Experimental Characterization of Dynamic Behavior of Micromachined Resonators

By

Junhui Zhao

A Thesis
Submitted to the Faculty of Graduate Studies
in Partial Fulfillment of the Requirement
For the Degree of

Master of Science

Department of Electrical and Computer Engineering
University of Manitoba,
Winnipeg, Manitoba
Canada

@ Junhui Zhao
2005

THE UNIVERSITY OF MANITOBA

FACULTY OF GRADUATE STUDIES

*****

COPYRIGHT PERMISSION

Experimental Characterization of Dynamic Behavior of Micromachined Resonators

BY

Junhui Zhao

A Thesis/Practicum submitted to the Faculty of Graduate Studies of The University of Manitoba in partial fulfillment of the requirement of the degree

Of

Master of Science

Junhui Zhao © 2005

Permission has been granted to the Library of the University of Manitoba to lend or sell copies of this thesis/practicum, to the National Library of Canada to microfilm this thesis and to lend or sell copies of the film, and to University Microfilms Inc. to publish an abstract of this thesis/practicum.

This reproduction or copy of this thesis has been made available by authority of the copyright owner solely for the purpose of private study and research, and may only be reproduced and copied as permitted by copyright laws or with express written authorization from the copyright owner.

0-494-09001-4

Library and Archives Canada

Published Heritage Branch

395 Wellington Street
Ottawa ON K1A 0N4
Canada

Bibliothèque et Archives Canada

Direction du Patrimoine de l'édition

395, rue Wellington
Ottawa ON K1A 0N4
Canada

Your file *Votre référence*
ISBN:
Our file *Notre retérence*
ISBN:

NOTICE:
The author has granted a non-exclusive license allowing Library and Archives Canada to reproduce, publish, archive, preserve, conserve, communicate to the public by telecommunication or on the Internet, loan, distribute and sell theses worldwide, for commercial or non-commercial purposes, in microform, paper, electronic and/or any other formats.

The author retains copyright ownership and moral rights in this thesis. Neither the thesis nor substantial extracts from it may be printed or otherwise reproduced without the author's permission.

AVIS:
L'auteur a accordé une licence non exclusive permettant à la Bibliothèque et Archives Canada de reproduire, publier, archiver, sauvegarder, conserver, transmettre au public par télécommunication ou par l'Internet, prêter, distribuer et vendre des thèses partout dans le monde, à des fins commerciales ou autres, sur support microforme, papier, électronique et/ou autres formats.

L'auteur conserve la propriété du droit d'auteur et des droits moraux qui protège cette thèse. Ni la thèse ni des extraits substantiels de celle-ci ne doivent être imprimés ou autrement reproduits sans son autorisation.

In compliance with the Canadian Privacy Act some supporting forms may have been removed from this thesis.

While these forms may be included in the document page count, their removal does not represent any loss of content from the thesis.

Conformément à la loi canadienne sur la protection de la vie privée, quelques formulaires secondaires ont été enlevés de cette thèse.

Bien que ces formulaires aient inclus dans la pagination, il n'y aura aucun contenu manquant.

Canada

Abstract

The micromachined mechanical resonators using MEMS technology have potential industrial applications in the fields of sensors and actuators as well as in the field of wireless telecommunications where the single chip transiver system might be possible by using the micromachined mechanical resonators to replace all bulky, expensive and off-chip filters and oscillators. The rapid growth of these micromachined mechanical vibrating devices has increased needs for developing highly effective testing systems which are capable of testing the performance of the vibrating elements.

The testing of the micromechanical vibrating devices is usually performed using capacitive, piezoelectric and piezoresistive detection with network analyzer, spectrum analyzer and lock-in techniques. They, however, often encounter the interference from other parasitic signals including electrostatic feedthrough currents.

In this thesis optical techniques for detecting tiny movement of object were employed and compared with traditional electrical techniques. The optical methods utilized were laser beam deflection and optical interferometry,

The simple micromachined mechanical beam resonators with the expected resonant frequency of near 150 kHz and 11 MHz were tested. For the 150 kHz resonator, the experimental data acquired using capacitive coupling detection indicate the existence of significant parasitic signals characterized by low resonant peak amplitude and small phase shift ($\sim 25^0$) at resonant frequency. In contrast, optical measurements, using laser beam deflection technique, do not show significant effect of parasitic signals evidenced by its large peak amplitude and 180^0 phase change at the resonant frequency, clearly demonstrating advantages of optical methods. Non-linear behavior of the vibration of the micromechanical resonator was observed and identified as a "spring softening" effect mainly induced by the large electrostatic force. Criterion of nonlinear behavior and its hysteresis were also investigated and discussed.

For 11 MHz resonator, electrical measurement was first done with network analyzer by capacitive coupled method. Experimental data show three very week resonant peaks accompanied by very small phase shifts of about a few degrees. The very small amplitude

and phase change at the resonant frequency are attributed to the contribution from other parasitic signals. In contrast, the experimental data measured using optical fibre interferometer give a large amplitude peak at the frequency of 11.8 MHz accompanied by a large phase shift of about 120 degree, clearly indicating much less susceptibility to parasitic signals using optical measurement method. The "spring softening" nonlinear behavior was also observed when high DC bias voltages were applied, very similar to the behaviors displayed by the 150 kHz resonator.

Based on the experimental data for above two electromechanical systems, their mechanical properties, such as spring constant k_1 and resonant frequency f_r, and equivalent electrical parameters, such as resistance R_m, capacitance C_m and inductance L_m, were approximately derived in terms of equivalent electrical circuit theory. These parameters can be used no only to evaluate the mechanical properties of device structure and provide feedback to design and fabrication processes but also to perform simulation on electrical circuit and serve the construction of practical circuits, such as filters and oscillators.

Acknowledgements

First of all, I would like to express my deep thanks to Dr. Doug Thomson for giving me the opportunity to step into electrical engineering field, and I am very much grateful for his guidance, encouragement and support during my study.

I would like to thank all the professors in our SPM research group for sharing their knowledge through teaching and all other ways. Especially I sincerely thank Dr. G. E. Bridges for his academic and technical help during the experiment.

Thanks also go to many graduate students in our SPM Lab for their generous helps and useful discussions during the course of research and study, and to our department's technical staffs, especially Mr. Allan McKay, for their great assistances in many ways in instrumental design and construction.

I also would like to thank the Gennum Corp for providing samples, and especially lots of helpful suggestions and communications from Dr. Mircea Capanu are very much appreciated.

At last but not least, I would like to thanks my wife for her great patience with my study and considerate caring for our family life.

Contents

List of Figures

List of Tables

Chapter 1 Introduction

Microelectromechanical Systems (MEMS) technology, developed initially from the silicon integrated circuit (IC) industry, has been extensively explored and developed for fabricating various micromachined mechanical transducers [1-2]. These MEMS devices are actually the interface between the physical world and the electronic world, and they convert energy from one form to another form based on a wide variety of transduction mechanisms. Their potential industrial applications are involved in the fields of sensors and actuators as well as others including wireless communications, fluid transport, optical communication, etc. The engineering efforts of MEMS technology are to minimize size and power consummation of devices, to reduce cost and to improve performance through the batch-fabrication techniques as IC technology. Thus far, the complete integration of MEMS devices with the current IC is a great challenge to the commercial products.

1.1 Micromachined Mechanical Resonators

Micromachined mechanical devices with released movable mechanical structures occupy an important position in the MEMS family [1]. One of them is the micromechanical resonator. The operation mechanism of resonator is that the movable structure is excited and detected at its mechanical resonant frequency; change in resonant frequency due to either external force on the resonator or mass absorption can be detected. Thus, the real physical information related to the origins of change in resonant frequency can be disclosed.

The resonant vibration of the micromachined mechanical resonator can be practically applied to many fields. For instance, in the field of inertial sensors: accelerometers and gyroscopes are two main examples [3,4]. Accelerometers measure the acceleration of moving objects and gyroscopes measure the angular motion of rotating objects. Commercial MEMS accelerometers and gyroscopes, based on conventional capacitive - coupling mechanism, are now available from Analog Devices Inc., MEMSIC, Motorola, British Aerospace Ltd. and Silicon Sensing Systems [5].

Besides the inertial devices, the feasibility of the micromechanical resonators applicable to wireless communications has intensively been investigated in order to replace bulky and expensive quartz crystal oscillators, surface acoustic wave (SAW) oscillators, filters and mixers [6-11]. Their working principle is based on the property of resonance at its mechanical resonant frequency. For example, in a filter an input signal is used to excite the vibration of the resonator and output signal is resulted from the amplitude response of the resonator; signals with frequencies shifted away from the resonant frequency are filtered out. If such a resonator is connected with a feedback amplifier, an oscillator can be built under certain conditions, and its output signal has the resonant frequency of the resonator, which can be used as a carrier frequency in wireless communications. So far, MEMS resonators have not been practically available for wireless communications. One of the main reasons for this is that the integration with the integrated circuitry (IC) is difficult. To integrate sensors, the electronics are often built on one chip and the actual sensor on another chip; two chips are then wire-bonded together. This method is not feasible for wireless communications, because the advantage of size

reduction compared to quartz crystal resonators would be lost. The frequency regime of MEMS resonators may also limit their possible applications in wireless communications.

In addition, resonant sensing has been applied in numerous devices for the measurement of pressure, humidity, temperature, mass flow, specific gas, biological detection, force and magnetic field [12-19]. The mechanical structures of the resonant sensors can take a number of configurations such as a cantilever, a double-ended tuning fork or a clamped beam, etc. An atomic force microscope (AFM) is an example of the cantilever sensors, where resonant frequency changes with the force between the atoms of sample and a probe tip, the force of nano-Newton can be sensed [12]. Another application of such characteristic of resonant frequency is pressure sensor, where the force acted on the resonator is induced by the interaction of resonant element with surrounding gas. The pressure can be determined by detecting change in the resonant frequency caused by the force. Gas sensors are made based on the same mechanism, the resonant frequency changes due to the mass absorption by coating the resonator with an active layer that attracts certain gas molecules. Since different coatings select different molecules, gas sensors can be made for very specific gases [16]. Biological sensors work in a similar way, where the resonator is coated with an immobilized antibody and has a sensitivity of a few cells [17, 18].

1.2 Detection of Resonant Frequency

The design, performance and reliability of the MEMS devices largely depend on how much is known about their mechanical properties of materials and dynamical behaviors of microstructures. Thus, with the rapid development of movable micromechanical

systems, characterization of the static and dynamic behavior of these micro-devices is becoming increasingly important by establishing appropriate testing techniques for precise measurements on the microstructures so as to verify and to provide feedback to design and fabrication process.

1.2.1 Electrical Detection Methods

The resonant vibration of the micromechanical devices can usually be excited and detected electrically through capacitive-coupling. Piezoelectric and piezoresistive sensing [1] are also commonly used to convert the mechanical motion into the electrical signal. These conventional measurements can provide the information of their mechanical properties through their electrical performance. However, they often encounter the problem of the interference from other parasitic signals.

In contrast, optical detection methods for very small mechanical vibrations have been proved to be highly effective ways due to their sub-nanometer resolution and insusceptibility to the electrical parasitic signals.

1.2.2 Optical Detection Methods

Optical testing can perform MEMS surface profiling and measurement of in-plane and out-of-plane motion [20-22]. Surface profiling mainly includes focus detection profilometers and microscopic interferometry. Scanning point profilometer uses a point measurement probe with a translation of the light beam or sample; Full-field profilometer uses a detector array to obtain simultaneous measurements of a large number of points. Scanning point profilometers are based on the detection of the focusing variations of a

laser or white light beam when the sample is scanned in its XY plane. Focus detection profilometers have typically a vertical resolution in the 1-10 nm range, a spot size down to 1 μm, a vertical dynamic range of 10 to 100 μm or more and frequency bandwidth of a few kHz or a few tens of kHz. Scanning point profilometers are suited for 1-D and 2-D measurements; Full field profilometers are better suited for 3-D surface profiling.

Microscopic interferometry is a most widely used optical technique for microdevice profiling. Holographic inteferometry and speckle techniques are common full field techniques in mechanical engineering for surface contouring and displacement field measurements. Both are based on the interferences between a laser beam scattered by the sample surface and a reference laser beam.

Measurement of out-of-plane motion is usually carried out using the following methods:

Laser beam deflection detection

Laser beam deflection technique measures the vibration of movable devices by detecting the angular variations of the laser beam reflected from the vibrating element using a spectrum analyzer or lock-in amplifier. It has a sub-nanometer resolution for out-of-plane vibration; but, accurate calibration of vibration amplitude is difficult. In-plane spatial resolution below a few micrometers is limited by its focusing ability and spot size.

Optical interferometer techniques

There are two kinds of interfering techniques: heterodyne and homodyne. Heterodyne interferometer measures the phase changes resulted from both phase difference induced by the motion of device and the frequency shift introduced between the probe path and the reference path where RF-driven Bragg cells modulate the frequency of the reference light. The phase changes are detected through measuring the interfering intensity

produced from the probe light and the frequency modulated reference light. Heterodyne interferometer, often named velocimeter, measures velocity rather than displacement. It has a 0.01 nm motion resolution in a frequency bandwidth of a few MHz and submicron spatial resolution. Homodyne interferometer directly detects the interference intensity related to the phase change between the probe light and the reference light, which is introduced by the displacement of moving object, both lights have the same frequency. Both amplitude and phase information can be extracted using Lock-in technique. Typical resolution values lie between 0.01-0.1 nm [22].

1.3 Objective of Thesis Work

This thesis work mainly focuses on some important issues in the detection of the resonant vibration of the micromechanical resonators, and in the characterization of the dynamic vibration behaviors using both electrical measurements and optical measurements. Their advantages and disadvantages will be demonstrated experimentally. It is expected that experimental measurements will demonstrate how well the performance of practical devices agrees with the theoretical mechanics and its design expectation. Many important mechanical parameters are expected to be derived from the experimental measurements, such as resonant frequency, spring constant and quality factor; electromechanical properties, such as equivalent electrical components of the mechanical system, will also be explored so as to further study of this electromechanical system. It is hoped that these experimental data for the micromechanical resonators are helpful to further understand how the micromachined mechanical resonator filters and oscillators work and how they can be constructed.

1.4 Outline of the Thesis

The task of this thesis is to explore the experimental techniques for measuring dynamic behaviors of micromachined mechanical resonators using both electrical methods and optical methods. Prior to the description of measurement techniques and experiment setup, the understanding of the dynamic motion behavior of micromachined mechanical resonators is necessary. Mechanical properties of the mechanical resonators will be presented in chapter 2, some important dynamic mechanical properties and their related theoretical analysis will be reviewed. Nonlinearity of vibration in the mechanical system, due to its interesting and important property directly related to the performance of the mechanical devices, will also be introduced. In addition, vibrating mechanical system is electrically analogous to an electrical circuit; hence, equivalent electrical circuit will be briefly discussed so as to allow the current powerful circuit theories and simulation tools be applied to the micro-electromechanical system. After that, mechanisms of a few typical electrical and optical detection techniques will be discussed in detail in chapter 3. Chapter 4 will first give a comprehensive conception of the MEMS technology concerning its special fabrication processes; then, our experimental setup for electrical and optical measurements will be illustrated. In chapter 5 the experimental results and data analysis will be presented and discussed based on the theoretical conception described in chapter 2. Finally, summarization of this thesis work and suggestions for future work will be proposed in chapter 6.

Chapter 2 Properties of the Mechanical Resonators

The micromachined mechanical resonators have many geometrical topologies: such as, the free-fixed cantilever, the clamped-clamed resonate beam, comb type driver, etc. Their design, fabrication and modeling require a thorough theoretical analysis on their mechanical behaviors on which experimental setup and data analysis rely. General mechanical properties of mechanical resonant beam structures will be reviewed in this chapter. Resonance problem of a clamped-clamped (C-C) beam and free-fixed cantilever will be discussed in terms of a simplified beam theory. The dynamical properties of the beam resonator will be modeled and analyzed using a simplified lumped harmonic oscillator in a single degree of freedom. Nonlinear behavior of the beam resonator will also be discussed. By analyzing the electromechancial coupling between electrical signal and mechanical vibration, equivalent electrical circuit for the mechanical system will be established to describe its electrical behavior based on circuit theory.

2.1 Transverse Vibration of Prismatic Beams

A flexural beam structure in the form of cantilever, as a simple and special example shown in figure 2.1, is assumed to be composed of homogeneous, linearly elastic materials in a shape of a rectangular cross-section. A linear dynamic equation governing the transverse deflections $u(x,t)$ of such prismatic beam as a function of the longitudinal coordinate x and the time t can be expressed as follows [23-25].

$$EI\frac{\partial^4 u(x,t)}{\partial x^4} - N\frac{\partial^2 u(x,t)}{\partial x^2} + \rho bh\frac{\partial^2 u(x,t)}{\partial t^2} + c\frac{\partial u(x,t)}{\partial t} = F(x,t) \qquad (2.1)$$

where ρ denotes the mass density of the beam material, b and h are the width and thickness of the beam, respectively, c is the viscous damping coefficient per unit length, $F(x,t)$ represents all externally applied transverse mechanical forces per unit length. E is the Young's modulus of the beam material, I is the second moment of inertia of the beam, N is an applied axial force (for the cantilevers, $N = 0$). Equation (2.1) applies to the beams for which the width b is comparable to the thickness h, i.e., $b \sim h$. For so-called wide beams (plates), i.e., $b > 5h$, Young's modulus is effectively replaced by $E=E_0(1 - \nu)^2$, where ν denotes Poisson's ratio.

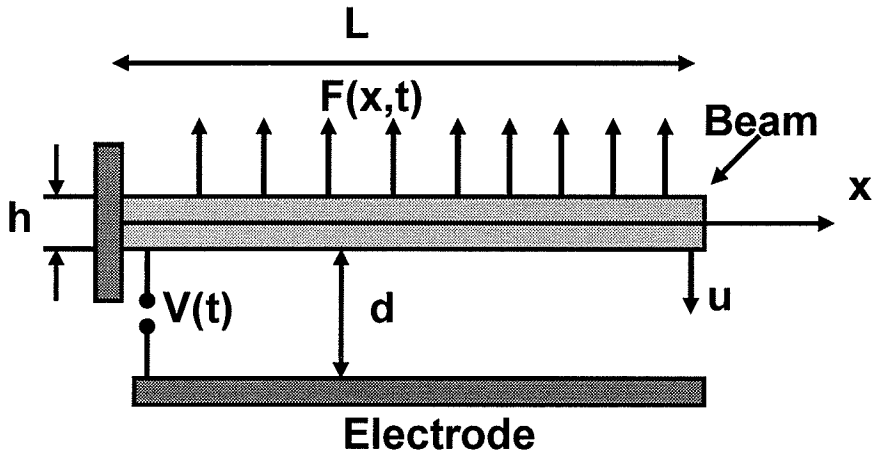

Figure 2.1 Schematic diagram of cantilever-type beam structure

To solve the differential equation (2.1), the method of 'variables separation' can be applied to derive characteristic equations. Solution to equation (2.1) based on the concept of modal analysis can be written as follows:

$$u(x,t) = \sum_{n=1}^{\infty} u_n(x) u_n(t) \tag{2.2}$$

where $u_n(x)$ is a spatial function representing different mode shapes of vibration and $u_n(t)$ is a time-dependant function representing the displacement of the motional beam. When the equation (2.2) is substituted into the equation (2.1), by multiplying each term in the equation (2.1) with a normal mode $u_n(x)$ and integrating along the beam length, then, by utilizing the orthogonal property of the mode shapes, the following formulas are deduced [24]:

$$EI\frac{\partial^4 u_n(x)}{\partial x^4} - N\frac{\partial^2 u_n(x)}{\partial x^2} = \omega_n^2 \rho b h u_n(x) \tag{2.3}$$

$$M_n\frac{\partial^2 u(t)}{\partial t^2} + r_n\frac{\partial u(t)}{\partial t} + K_n u(t) = F_n(t) = F_n e^{jwt} \tag{2.4}$$

Where n = 1, 2,3 …, n is the mode number.

$$M_n = \int_0^1 \rho b h u_n^2(x)dx = \rho b h l = m \tag{2.5}$$

which is the generalized mass corresponding to mode n;

$$K_n = \int_0^1 u_n(x)[EI\frac{\partial^4 u_n(x)}{\partial x^4} - N\frac{\partial^2 u_n(x)}{\partial x^2}]dx = \omega_n{}^2 M_n \tag{2.6}$$

which is the generalized spring stiffness corresponding to mode n.

$$r_n = \int_0^1 c u_n^2(x)dx = cl \tag{2.7}$$

which is the generalized viscous damping corresponding to mode n.

$$F_n = \int_0^1 F(x)u_n(x)dx \tag{2.8}$$

which is the generalized external force corresponding to mode n.

where ω_n denotes the non-damped resonant frequency associated with mode *n*. *m* is the total mass of the beam. The above relations assume mode shapes are normalized. It is noticed that r_n and M_n are independent of the mode number n for the beam structures. Equation (2.4) represents an infinite set of uncoupled ordinary differential equations with the same form describing the motion of a lumped parameter system. As a matter of fact, the partial differential equation of motion for a distributed system is replaced by an infinite set of uncoupled ordinary differential equations in the modal analysis. Each of the distributed systems is now represented by an infinite number of lumped-parameter systems.

Equation (2.3) is called Euler beam equation, which can be solved as an eigenvalue problem, eigenvalue ω_n^2 and its corresponding eigenfunction $u_n(x)$ can be determined under appropriate boundary conditions. Each of eigenvalue-eigenfunctiong pair defines a mode of the system. ω_n are called the natural frequencies while $u_n(x)$ are named as the mode shapes of the system.

When electromechanical interactions and axial load (N) are absent, the eigenfunctions for a clamped–clamped beam of length l are found to be [24]

$$u_{ncc}(x) = \cos(k_n x) - \cosh(k_n x) + \frac{\cos(k_n l) - \cosh(k_n l)}{\sinh(k_n l) - \sin(k_n l)}(\sin(k_n x) - \sinh(k_n x)) \qquad (2.9)$$

for a cantilever (fixed–free) beam, it becomes:

$$u_{ncf}(x) = \cos(k_n x) - \cosh(k_n x) - \frac{\cos(k_n l) + \cosh(k_n l)}{\sinh(k_n l) + \sin(k_n l)}(\sin(k_n x) - \sinh(k_n x)) \qquad (2.10)$$

where k_n are constants corresponding to mode n. It is easily verified that the above mode shapes are normalized, i.e., $\frac{1}{l}\int_0^l u_n(x)u_m(x)dx = \delta_{nm}$, where δ_{mn} denotes the Kronecher

delta. These constants k_n can be determined from the characteristic equation by solving the special eigenvalue problem under the appropriate boundary conditions. The corresponding natural frequencies ω_n can be found for zero axial load N as follows

$$\omega_n^2 = k_n^4 (EI / \rho bh) \tag{2.11}$$

Where $I = bh^3/12$.

For a clamped–clamped beam the characteristic equation can be derived as $\cos(kl)\cosh(kl)=1$, yielding the following fundamental mode k_1, $k_1 l \sim 4.730$, and for a cantilever, $\cos(kl)\ \cosh(kl)=-1$, yielding, $k_1 l \sim 1.875$. Table 2.1 lists the values of $k_n l$ corresponding to the first five mode shapes [23].

Table 2.1 Values of the first five mode shapes

n	$(k_n l)^2$	
	Cantilever beam	Clamped-clamped beam
1	3.516	22.373
2	22.034	61.678
3	61.701	120.903
4	120.912	199.860
5	199.855	298.526

2.2 Spring Constant k

In above section the vibration modes and their corresponding natural frequencies were derived. Now, a general expression for the effective stiffness of the beam system will be defined based on the mode shapes. The effective stiffness K_{eff} is defined as F/u_{max} where

F is a uniformly distributed load over a section of the beam of the length L, and u_{max} is the maximum deflection of a continuous beam structure. For a C-C beam u_{max} is at the center of the beam and for a fixed-free beam u_{max} is at the tip of free end for the first mode shape. The clamped-clamped beam with immovable edges subjected to symmetrically distributed transverse load and axial force N is schematically shown in figure 2.2.

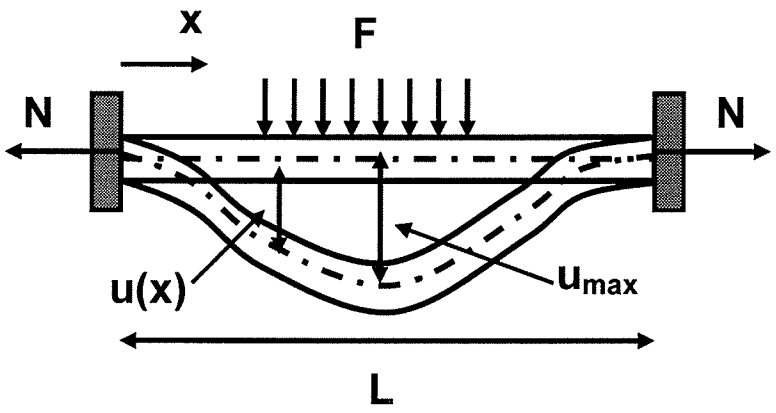

Figure 2.2 A C-C beam subjected to symmetrically distributed uniform load

Normally the stiffness is attributed to the bending and the stretching of the beam. The contribution to the beam stiffness not only includes built-in stress σ_0 but also the induced nonlinear stress σ_{NL} that arises from a large deflection. A generalized expression for the stiffness must take all these effects into account.

For the C-C beam with a uniform load F, the boundary conditions require $u(0) = u(L) = 0$ and du/dx = 0 at both sides of x = 0 and x=L. When tensile stress N is zero, the solution is derived as follows [26]:

$$u = \frac{x^2(L^2 - 2Lx + x^2)}{2Ebh^3} F \tag{2.12}$$

Using the definition of Hook law, $k_{eff}^{cc} = \frac{FL}{u_{\max}}$

where u_{max} is at the position of x = L/2, thus

$$k_{eff}^{cc} = \frac{32\hat{E}bh^3}{l^3} \tag{2.13}$$

When an axial loading is applied, a tensile force takes a form of N = $(\sigma_0 + \sigma_{NL})$bh, where $\hat{\sigma}_0 = \sigma_0$ (1-ν) is the residual film stress; $\sigma_{NL} = \frac{\pi^2 E u_{\max}^2}{4l^2}$ is an estimate of the induced axial stress due to the nonlinear stretching. The effective stiffness k_{eff}^{cc} of a fixed-fixed beam can be derived as follows [27]

$$k_{eff}^{cc} = \frac{32\hat{E}bh^3}{l^3} + \frac{8N}{l} \tag{2.14}$$

where $\hat{E}$ = E/(1-ν^2) for b > 5h, $\hat{E}$ = E for b = h. The second term comes from the axial loading resulted from axial stretching.

2.3 Nonlinear Mechanical Deflection

It is mentioned above that when the C-C beam is subjected to the large deflection the elongation of the beam need to be considered. Besides the bending of the beam, the stretching of the beam also contributes the strain in the structure in a nonlinear form.

'Variation approach', by minimizing energy with respect to displacement u, yields the following expression relating an applied force F to the deflection amplitude u [26]

$$F = \frac{\pi^4}{6}\frac{Ebh^3}{L^3}u + \frac{\pi^4}{8}\frac{Ebh}{L^3}u^3 \tag{2.15}$$

The second non-linear term makes the effective spring constant of the non-linear beam stiffer as the deflection amplitude u increases, this is called Duffing stiffening which is often encountered in MEMS structures. The solution includes two parts: the first term is due to the bending of the beam, as being linear; and the second term is due to the stretching of the beam, introducing the non-linearity.

When the nonlinear stiffening effect becomes dominant due to the stretching induced by the large deflection of the beams, the nonlinear stiffness term will be larger than the total stiffness induced by the bending of the beam and the residual stress of the beam material. The nonlinear stiffening becomes important if the following condition is reached [27]:

$$\frac{2\pi^2 Ebhu_{\max}^2}{l^3} >> \frac{32\hat{E}bh^3}{l^3} + \frac{8\hat{\sigma}_0 bh}{l} \tag{2.16}$$

The formula 2.16 can be used as a criterion to evaluate the nonlinear behavior.

Above analysis is mainly concerned with the static mechanics of a continuously distributed mass described in equation (2.3). Next, the dynamic mechanical behavior will be dealt with a lumped harmonic model.

2.4 Lumped Harmonic Oscillation

As it can be seen from the equation (2.1), it is difficult to solve the dynamic mechanics of a continuously distributed system. Even for such a simple beam structure, the derivation of the natural resonant frequencies and the mode shapes requires a simplified model for the mathematical description of the problem. An equivalent lumped model for the distributed system has been developed and proved as a reasonably good method for analyzing the dynamic problems. The simplest of them is one-degree of freedom system

consisting of a massless spring with spring constant k and a mass m attached to the spring. The model will be discussed and it will show that the model of a harmonic oscillator can reasonably well describe the vibration of complex structures like cantilever and C-C beams. The equation (2.4) can be rewriten as follows

$$m\frac{\partial^2 u(t)}{\partial t^2} + c\frac{\partial u(t)}{\partial t} + ku(t) = F(t) = Fe^{jwt} \tag{2.17}$$

where m, c, k and F can be considered as effective parameters as described in the section (2.3) , By neglecting damping and external forces, the equation of motion is simplified as a simple harmonic oscillation

$$m\frac{d^2 u}{dt^2} + ku = 0 \tag{2.18}$$

The solution of this equation is assumed as

$$u(t) = A_1 \sin(\omega_0 t) + A_2 \cos(\omega_0 t) \tag{2.19}$$

where ω_0 is a resonant frequency in a form

$$\omega_0 = \sqrt{\frac{k}{m}} \tag{2.20}$$

Now the beam resonator is approximated as a simple harmonic oscillator with an effective spring constant k and an effective mass m.

If a damping force –c(du/dt), in addition to a spring restoring force –ku, is included, and the externally applied force F(t) on the vibrating mass varies harmonically, by introducing the following notations:

$$\omega_0{}^2 = \frac{k}{m} \quad ; \quad 2r = \frac{c}{m}; \quad F_0 = \frac{F}{m}$$

Equation (2.17) becomes

$$\frac{\partial^2 u(t)}{\partial t^2} + 2r\frac{\partial u(t)}{\partial t} + \omega_0^2 u(t) = F_0 e^{jwt} \tag{2.21}$$

This is the differential equation of motion for a forced oscillator subjected to the viscous damping. A particular solution of equation (2.21) can be taken as the following form:

$$x = M\cos\omega t + N\sin\omega t \tag{2.22}$$

where M and N are constants. To determine these constants, by substitute the trial solution (2.22) into equation (2.21), M and N are found as follows [23]:

$$M = \frac{F_0(\omega_0{}^2 - \omega^2)}{(\omega_0{}^2 - \omega^2)^2 + 4r^2\omega^2} \tag{2.23a}$$

$$N = \frac{F_0(2r\omega)}{(\omega_0{}^2 - \omega^2)^2 + 4r^2\omega^2} \tag{2.23b}$$

The solution of this equation can also be rewritten using vibration amplitude A and phase θ angle defined in the following formulas:

$$u = A\cos(\omega t - \theta) \tag{2.24}$$

where $A = \sqrt{M^2 + N^2}$ and $\theta = \tan^{-1}(\frac{N}{M})$. Thus, they can be derived as

$$A = \frac{F_0 / \omega_0{}^2}{\sqrt{(1-\omega^2/\omega_0{}^2) + 4r^2\omega^2/\omega_0{}^4}} \tag{2.25a}$$

$$\theta = \tan^{-1}\left(\frac{2r\omega/\omega_0{}^2}{1-\omega^2/\omega_0{}^2}\right) \tag{2.25b}$$

Let $\zeta = r/\omega_0$, the formula (2.24) can be rewritten as the following equation

$$u = \frac{F}{k}\beta\cos(\omega t - \theta) \tag{2.26}$$

$$\beta = \frac{1}{\sqrt{(1-\omega^2/\omega_0{}^2) + 4\varsigma^2\omega^2/\omega_0{}^2}} \tag{2.27a}$$

$$\theta = \tan^{-1}\left(\frac{2\varsigma\omega/\omega_0}{1-\omega^2/\omega_0{}^2}\right) \tag{2.27b}$$

Where β is called magnification factor, which represents how much amplitude of vibration is magnified when the frequency ω of external force approaches to the resonant frequency ω_0 of the oscillator.

Figure 2.3 (a) and (b) shows the frequency dependence of the amplitude and the phase of the damping harmonic oscillation plotted using equation (2.27) (a) and (b). Thus, a steady-state forced vibration with viscous damping now is seen as a simple harmonic motion with constant amplitude A, phase angle θ and period $T = 2\pi/\omega_0$. It can be seen that the amplitude of the vibration is magnified greatly when external forcing frequency ω approaches to the resonant frequency ω_0, the magnification can be expressed by quality factor Q which is derived as follows:

$$Q = \frac{\omega_0^2}{\sqrt{(\omega_0^2-\omega^2)+(2\varsigma\omega)^2}} \cong \frac{1}{2\varsigma} = \beta \tag{2.29}$$

In addition, the amplitude of resonance and the quality factor Q will decrease as the viscous damping increases, and the resonant frequency is shifted down due to the viscous damping, which can be expressed in the following form [23]

$$\omega_r = \omega_0\sqrt{1-\frac{2r^2}{\omega_0^2}} \tag{2.28}$$

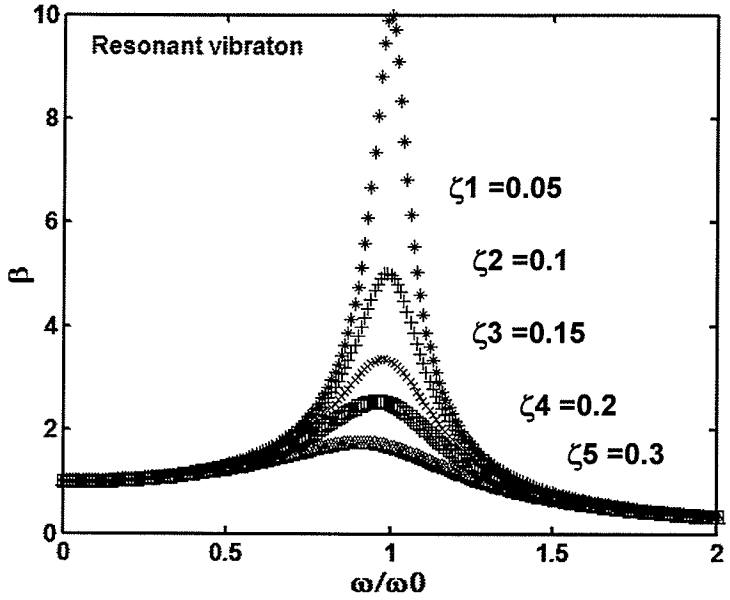

(a)

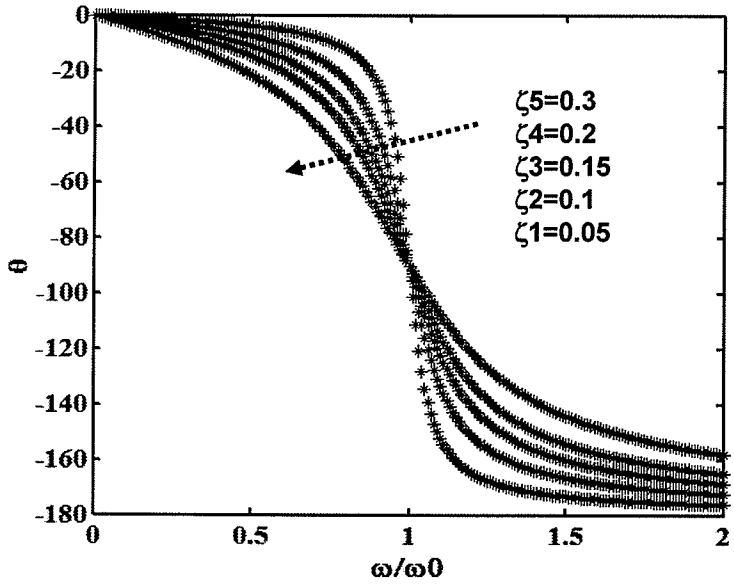

(b)

Figure 2.3 Frequency response of the simple harmonic vibration. (a) is dependence of vibration amplitude upon frequency; (b) is the phase change with frequency.

2.5 Nonlinear Vibration

In above section the linear differential equation is used to describe the vibration behavior when the deflection linearly responses to the external force for its small displacement. Once the deflection becomes large enough to make the system show nonlinear behavior, the equation (2.17) becomes the following form:

$$\ddot{u} + 2r\dot{u} + \omega_0{}^2(u \pm \mu u^3) = F\cos\omega t \tag{2.30}$$

The new term of u^3 represents the nonlinear contribution. The equation is called Duffing's equation which describes the steady-state response of a non-linear system subjected to a periodic forcing function and viscous damping. The Ritz averaging method can be used to deduce an approximate solution as follows [23].

As a first approximation, solution can be written in a form:

$$u = A\cos(\omega t - \varphi) = a_1\cos\omega t + b_1\sin\omega t \tag{2.31}$$

where $A^2 = a_1{}^2 + b_1{}^2$, and $tan\varphi = b_1/a_1$. Two constants a_1 and b_1 can be determined by the Ritz averaging method, and the following formulae can be derived

$$\frac{3\mu A^3}{4} = \left(\frac{\omega^2}{\omega_0{}^2} - 1\right)A + \frac{F_0}{\omega_0{}^2}\sqrt{1 - \frac{(2r\omega cA)^2}{F_0{}^2}} \tag{2.32a}$$

$$\frac{3\mu A^3}{4} = \left(\frac{\omega^2}{\omega_0{}^2} - 1\right)A - \frac{q}{\omega_0{}^2}\sqrt{1 - \frac{(2r\omega A)^2}{\omega_0{}^2}} \tag{2.32b}$$

where equation (2.32a) applies to the case of the 'hardening spring' and equation (2.32b) to the 'softening spring'.

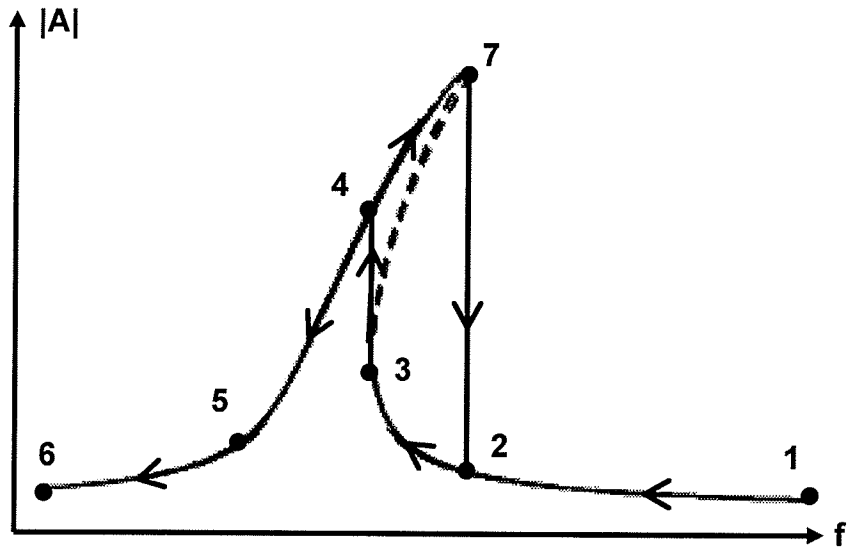

(a)

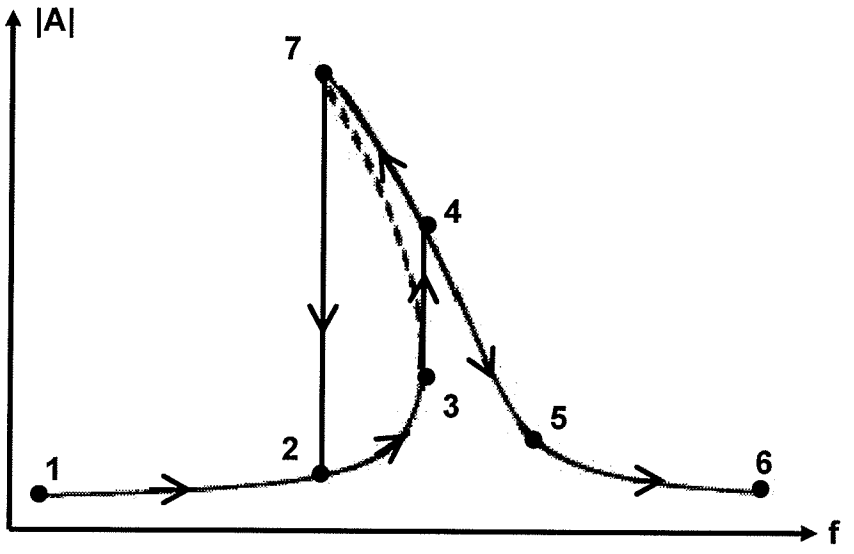

(b)

Figure 2.4 Schematic of the nonlinear behavior. (a) shows the 'spring hardening' and (b) shows the 'spring softening' [23].

The behavior of the vibration amplitude versus sweep frequency is schematically illustrated in the figure 2.4 where (a) describes the 'spring hardening' and (b) describes the 'spring softening'. In the figure 2.4 (a) and (b), nonlinear resonant frequency ω_r, at the highest point of amplitude, shifted up and down, respectively. But, the nonlinear resonant states, labeled as point 7 in both figures, may not actually occur because of the non-stable condition. In fact, the rapid jump in amplitude from point 3 to point 4 in the figure 2.4 (a) may occur when frequency sweeps down; the rapid drop from point 7 to 2 may occur when frequency sweeps up. The rapid jump in amplitude from point 3 to point 4 in the figure 2.4 (b) may occur when frequency sweeps up; the rapid drop from point 7 to 2 may occur when frequency sweeps down. Hysteretic behavior will occur when frequency was swept up and down.

In the damped systems, the phase angle φ varies continuously from 0 to π as the driving frequency ω varies from 0 to ∞. At resonance the phase angle is theoretically $\pi/2$, but actually it changes abruptly when a drop or a jump occurs. Such a change is from a value slightly below zero to a value slightly above π.

2.6 Electromechanical Coupling

Micromechanical system is typically interacted with electronics through capacitive coupling; electrostatic coupling has minimal power consumption. Electrostatic energy stored in a capacitor C is

$$E = \frac{1}{2} C U^2 \tag{2.33}$$

and

$$C = \varepsilon \frac{A}{d-u} = \frac{C_0}{1-u/d} \tag{2.34}$$

where U is the voltage applied on the capacitor. The capacitance value depends on the gap size d and on the displacement u of the moving resonator. Capacitance with zero displacement u is C_0, A is the effective area overlapped by the electrode and the resonator. The electrostatic force equals the negative gradient of energy. Using Taylor's series, it can be written as follows:

$$F_e = -\frac{U^2}{2}\frac{\partial C}{\partial u} \tag{2.35}$$

$$F_e = -\frac{U^2 C_0}{2d}\left[1 \mp 2\left(\frac{u}{d}\right) + 3\left(\frac{u}{d}\right)^2 \mp 4\left(\frac{u}{d}\right)^3 + \cdots + (n+1)\left(\frac{u}{d}\right)^n\right] \quad (\text{u/d} < 1) \tag{2.36}$$

The electrostatic force is proportional to the voltage squared. Thus, a DC voltage is required to create the force that excites the oscillator exactly at the frequency of AC driving voltage. If both DC and AC voltage are applied, we have

$$U^2 = U_{DC}^2 + \frac{1}{2}U_{AC}^2 + \frac{1}{2}U_{AC}^2 \cos 2\omega t + 2U_{DC}U_{AC}\cos \omega t \tag{2.37}$$

from above two equations it can be seen that the electrostatic force has components at frequencies of zero, ω and 2ω. Since the excitation at the frequency of AC driving voltage is required, the DC voltage must be much stronger than the AC voltage. In addition, the displacement u is typically small compared with the gap size d, which means that the force can be approximated as follows

$$F_e \approx -\frac{C_0}{2d}\left[1 + 2\left(\frac{u}{d}\right)\right]U^2 \approx -\frac{C_0 U_{DC}^2}{2d} - \frac{C_0 U_{DC}^2}{d^2}u - \frac{C_0 U_{DC} U_{AC}}{d}\cos(\omega t) \tag{2.38}$$

where the multiplying factor of u can be interpreted as an electrical spring constant k_e.

It can be seen that the magnitude of the electrostatic force at ω depends on the applied AC and DC voltage and the gradient of the capacitance.

2.7 Electromechanical Coupling Factor

The electromechanical coupling factor η can be derived from equation (2.38), the relation between the AC voltage and the force F_e is

$$F_e = U_{DC}\frac{\partial C}{\partial u}U_{AC} \tag{2.39}$$

The electromechanical coupling factor is defined as:

$$\eta = U_{DC}\frac{\partial C}{\partial u} \approx U_{DC}\frac{C_0}{d} \tag{2.40}$$

Thus, the coupling between the electrostatic and mechanical domains depends on the coupling capacitance C_0 and the gap size d between the electrode and the resonate beam as well as on the DC bias voltage over the gap. Narrow gap will strongly enhance the electromechanical coupling.

2.8 Sensing of Vibration

The oscillating MEMS resonator works by applying a DC bias voltage and an AC exciting signal on it. The motional current induced by the vibration can be derived as follows, when $U_{DC} >> U_{AC}$:

$$i_m = \frac{dQ}{dt} = \frac{d(UC)}{dt} \approx U_{DC}\frac{\partial C}{\partial t} \tag{2.41}$$

If the motion is assumed to be sinusoidal, the motion current can be rewritten as

$$i_m = U_{DC}\frac{\partial C}{\partial u}\frac{\partial u}{\partial t} = U_{DC}\frac{\partial C}{\partial u}\omega u = \eta\omega u \tag{2.42}$$

In addition to the DC bias voltage and the vibration amplitude, the motional current depends also on the frequency and the gradient of the capacitance between the electrode

and the resonator. Based on Hook's law, the vibration amplitude at resonance can be obtained by dividing the force (equation (2.39)) with the spring constant, Q is the amplification factor at the resonance.

$$u = Q\frac{\eta U_{AC}}{k} \approx Q\frac{C_0 U_{DC} U_{AC}}{kd} \tag{2.43}$$

Thus, the motional current depends strongly on the electromechanical coupling factor, DC-bias voltage and AC voltage, and the derivative of the coupling capacitance; also, High quality factor Q is also important for getting high motional current.

2.9 Effective Electrical Spring Constant k_e

The overall spring constant of the electro-mechanical system is the sum of mechanical spring constant k_1 and electrical spring constants k_e. The electrical spring constant k_e is defined as

$$k_e = -\frac{\eta U_{DC}}{d} \approx -\frac{C_0 U_{DC}^2}{d^2} \tag{2.44}$$

Since the total spring constant is reduced by the electrical spring constant, it thus has an effect on the resonance frequency of the resonator

$$\omega_r = \omega_0\sqrt{1-\frac{k_e}{k_1}} = \omega_0\sqrt{1-\frac{C_0 U_{DC}^2}{k_1 d^2}} \tag{2.45}$$

where $\omega_0^2 = k_1 / m$.

The resonant frequency becomes smaller due to the electrostatic force. Therefore, the electromechanical coupling can be used to tune the resonance frequency. However, the frequency tuning is limited by a pull-in effect.

2.10 Pull-in Voltage

Pull-in voltage is defined as the voltage at which the restoring spring force can no longer balance the attractive electrostatic force. Pull-in instability is fundamental to the understanding of many MEMS devices and it can be used to determine some unknown electromechanical properties.

It is assumed that two plates, separated by a gap spacing d, form a capacitor with an effective overlap area A_{eff}. The bottom plate is fixed and the top plate is suspended by a spring with stiffness K_{eff}. By applying a DC voltage V_{dc} across the plates, an electrostatic attractive force is induced, which leads to a decrease of the gap spacing, thereby stretching the spring. This results in an increase of the spring force which counteracts the electrostatic force. Pull-in instability occurs when the voltage is so high that the resonator beam sticks to the electrode. The pull-in behavior is observed when the mechanical and electrical forces (and simultaneously also their derivatives) cancel each other. The value of pull-in voltage for a static case can be calculated as follows [27]:

$$V_{PL} = \sqrt{\frac{8K_{eff}d_0^3}{27\varepsilon_0 A_{eff}}} \tag{2.46}$$

where d_0 is the separation between two plates in the absence of DC voltage.

2.11 Equivalent Electrical Circuit for Electromechanical System [24, 25]

Electromechanical coupling realizes the conversion between mechanical energy and electrical energy through exciting and detecting the mechanical vibration. There are many techniques to fulfill the electromechanical coupling, such as piezoresistive, piezoelectric, and capacitive methods. Other ways for actuating and sensing include magnetic, optical

and acoustic, etc. Of all techniques, As far as practical application is concerned, the electrostatic excitation and detection are preferred because it makes the co-fabrication of microbeam resonators and peripheral electronic circuits on a single chip possible. The microbeams and the electrode can be easily implemented for the purpose of excitation and detection.

Since the electrostatically driven beam resonator has the characteristics of nonlinearity in the electrostatic excitations, the devices require a DC bias voltage and a small sinusoidal AC signal to excite and detect a purely sinusoidal resonance. It should be noticed that the DC bias possibly results in a mechanical instability and a lowering of the quality factor. Existence of parasitic signals in the electrostatically driven and sensed microbeam can also be a problem for the electrical performance of the resonant system.

Since electrical network theory and circuit simulation software such as SPICE have been well developed, it is very helpful to analyze the performance of the electrostatically driven beam resonator using the equivalent electrical circuit of the microbeam resonator. The electrical equivalent circuit is also useful in interpreting the parasitic effects on the performance of the polysilicon beam resonator, especially the gain–phase response.

The mechanical behavior of microbeam resonator is described by the differential equation of motion with a set of boundary conditions. The electromechanical coupling associates the electrical performance with the mechanical properties. Thus, the electromechanical system behaves like an equivalent electrical circuit composed of inductors, resistors, and capacitors. These equivalent electrical components for the electromechanical system can be derived based on the analogy of the mathematical description for electrical and mechanical properties. In this way, the electrical

components in an electric circuit such as inductors, resistors, and capacitors can be represented by the properties of the mechanical system, such as mass, stiffness, and damping, with the help of the electromechanical coupling coefficient. The corresponding parameters for the mechanical and the electrical description are listed in the table 2.2.

Table 2.2 The correspondent mechanical and electrical parameters [28]

Mechanical parameters	Electrical parameters
Mass (m)	Inductance (L)
Compliance (spring) (1/k)	Capacitance (C)
Viscous damping (c)	Resistance (R)
Force (F)	Voltage (U)
Displacement (x)	Charge (q)
Velocity (dx/dt)	Current (i)
Momentum (p)	Magnetic flux (Φ)

As shown in figure 2.5 (a) the transverse electrostatic microbeam is taken to establish the equivalent electrical circuit of the micromechanical system [28]. The transversely vibrating beam is the upper plate of capacitor parallel to the lower electrode in the substrate. The current flowing into the capacitor between the upper and the lower plates is found to be

$$i(t) = \frac{\partial}{\partial t} q(t) = C(t) \frac{d[U_{dc} + U_{ac}]}{dt} + [U_{dc} + U_{ac}] \frac{dC(t)}{dt} \qquad (2.47)$$

Since the gap d is much larger than the beam deflection $u(t)$ and $U_{dc} >> U_{ac}$, the equation (2.47) is approximated as

$$i(t) = C_0 \frac{dU_{ac}}{dt} + \frac{U_{dc} C_0}{d} \frac{du(t)}{dt} = i_0(t) + \eta \frac{du}{dt} = i_0(t) + i_m(t) \tag{2.48}$$

where $\eta = U_{DC} \frac{\partial C}{\partial u} \approx U_{DC} \frac{C_0}{d}$ is the coupling factor of the electromechanical system. $i_0(t)$ is the feedthrough current and $i_m(t)$ is the electromechanically induced motional current.

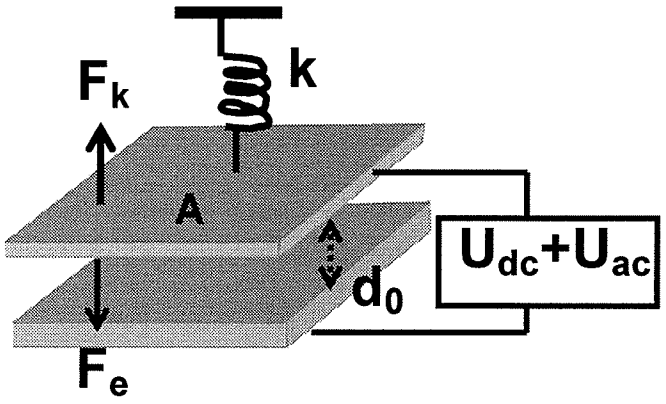

(a)

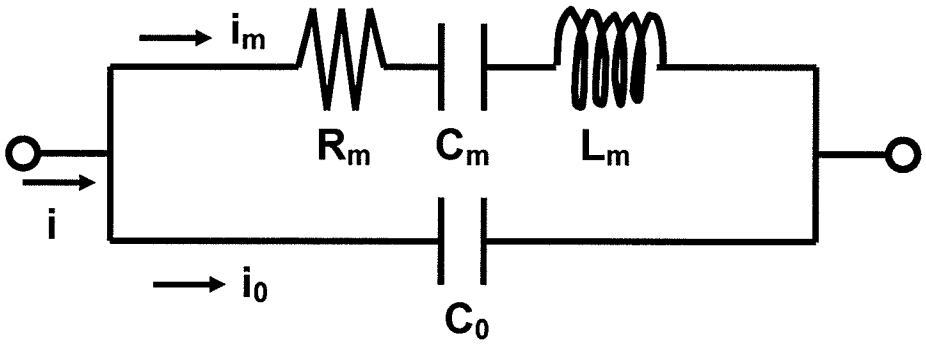

(b)

Figure 2.5 The schematic diagram of the capacitive beam resonator (a) and its equivalent electrical circuit (b).

The electrostatically driven and sensed microbeam resonator described in figure 2.5 generally vibrates at the same frequency as that of the excitation AC signal, which can be characterized as a harmonically excited oscillating system. The governing equation of the mechanical motion in the harmonic system is given by

$$m\frac{d^2u}{dt^2}+c\frac{du}{dt}+(k-k_e)u=f_e(t) \tag{2.49}$$

where k_e is the effective electrical spring constant. $f_e(t)$ is the electrostatic force acting on the moving plate

$$f_e(t)=U_{DC}\frac{\partial C}{\partial u}U_{AC}=\eta U_{ac} \tag{2.50}$$

From LRC circuit theory the voltage related to the motion current i_m across the beam resonator can be represented by the following differential equations in terms of charge q, inductance L_m, capacitance C_m and resistance R_m

$$U_{ac}(t)=L_m\frac{d^2q}{dt^2}+R_m\frac{dq}{dt}+\frac{q}{C_m}=L_m\frac{di_m(t)}{dt}+R_mi_m(t)+\frac{1}{C_m}\int i_m(t)dt \tag{2.51}$$

where Lm , Rm , and Cm are the equivalent inductance, resistance, and capacitance, respectively, $i_m(t)$ is the electromechanically induced motional current.

By substituting $f_e(t)$ (equation (2.50)) and $i_m(t)$ (equation (2.47)) into equation (2.49), the analogous differential equation for the electromechanical beam becomes

$$U_{ac}(t)=\frac{m}{\eta}\frac{d^2u}{dt^2}+\frac{c}{\eta}\frac{du}{dt}+\frac{(k-k_e)}{\eta}u \tag{2.52}$$

then

$$U_{ac}(t)=\frac{m}{\eta^2}\frac{di_m(t)}{dt}+\frac{c}{\eta^2}i_m(t)+\frac{(k-k_e)}{\eta^2}\int i_m(t)dt \tag{2.53}$$

By comparing equation (2.51) and (2.53), the equivalent electrical parameters such as inductance, resistance, and capacitance can be extracted for the electromechanical microbeam as follows

$$L_m = \frac{m}{\eta^2} \qquad R_m = \frac{c}{\eta^2} \qquad C_m = \frac{\eta^2}{(k - k_e)} \tag{2.54}$$

where $\eta = U_{DC} \frac{\partial C}{\partial u} \approx U_{DC} \frac{C_0}{d}$.

The equivalent electrical circuit given in figure 2.5(*b*) resembles that of a crystal resonator. It can be used to determine the frequency response of the electromechanical systems, thereby, conveniently allowing the use of powerful analytical tools developed for electrical network theory, for instance, circuit simulation software, such as SPICE.

Besides the derived equivalent electrical components L_m, C_m and R_m, the vacuum capacitance, C_o, comprised of the lower electrode and the upper beam, is connected to the equivalent circuit in parallel, contributing the feedthrough current i_0 to the expected useful motion current i_m. In addition, the effect of parasitic capacitances arising from the bond pads and wires and resistances from the doped polysillicon beam and electrode in the electrical circuit should be considered for the electromechanical beam when its equivalent electrical circuit is used to analyze the performance of the system.

Chapter 3 Mechanisms of Sensing and Actuating

The excitation and detection of the mechanical beams can be performed in a variety of ways, such as piezoresistive, piezoelectric, capacitive, optical, magnetic, acoustic methods. The understanding of the operation mechanisms of these methods for excitation and detection is necessary for selection of the appropriate testing techniques. In this chapter some of typical electrical and optical methods will be reviewed concerning their working principles, and their advantages and disadvantages will be discussed.

3.1 Electrical Techniques

3.1.1 Piezoresistive Sensing

Piezoresistive sensing utilizes special resistors that their resistance varies with change of their physical dimensions resulted from external force such as pressure. It can be used to measure strain or displacement of movable structures. Piezoresistive sensor, often used as a strain sensor, is usually constructed by building the piezoresistive materials on the surface of a movable structure. The deflection of the movable structure leads to change in physical dimension of the resistor, resulting in the change of resistance due to the piezoresistive effect, as expressed in the following formula [1]:

$$\frac{\Delta R}{R} = (1+2v)\frac{\Delta l}{l} + \frac{\Delta \rho}{\rho} \tag{3.1}$$

where ΔR is the change of the resistance, R is the original resistance, v is the Poisson ratio, Δl is the length change of the resistor, l is the original length of the resistor, and $\Delta \rho$ and ρ represent the resistivity change and resistivity of the resistor, respectively.

It can be easily found out that the resistance of the resistors used for the piezoresistive sensor is proportional to the external force when the resistivity change is ignored since the dimension change is proportional to the applied force.

The sensitivity of the sensors can be represented by the gauge factor which is defined as:

$$GF = \frac{\Delta R / R}{\Delta L / L} = \frac{\Delta R / R}{\varepsilon} = (1 + 2v) + \frac{\Delta \rho / \rho}{\varepsilon} \tag{3.2}$$

The gauge factors of various types of strain sensors show much difference, for example, semiconductor sensors have GF ranging from 80-200, much larger than that of metal sensors from 1-5 [1].

The performance of the piezoresistive sensors is very much susceptible to temperature. The sensitivity of the sensors decreases as temperature increases. Hence, temperature compensation is necessary for their use (for example, using Wheatstone bridge). In addition, any residual stress generated during fabrication will also influence the sensitivity of the sensors.

3.1.2 Capacitive Coupled Detection

Capacitive sensing utilizes a capacitor that its capacitance changes due to the deformation of structure. Through capacitive coupling electrical signals (current) is induced by mechanical motion. A typical structure of capacitive sensor is composed of two parallel plates. Its capacitance is expressed as:

$$C = \frac{\varepsilon A}{d} \tag{3.3}$$

where A is the area of the plates and d is the distance between the two plates, ε is the permittivity of the dielectric between the two plates.

The commonly used forms of capacitive sensor include various membranes applicable to the fields of microphone and pressure sensor. For membranes, the capacitance change is not linear with respect to the structural deformation; also, very small capacitance (1 to 3 pF) requires measurement circuit to be integrated on a single chip. For a comb driver capacitor, its fringing field will become very significant when the size of device reaches at the scale of micrometer.

Capacitive sensing is found to potentially have higher performance than piezoresistive sensing in the application fields requiring high sensitivity, low pressure range and high stability. But, capacitive structures fabricated by surface micromachining often have very small capacitance (femto or atto farad), any potential advantage in signal to noise ratio (SNR) for the capacitive sensing cold be eliminated by the interface electronics.

From the equation (3.3) it can be seen that the change in the distance of the two plates will induce the change of the capacitance. Given an example, if the two plates have a width of 30μm and a length of 300μm, and the distance between the two plates is 2 μm, the resulting capacitance is 40 fF. The change in the capacitance due to a change in the distance (Δ d) is given as follows:

$$\Delta C = C\frac{\Delta d}{d} \tag{3.4}$$

For a maximum deflection of 2 nm the change of capacitance is then ΔC= 0.04 fF. In contrast, a bonding pad usually has a size of (100μm x 100μm) and has a capacitance of 0.17 pF (ε(sio2) = 3.9 ε_0 and assuming d is 2 μm). Thus, during measurement, the percentage of the change in capacitance relative to the total capacitance should be considered in order to detect such a small change in capacitance with available equipments, especially in the RF frequency range.

3.1.3 Piezoelectric Sensing

Piezoelectric sensing is based on the piezoelectric effect of piezoelectric materials. A material displays piezoelectricity when a mechanical stress on a material produces an electrical polarization and reciprocally an applied electrical field produces a mechanical strain. This effect can be applied to the sensing of mechanical stress, or indirectly, the displacement of structure.

The sensitivity of piezoelectric sensors is expressed by the charge sensitivity coefficients d_{ij}, (in units of C/N), which represents the charge generated on the surface of area A in the i axis when a force is applied in the j axis [1]

$$\Delta Q_i = d_{ij}\Delta F_j = d_{ij}\Delta\sigma A \tag{3.5}$$

For a given thickness t of a piezoelectric material, the voltage V induced across the electrode plates, when they are subjected to a force, would be

$$V = \frac{Q}{C} = \frac{d_{ij}}{\varepsilon_0 \varepsilon_r A} t\Delta F_j \tag{3.6}$$

Vise versa, the voltage applied to the piezoelectric material can produce the force which is able to stretch the dimension of the piezoelectric material, typical values of dimensional variation range from 10^{-10} to 10^{-7} cm/V. This is the operation mechanism of piezoelectric actuators.

Piezoelectric materials include quartz, polymer PVDF, Barium Titanate ($BaTiO_3$), Lead Zirconate Titanate (PZT) and Zinc oxide (ZnO). The piezoelectric sensing has found its applications in the fields of SAW devices, pressure sensors, force sensors, speedometers, accelerometers, hydrophones and microphones, etc.

3.1.4 Resonant Sensing

The natural frequency of the resonant microsensor changes when a tensile force is applied. The variation of natural frequency the resonator is directly related to the strain. For example, the natural resonant frequency of a flexure resonator with both fixed ends can be derived in a form [29, 30]:

$$f = \frac{4.73^2 h}{2\pi d^2}\left[\frac{E}{12\rho}\left(1+0.2366\left(\frac{l}{h}\right)^2 \varepsilon\right)\right]^{\frac{1}{2}} \tag{3.7}$$

where f is the natural frequency of the fundamental oscillating mode, l is the length of resonator, h is the thickness of resonator, E is the Young's modulus, ρ is the density of material and ε is the strain generated inside the resonator structure.

Comparing resonant sensing with piezoresistive sensing, the resonator acts as a kind of strain gauge, which relates the strain to the resonant frequency. The relationship between frequency change and strain can be expressed in the following form:

$$\frac{\Delta f}{f} = k_{gf}\varepsilon \tag{3.8}$$

where k_{gf} is the gauge factor of the resonant strain gauge:

$$k_{gf} = \frac{1}{2}\left[0.2366\left(\frac{l}{h}\right)^2\right]\left[1+0.2366\left(\frac{l}{h}\right)^2 \varepsilon\right]^{-1} \tag{3.9}$$

as a simple estimate of k_{gf}, assuming a strain is 100 ppm for a 1.2 mm long, 20 μm wide and 5 μm thick resonator strain gauge, the gauge factor can be as high as 3000; whereas, the piezoresistive strain gauge factor is only about 2. Since the gauge factor directly relates to the sensitivity of the sensor, the resonant sensing can be used as highly sensitive microsensors. However, the resonant sensing usually requires a more complex sensor

structure than piezoresistive sensing does; also, the resonant strain gauges need to be vacuum-encapsulated.

3.2 Optical Detection Methods

3.2.1 Optical Beam Deflection Method

One optical method for detecting the displacement of a micro-scale cantilever is to use a position-sensitive photodetector (PSPD) as implemented in most Atomic Force Microscopy (AFMs) [31-33]. A laser is reflected off the end of a cantilever and received by a bi-cell photodetector. The photocurrent produced in a bi-cell detector changes with the position of the reflected light on the detector, which is directly related to the angle between the surface of the cantilever and the incident laser beam, The detector can sense the displacements of a light beam in the nanometer scale, which is equivalent to the displacement of the cantilever in the subangstrom scale.

As indicated in Figure 3.1 when the cantilever is subjected to a vertical force F, the deflection of the cantilever takes the following form [32]

$$z(x) = \frac{F}{6EI}(3lx^2 - x^3) \tag{3.10}$$

Where l is the length of the cantilever, E is the modulus of elasticity, and I is the moment of inertia of the cantilever. Due to the very small deflection magnitude of the cantilever, the angle of the deflection θ at the end of the cantilever, where x = l, can be approximated as follows:

$$\theta \approx \left.\frac{dz}{dx}\right|_{x=l} = \frac{Fl^2}{2EI} \tag{3.11}$$

By using equation (3.10) and substituting $F = k\Delta z$, (Δz is the deflection of the cantilever).

$$\theta \approx \frac{3}{2}\frac{\Delta z}{l} \tag{3.12}$$

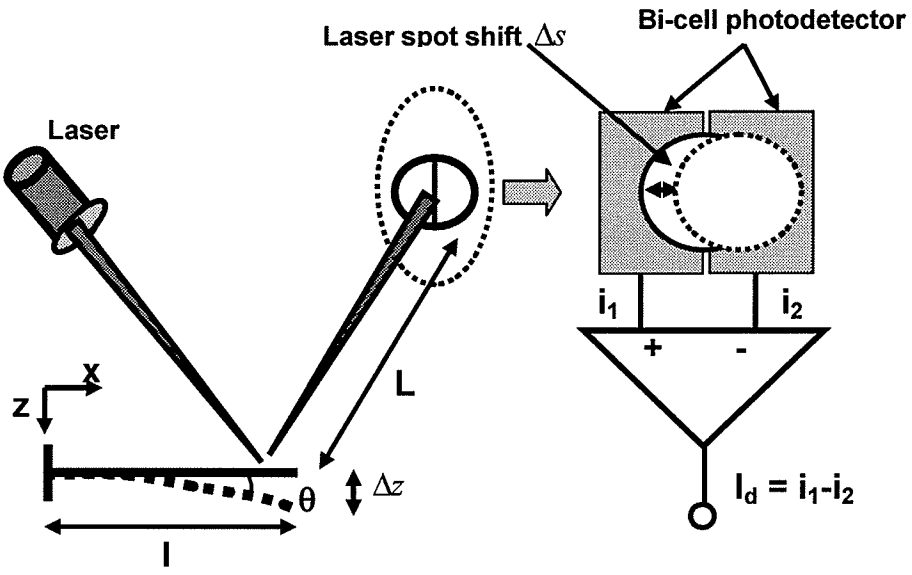

Figure 3.1 Schematic diagram of laser beam deflection system

In Figure 3.1 it is assumed that L is the distance between the bi-cell photodiode and the laser spot on the cantilever and that Δs is the displacement of the reflected laser beam spot on the bi-cell photodetector, approximately $\theta \approx \frac{\Delta s}{L}$. Thus, the relation between Δs and Δz can be found as follows

$$\Delta s \approx \frac{3L\Delta z}{2l} \tag{3.13}$$

It can be seen that the shift of beam spot Δs is proportional to the deflection Δz of the cantilever, i.e., to the force applied to the cantilever.

When the two cells of the photodiode are first positioned and receive an equal optical power from the reflected laser beam, the photocurrents from the two cells are balanced, thus, the bi-cell detector output is zero. Once the cantilever is deflected by Δz, the spot shift of the reflected laser beam will produce the output current proportional to the difference of the irradiance received by the two photocells.

Let us estimate the photocurrent produced in the bi-cell photodetector. If it is assumed that optical beam is monochromatic and its intensity distribution of beam is a Gaussian type. The quantum efficiency of photons to the electrical charges is assumed to be unity. The number of the photons falling on each cell can be calculated by integrating over the portion of the Gaussian beam. The total electrical charges are given by

$$I = 2Nq \int_0^{As} \frac{e^{-\frac{x^2}{2\sigma^2}}}{\sigma\sqrt{2\pi}} \tag{3.14}$$

where N is the total number of photons per second incident on the detector. q is the charge of an electron, and the induced electron current I is calculated using the standard deviation of Gaussian function,

$$I = \frac{P}{h\nu} q \frac{3\sqrt{2}L}{\sigma l} \Delta z \tag{3.15}$$

where σ is standard deviation of Gaussian function. The above equation gives an approximation of the output current produced by the bi-cell photodetector [33].

3.2.2 **Noise in the Optical Deflection Sensor**

There are two main types of noises in the optical detector [33], shot noise induced by the photons randomly falling on the surface of the detector; 1/f noise arising from the low frequency change in the output power of the laser source.

Shot noise, or quantum noise, is a fundamental limit of the nature of light and is characterized by the fluctuation of the photons arriving at the detector. Photoelectrons can be described by Poisson's statistics. The variance of the shot noise is therefore equal to the mean number n_e of the collected photoelectrons during a characteristic time interval, called integration time $\tau = 1/2B$, where B is the detection bandwidth. The ratio of the number of created photoelectrons n_e to the number of incoming photons n_p is called quantum efficiency, $\eta = n_e/n_p$. The ratio of the current i and the optical power p_{opt} is defined as the spectral sensitivity

$$S = \frac{i}{P_{opt}} = \frac{\eta q}{h\nu} \tag{3.16}$$

where $q = 1.602 \times 10^{-19}$ C, $h = 6.626 \times 10^{-34}$ J is Planck's constant, and ν is the light frequency. The variance $\langle i_{SN}^2 \rangle$ of the shot noise current is given by the number of electrons n_e generated in the photodiode in the bandwidth B

$$\langle i_{SN}^2 \rangle = 2qBn_e \tag{3.17}$$

where B is the noise bandwidth. If the dark-current i_d, which is the remaining current when the photodetector is not exposed to light, is considered, the electrical power for the shot noise within the frequency bandwidth B can be written as

$$P_{SN} = \langle i_{SN}^2 \rangle R_0 = 2qB(SP_{tot} + i_d)R_0 \tag{3.18}$$

If the total electrical power P_{tot} is much larger than the dark current i_d, the electrical power of the shot noise from the detector becomes

$$P_{SN} = 2qBSP_{tot}R_0 \tag{3.19}$$

The performance of the optical beam deflection sensor is mostly limited by the shot noise.

Another noise source is 1/f noise which becomes important at low frequency. However, the optical beam deflection system is insensitive to 1/f noise because the 1/f noise from the bi-cell photodetector is cancelled each other.

The sensitivity of the optical beam-bounce system was estimated to be 7.9 $x10^{-6}$ nm/$\sqrt{Hz}$ [31]. In order to detect the correct signals related to the mechanical beam vibration, the spot size of the laser beam should be focused as small as possible, If the laser beam diameter is large, very little of the light will fall on the cantilever and most of the light will be due to the reflections off the substrate. In addition, the micromachined cantilevers and clamped beams tend to be fabricated smaller and smaller with higher and higher resonant frequencies, high-speed PSPD is required for the measurement of the resonance of micromachined vibrating elements.

3.2.3 Interferometry Techniques

Apart from the optical beam deflection method using position sensitive photodetector for measuring very small displacement of objects, interferometric techniques have been used in the fields of high-precision measuring systems and displacement sensors [33, 34]. Interferometric techniques can be mainly placed into two categories; static (homodyne) and dynamic (heterodyne) methods. Homodyne works only with one optical frequency for the interfering light beams. Heterodyne uses two or more frequencies for the interfering waves. Fabry-Perot and Mach-Zehnder interferometers are two kinds of common configurations of interferometers.

The intensity of the interference light of two beams can be deduced as follows [34]:

$$I = I_0 + I_r + 2\sqrt{I_0 I_r}\cos(\Delta\omega t + \Delta\phi(t)) \tag{3.20}$$

The interference signal is of sinusoidal form with the frequency of $\Delta\omega$ and the amplitude of $2\sqrt{I_0 I_r}$, and Io + I_r is the dc signal. The information of the moving object is related to the phase variation $\Delta\phi(t)$. Only the ac component is interested, the electrical signal takes the following form:

$$I(t) = vS2\sqrt{I_0 I_r}\cos(\Delta\omega t - \Delta\phi(t)) \tag{3.21}$$

where $\Delta\omega = \omega_1 - \omega_2$ is the frequency difference of the two interfering lights, and $\Delta\phi(t) = \phi_1(t) - \phi_2 = \frac{4\pi}{\lambda}x(t) + \phi_0$, x(t) is the displacement of object; S is the detector sensitivity, and v is the visibility of the interference in the following form

$$v = \frac{I_{\max} - I_{\min}}{I_{\max} + I_{\min}} \tag{3.22}$$

Equation (3.21) is a phase modulated signal with carrier frequency $\Delta\omega$ and phase modulation $\Delta\phi(t)$.

When the frequencies of the two interfering beams are different, i.e. $\Delta\omega = \omega_1 - \omega_2 \neq 0$, method based on the equation (3.21) is called heterodyne interferometry, its commercial instrument is called velocimeter.

When the interfering lights have the same frequency, i.e., $\Delta\omega = \omega_1 - \omega_2 = 0$, the interference intensity becomes

$$I(t) = a\cos(\frac{4\pi}{\lambda}x(t) + \phi_0) \tag{3.23}$$

$$I(t) = a\cos(\beta\cos(\omega_s t + \varphi) + \phi_0) \tag{3.24}$$

where $x(t) = x_0\cos(\omega_s t+\varphi)$, and $\beta = 4\pi x_0/\lambda$.

Equation (3.24) can be expanded into the following form with the Bessel function $J_n(\beta)$, for $\phi_0 = (2n + 1)\pi/2$

$$I(t) = a\cos\phi_1[J_0(\beta) - 2J_2(\beta)\cos 2(\omega_s t + \varphi) + ...] + a\sin\phi_1[2J_1(\beta)\cos(\omega_s t + \varphi) - 2J_3(\beta)\cos 3(\omega_s t + \varphi) + ...] \quad (3.25)$$

for $\beta << 1$

$$I(t) \approx (-1)^n a\beta\cos(\omega_s t + \varphi) \quad (3.26)$$

It is obvious that when the vibration amplitude of object is much smaller than wavelength, the interference intensity is proportional to the object displacement. From the above equations the interferometer phase angle $\phi_0 = (2n + 1)\pi/2$ is required to get an optimum sensitivity. Method based on the equation (3.26) is called homodyne interferometry. In homodyne interferometer, noise is the limiting factor for the resolution. Typical resolution values lie between 10 and 100 $x10^{-12}$m, depending on the quality of the equipment.

3.2.4 Fabry-Perot Optical Fiber Interferometer

Optical fiber interferometers usually have the two types: Mach-Zehnder and Fabry-Perot, and they have been known as extremely compact and economic displacement sensors with high sensitivity [35-39]. The operation principle of the Fabry-Perot optical fiber interferometer is schematically shown in figure 3.2. The laser is coupled into the fiber1 and propagates through the optical coupler to fiber2. Then, one part of light in fiber 2 is reflected from the end face of the fiber 2 and other part of light is reflected from the moving object and returned back into the fiber 2. The two parts of light in fiber 2 interferes with each other, resulting the interfering signal, which propagates through the

coupler to the fiber 3 then received by the photodetector. The intensity of the interfering signal changes periodically which depends on the distance x(t) between the end of fiber2 and the object as follows:

$$I = I_1 + I_2 + 2\sqrt{I_1 I_2}\cos(\frac{4\pi}{\lambda}x(t) + \phi_0) \tag{3.27}$$

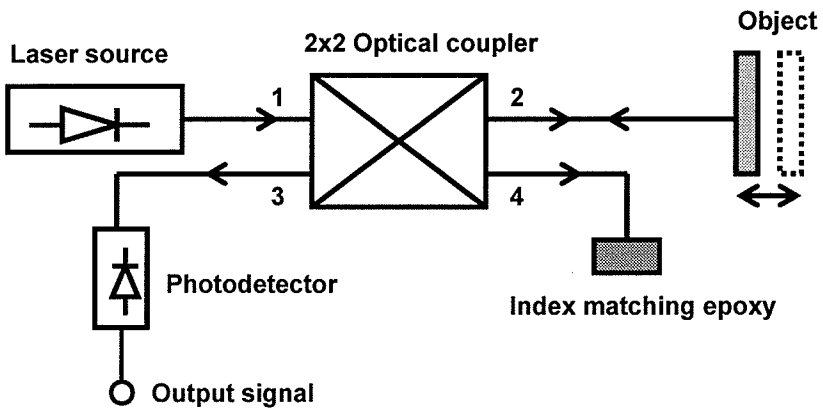

Figure 3.2 Schematic diagram of the Fabry-Perot Optical Fiber Interferometer

In Fabry-Perot optical fiber interferometer $I_1=r_1I_0$ is the intensity of light reflected from the end face of fiber2 and $I_2 = (1\text{-}r_1)2rI_0$ is the intensity of light reflected from the moving object and returned into fiber2, where I_0 is the intensity of laser coupled into fiber2, r_1 is the reflectivity of the end face of fiber 2 and r is the reflectivity of moving object. For quartz fiber $r_1 = 0.04$ is Fresnel reflectivity of boundary surface between the interface of glass with refractive index n=1.5 and air with refractive index n=1. Thus, when the distance between interferometer mirrors equals x_0, the light intensity detected by a photodetector is described as follows:

$$I = I_0(r_1 + (1-r_1)^2 r + 2(1-r_1)\sqrt{rr_1}\frac{\sin\xi}{\xi}\cos(\frac{4\pi}{\lambda}x_0\sin(\omega t+\varphi)+\phi_0)) \tag{3.28}$$

where $\xi = \pi\frac{l}{l_c}$, $\sin\xi/\xi$ represents the degree of coherence, which is introduced because any light source can not be exactly monochromatic. The radiation of laser diode consists typically of several frequency modes and the total width of the spectrum $\Delta\lambda$ is equal approximately to 3-5 nm. Coherence length l_c of such a radiation can be estimated by $l_c = \frac{\lambda^2}{\Delta\lambda}$. The visibility of interference fringes will be affected by coherence length of the light. Increase in the path difference of interfering beams decreases the visibility of interference pattern. When the path difference reaches the coherence length, the visibility equals zero.

Because the intensity of the beam reflected from the end face of fiber is about an order of magnitude less than the intensity of radiation reflected from moving object and returned back into the fiber, 100% visibility of interference can not be achieved even at zero path difference of interfering rays. Thus, the optical power arriving at the photodetector depends upon the distance between fiber and moving object.

If the multiple beam interference produced from the interface between the end of fiber 2 and the surface of moving object is considered instead of the two beams interference described above, the interference intensity of light arriving at the detector is given by [35]

$$\frac{I}{I_0} = \frac{(r_1^2+\beta^2)-2r_1\beta\cos\delta}{(1+r_1^2\beta^2)-2r_1\beta\cos\delta} \tag{3.29}$$

where $\beta = |r_2|F(D/a)$ and $F(D/a) = 1/\sqrt{1+4\theta D/a+4\vartheta^2(D/a)^2}$

In the above equations r_1 and r_2 are the reflection coefficients at the end of fiber and at the surface of moving object, respectively. λ is the wavelength of light, D is the distance between the fiber end and the surface of moving object. $\delta = 4\pi D / \lambda$ is the phase difference induced by the distance D. β is called an electric field damping parameter, which is related to the beam spreading represented by the function F(D/a). a is the diameter of the core of fiber. θ is the half angle of the spreading cone for the single-mode fiber.

When the multiple reflections between the end of fiber and the moving object are ignored the problem can be simplified as the two beams interference problem as described above [33].

Chapter 4 Fabrication Process and Testing Set-up

4.1 MEMS Technology

Micromachining technology for the fabrication of micromechanical resonators in MEMS will be briefly described in order to better understand structures of the resonators. MEMS technology has been developed from the traditional IC industry in which the fabrication process generally includes photolithography, thermal oxidation, doping, diffusion, ion implantation, low pressure chemical vapor deposition (LPCVD), PECVD, evaporation, sputtering, wet etching, plasma etching, reactive-ion etching, ion milling; and the materials are silicon, silicon dioxide, silicon nitride, aluminum [1].

In addition to the above standard IC processes, MEMS has its own special microfabrication techniques, such as anisotropic wet etching of single crystal silicon, deep reactive–ion etching, x-ray lithography, electroplating, etc., and the materials include piezoelectric films (e.g., PZT), magnetic films (e.g., Ni, Fe, Co, and rare earth alloys), high-temperature materials (e.g., SiC and ceramics), mechanically robust aluminum alloys, stainless steel, platinum, gold, sheet glass, plastics (e.g., PVC and PDMS) [2].

Two mostly common used micromachining methods in the MEMS are named as bulk micromachining and surface micromachining based on how to process silicon substrate [40]. Bulk machining builds structures by etching into the body of the silicon substrate to form membranes, trenches and holes, etc., and surface micromachining constructs the micromechanical structural layers by depositing thin films layer by layer on the substrate surface.

Photolithography is a first important process which defines the degree of integrity and the microscopic dimension of microdevices. In the photolithography process a mask, defining the desired pattern of structure, is first designed and fabricated, then it is used to transfer the structure pattern to a photo-sensitive polymer called photoresist which is coated on the substrate. Part of the photoresist can be removed after exposed to UV light, leading to the desired structural pattern forming on the silicon wafer. Then, through the process of etching and depositing, the expected structures can be built on the silicon wafer. Figure 4.1 gives an illustrative diagram of the photolithography process.

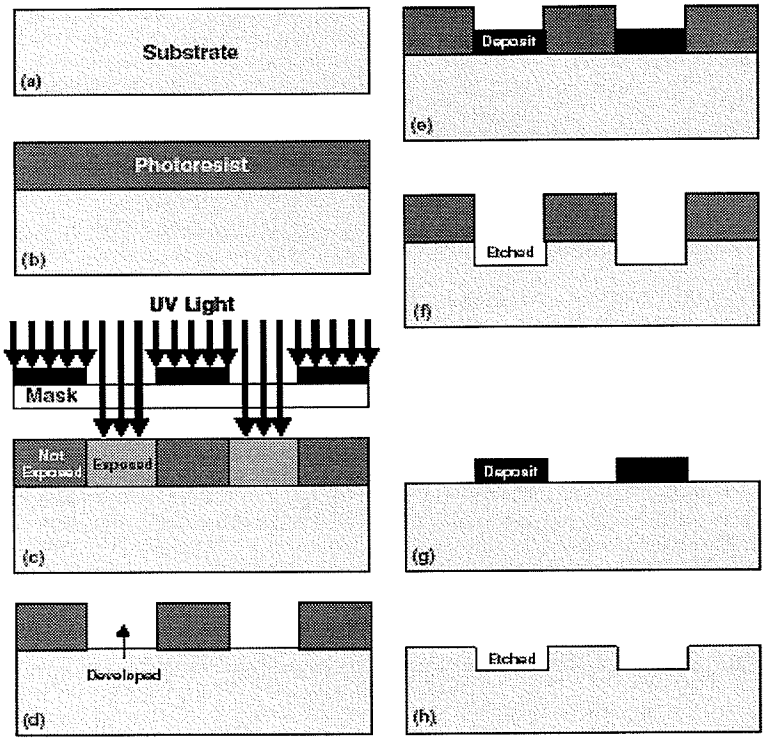

Figure 4.1 Schematic diagram of photolithography process [2].

4.1.1 Bulk Micromachining

Bulk micromachining technique is used to form structures on one side of a wafer in the forms of membranes, trenches and holes, etc. by selectively removing significant

amounts of silicon from the substrate through wet etching and dry etching. Wet etching uses liquid enchants of aqueous chemicals; and dry etching employs vapor and plasma etchants. Figure 4.2 schematically shows some basic forms of the bulk micromachined structures.

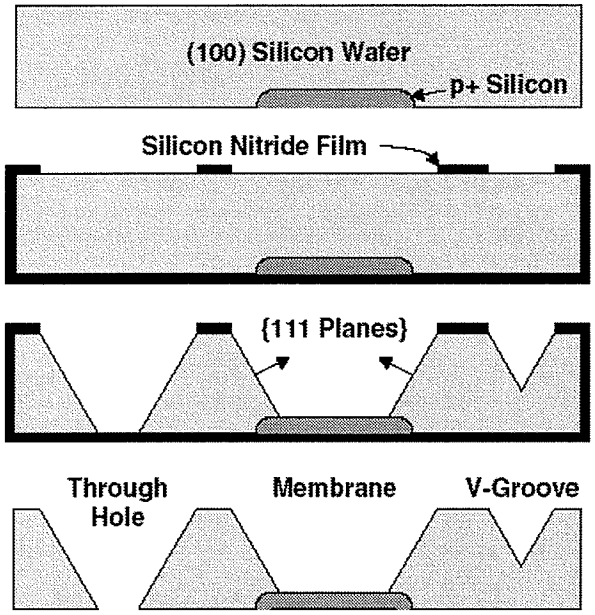

Figure 4.2 Schematic diagrams of bulk micromachined structures [2]

In wet etching process the desired structures on the silicon substrate can be formed by putting the substrate into an etching bath which may be acid or alkaline. Various structures can be created by either isotropic etching or anisotropic etching depending on the materials or the etchants. For the material such as amorphous or polycrystalline wet etching is always isotropic etching. The isotropic etching is not suitable for deep etching due to its undercut effect. For single-crystal silicon anisotropic etching is a very useful way to be used to build the desired structure. Main feature of the anisotropic etching is that etching speed is dependent on the crystal's orientation. The etching slows down

significantly at the (111) planes of silicon relative to other planes. For the wafers with different crystal orientation, different bulk machined features can be achieved. The most common etchants for the anisotropic etching of silicon are alkali hydroxide (KOH, NaOH); ammonium-based solutions (NH_4OH, TMAH) and EDP (ethylene diamine pyrocatechol). In addition, electrochemical etch-stop technique by combining anisotropic etching with boron implantation (P+ etch-stop) can be used to generate various silicon microstructures [1,40].

In dry etching the desired structures on the substrate can be built through chemical or physical interaction between the ions in the gas and the atoms of the substrate. Non-plasma, isotropic dry etching can be possible using xenon difluoride or a mixture of interhalogen gases and provides very high selectivity for aluminum, silicon dioxide, silicon nitride, photoresist, etc.. The most common dry etchings of bulk silicon are plasma etching and reactive ion etching (RIE). The common reactants include chlorofluorocarbon gases, sulfur hexafluoride, bromine compounds and oxygen. The anisotropic dry etching processes are widely used in MEMS because of the geometry flexibility and less chemical contamination than in wet etching. Arbitrarily oriented features can be etched deep into silicon using anisotropic dry etching. Very deep silicon microstructures can be obtained by the deep RIE (DRIE) [1, 40].

4.1.2 Surface Micromachining

Surface micromachining forms structures on the surface of the silicon by depositing thin films as structural layers or sacrificial layers and then eventually removing the sacrificial layers to release the desired mechanical structures. The dimensions of these

surface micromachined structures can be several orders of magnitude smaller than bulk-micromachined structures. The prime advantage of surface-micromachined structures is that they are easy to be integrated with IC components. Surface micromachining requires a compatible set of structural materials, sacrificial materials and chemical etchants. The structural materials must have the physical and chemical properties that are suitable for the desired application. In addition, they must have satisfactory mechanical properties: e.g., high yield and fracture stresses, minimal creep and fatigue and good wear resistance. The sacrificial materials must have good mechanical properties to avoid device failure during fabrication. These properties include good adhesion and low residual stress in order to eliminate device failure by delaminating and/or cracking. The etchants to remove the sacrificial materials must have excellent etch selectivity and be able to etch off the sacrificial materials without affecting the structural ones. In addition, the etchants must have proper viscosity and surface tension characteristics. The common IC compatible materials used in surface micromachining are: first, polysilicon and silicon dioxide family. LPCVD deposited polysilicon as the structural material and LPCVD deposited oxide as the sacrificial material. The oxide is readily dissolved in HF solution without affecting the polysilicon. Silicon nitride is often used for electrical insulation. Second, Polyimide and aluminum family, in this system polyimide is the structural material and aluminum is the sacrificial material. Acid-based etchants are used to dissolve the aluminum sacrificial layer. Third, Silicon nitride and polysilicon group, silicon nitride is used as the structural material, whereas, polysilicon is the sacrificial material. In this material system, silicon anisotropic etchants such as KOH and EDP are used to dissolve polysilicon. Fourth, Tungsten and silicon dioxide; CVD deposited tungsten is used as the structural material

with oxide as the sacrificial material. HF solution is used to remove the sacrificial oxide. Other IC-compatible materials such as silicon carbide, diamond-like carbon, zinc oxide, gold, etc. are also used. Figure 4.3 gives a simple example of how surface micromachining works.

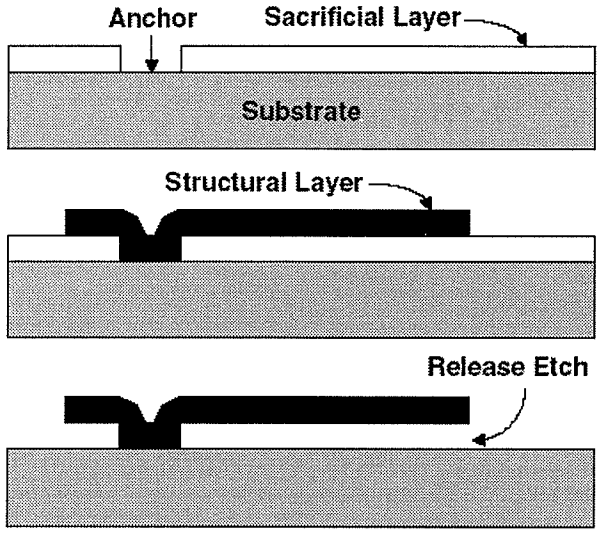

Figure 4.3 Structural and sacrificial layers formed by surface micromachining [2].

Surface micromachining could also be performed using dry etching methods. Plasma etching of the silicon substrate with SF_6/O_2-based and CF_4/H_2-based gas mixtures is advantageous since high selectivity for photoresist, silicon dioxide and aluminum masks can be employed. However, when plasma etching is applied, a large undercut of the mask is produced due to the isotropic fluorine atom etching of silicon which is known to be high compared with the vertical etch induced by ion bombardment. In contrast, reactive ion etching of poly-Si using a chlorine/fluorine gas combination produces virtually no undercut and almost vertical etch profiles when photoresist is used as a masking material.

Besides bulk and surface micromachining, other fabrication techniques have also been developed [2], such as LIGA (lithographe (ltography), galvanoformung (plating) and

abformung (molding)), SUU-8 (cheap alternative to LIGA) and plastic molding with PDMS (Polydimethylsiloxane).

In addition, wafer bonding is also very important processes for successful operation of the fabricated microdevices. Anodic bonding, fusion bonding, eutectic bonding and adhesive bonding have been developed to bond silicon, glass, metal and polymeric substrates [1, 40].

4.1.3 MUMPs Technology

The Multi-User MEMS Processes (MUMPs) was developed to serve the MEMS foundries in order to reduce the cost of microfabrication due to very expensive fabrication facility [41]. MUMPs is a three-layer polysilicon surface micromachining process which has general features of a surface micromachining process: (1) polysilicon is used as the structural material, (2) deposited silicon oxide is used as the sacrificial layer, (3) silicon nitride is used as electrical isolation between the polysilicon and the substrate, (4) metal (usually gold) is the top layer of the device and can be used as a conductive layer.

The MUMPs process uses a 100 mm n-type (100) silicon wafer of 1-2 Ω-cm resistivity. The surface of the wafers is highly doped with phosphorus. First, a silicon nitride layer is deposited on the wafers as an electrical isolation layer, followed by the direct deposition of a polysilicon film called Poly0. Poly0 can not be released in the MUMPs process; it is typically used as a ground plane or for routing purposes. Poly0 is then patterned by photolithography process that includes the coating of the wafers with photoresist, the exposure of the photoresist to the UV light with the appropriate mask, and the developing

of the exposed photoresist to create the desired etch mask for subsequent pattern transfer into the underlying layer. After the photolithography process, the Poly0 layer is etched in a special system. Following that, a phosphosilicate glass (PSG) sacrificial layer of 2.0 m is then deposited and annealed. The layer of PSG, known as first oxide, will be removed at the end of the whole MUMPs process to free the first mechanical layer of polysilicon. After the first oxide is patterned, the first structural layer of polysilicon (Poly1) is deposited in a thickness of 2.0 m. The polysilicon is lithographically patterned using a mask designed to form the first structural layer Poly1. After Poly1 is etched, a second PSG layer (Second Oxide) is deposited, annealed, patterned and etched so as to form holes and anchors to provide a mechanical and electrical connection between the Poly 1 and Poly 2 layers. The Poly2 structural layer is created as same as Poly 1. The Poly1 and Poly2 layers are the mechanical structural layers in MUMPs process because they both can be released by etching the sacrificial oxide layer at the end of the process. A 0.5 m metal layer is finally deposited, which provides for probing, bonding, and electrical routing. During the processes the photoresist can be stripped by immersing the devices in acetone for 3 minutes, and then in de-ionized (DI) water for 1 minute. The sacrificial oxides can be remove for releasing the mechanical structure by putting the chips in a bath of 49% HF for 1.5 - 2 minutes followed by several minutes in DI water and then alcohol for 2 minutes to reduce friction, followed by 30 minutes in an oven at 90 °C [41].

Our resonators were provided by Gennum Corporation and were fabricated in a process very similar to the MUMPs process. Figure 4.4 shows a typical mechanical structure of micromachined resonator provided by Gennum Corporation, which is a clamped-clamped mechanical resonator.

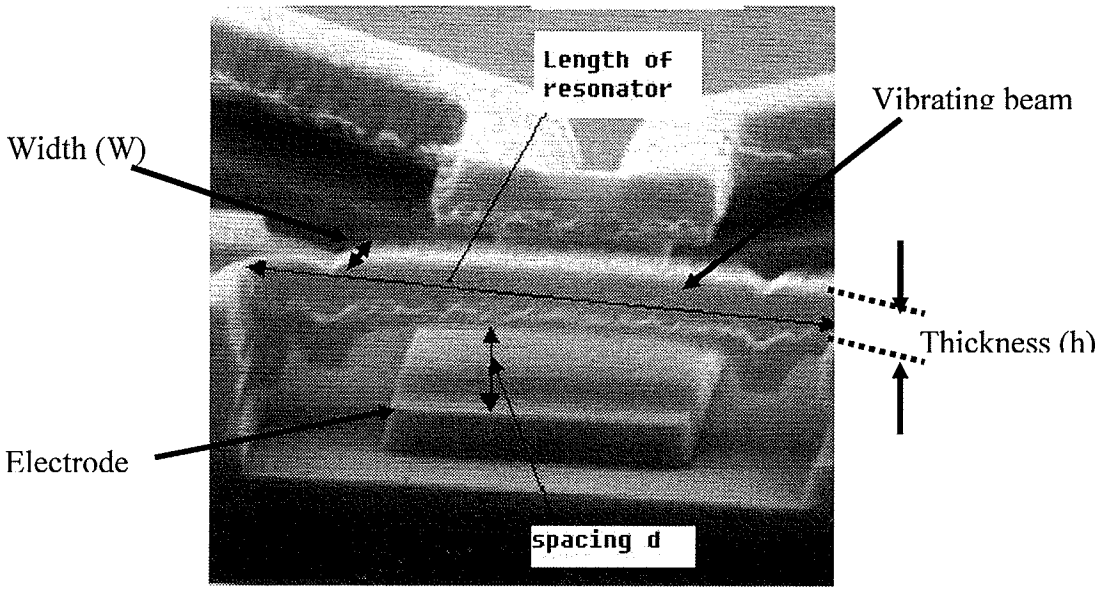

Figure 4.4 SEM picture of a clamped-clamped micromachined resonator

Based on the information provided by Gennum Corp, the material for the resonator beam is P-doped PolySi with sheet resistance of 4 Ω/sq, and residual stress is between -10 and -17 MPa (compressive). Young's modulus E is 165GPa and density ρ is 2330 kg/m^3. The samples offered by Gennum Corp. include the resonators with the resonant frequency of about 11 MHz and 150 kHz, respectively. For the 150 kHz resonator, the polySi beam has a length (L) of 300 um and width (W) of 30 um and thickness (h) of 1.6 um, the spacing between the beam and the underneath electrode d is about 2.0 um. For the 11 MHz resonators (18C and FL1 samples), d is around 150 nm, L is about 30.6 um, W is 9 um and h is about 1.6 um. These data were provided Gennum Corp.

Figure 4.5 shows the optical pictures of the resonators taken in our lab. Figure 4.5 (a) is the 150 kHz resonator, figure 4.5(b) is the 11 MHz resonator with one beam and figure 4.5 (C) is the 11 MHz resonator with 5 beams.

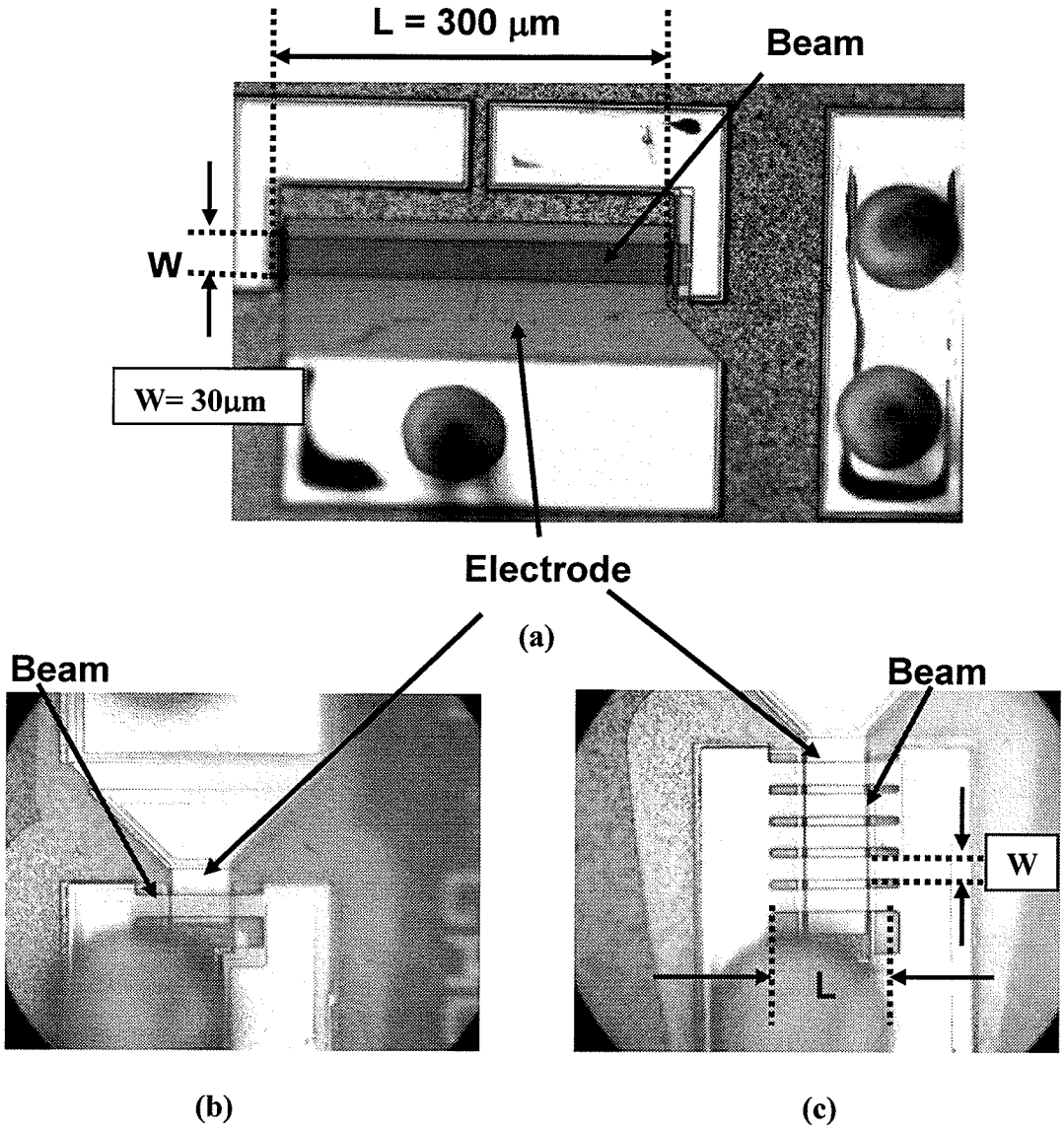

Figure 4.5 Pictures of the C-C resonators taken by optical microscopy. (a) is 150 kHz resonator; (b) is 11 MHz resonator (L=30.6 μm, W=9 μm) and (c) is 11MHz resonator with five parallel beams

4.2 Experimental Set-up

4.2.1 Capacitive Coupled Sensing With Network Analyzer

Testing of electromechanical devices is often performed using Network analyzer by measuring transmission S-parameter S_{21}. The 8753E network analyzer in our lab with bias-tee circuit can provide DC bias voltage up to 30 V to the testing device. In this experiment the two RF ports of network analyzer are directly connected to the input and output of the resonator, respectively, without using an amplifier. No attempt is made to match the resonator to the testing circuit, as doing so would load the device, reducing its Q. The large mismatch between the 50Ω impedance of the test equipment and the resonator will result in a rather high, but tolerable, insertion loss in the measurement [42]. DC bias voltage from a DC power supply is applied to the resonator through a bias-T circuit embedded inside network analyzer. The resonator is positioned in a vacuum chamber which can be pumped with mechanical pump and turbo molecular pump. Figure 4.6 gives the schematic diagram of such an experimental setup.

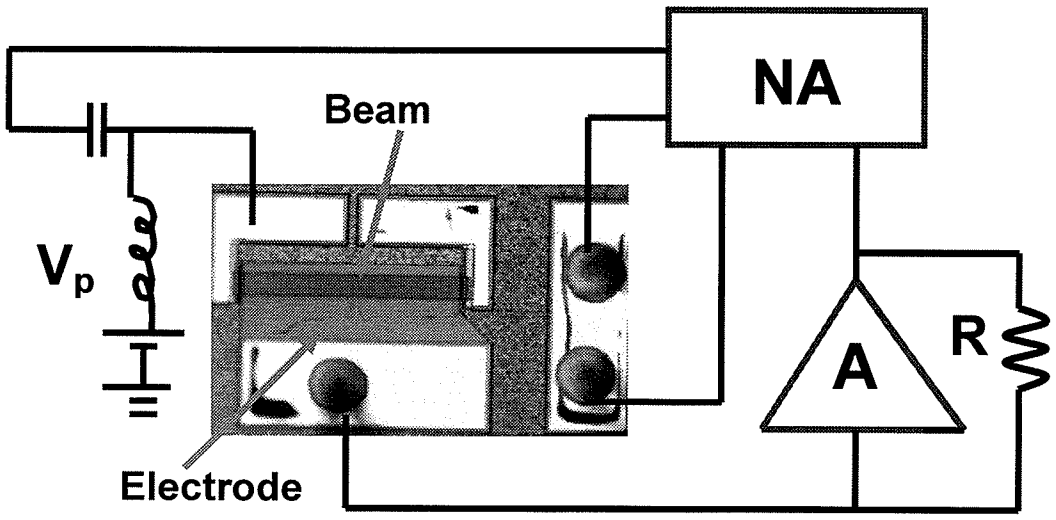

Figure 4.6 Experimental set-up by capacitive sensing with network analyzer

4.2.2 Capacitive Coupled Sensing by Lock-in Technique

The 150 kHz C-C resonator can also be measured by capacitive coupled exciting and sensing using lock in technique as shown in figure 4.7. The resonator was placed in a vacuum chamber under pressure less than 10^{-3} Torr. An exciting AC signal and a DC bias voltage were supplied with the DS345 30MHz Synthesized Function Generator. The DC bias voltage applied varies from 0 V to 10 V, and the sinusoidal driving voltage of 20 mV was first selected. The capacitive coupled signal from the output pin of the resonator was directly sent to the SR844 Lock-in amplifier which was synchronized with the driving signal. The output signal of the lock-in amplifier was then recorded using TDS3012 Digital Phosphorus Oscilloscope. Lock-in Amplifier offers higher sensitivity compared to the network analyzer.

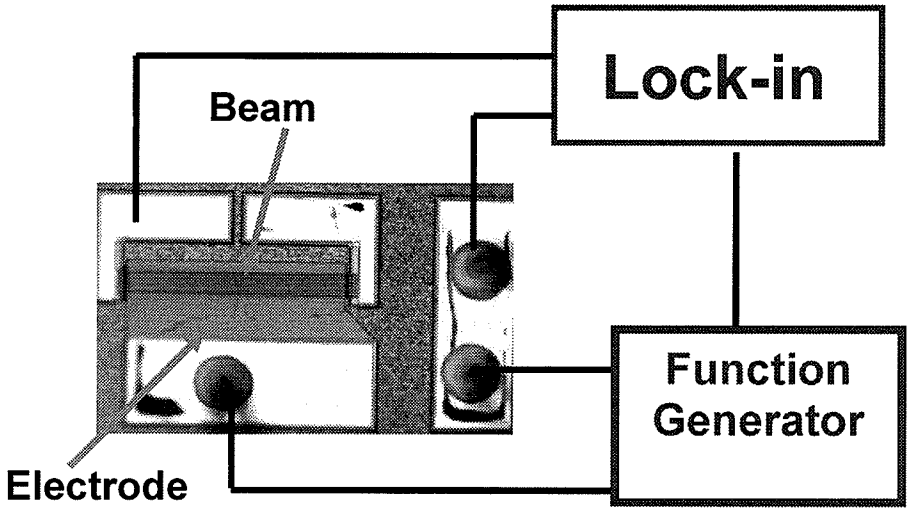

Figure 4.7 Experimental set-up using capacitive sensing with Lock-in technique

4.2.3 Optical Beam Deflection Detection

Optical beam deflection method is capable of detecting sub-nanometer movement. In figure 4.8 laser is focused on the center of the resonator beam, the reflected light is

collected by the bi-cell photodetector, which output the differential signal proportional to the vibration amplitude of the beam. The signal was fed into lock-in amplifier to perform frequency sweep. The differential signal from the photodetector can also directly be recorded using spectrum analyzer,

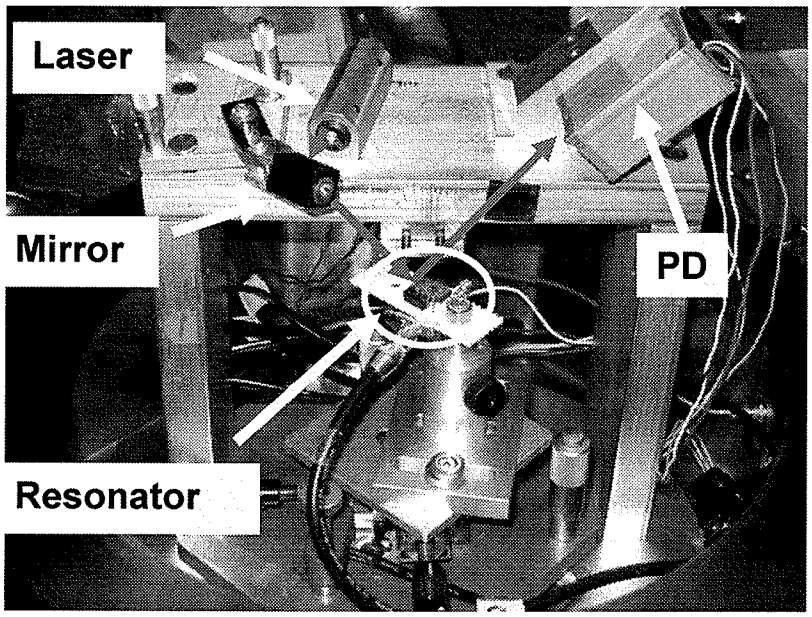

(a)

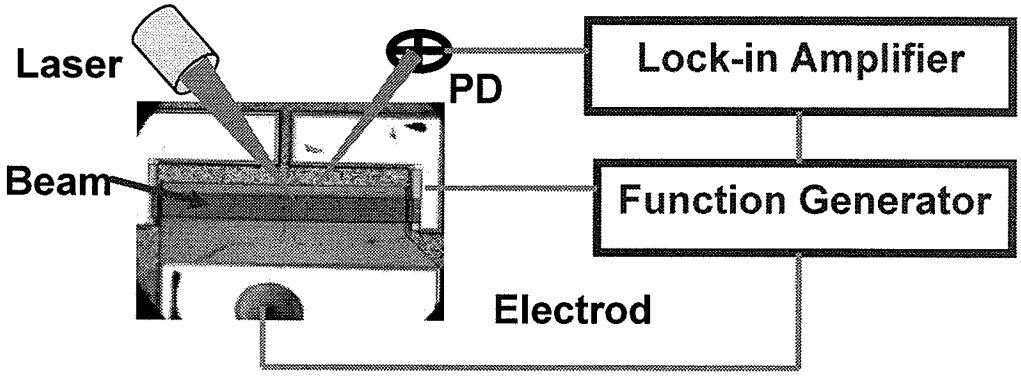

(b)

Figure 4.8 (a) Experimental setup of laser beam deflection and (b) schematic diagram.

4.2.4 Optical Fiber Interferometer

Figure 4.9 shows the experimental set-up of optical fiber interferometer. Tunable laser (Agilent 81689A) was used as a light source. The light was directed into a 2x2 single mode directional coupler using single mode fiber. The coupler splits the incident optical power equally and output one part to the resonator through tapered fiber and other part to the matching index epoxy. Approximately 4% of the light in tapered fiber (Oz Optics LTD) is reflected from the glass-air interface at the cleaved end of the fiber. The other 96% of the light pass through the fiber and incident on the resonator, part of which is reflected back into the fiber and interferes with the light reflected from the end of fiber. The intensity of total interfering light depends on phase difference between the light beams from the end of fiber and the resonator, i.e., the distance between the end of fiber and the resonator. The half of the interfering light is directed into a photodetector (THORLAB Model D400FC InGaAs Detector) through the coupler. The power of the interfering light, carrying the information of phase difference, is converted into electrical signal which is fed into lock-in amplifier. The resonator is exited by an AC signal with a DC bias voltage from Function Generator. When the AC exciting signal is swept around resonant frequency of the resonator, the lock-in amplifier detects amplitude and phase of the input signal related to the vibration of the resonator and gives a signal which can be recorded by oscilloscope.

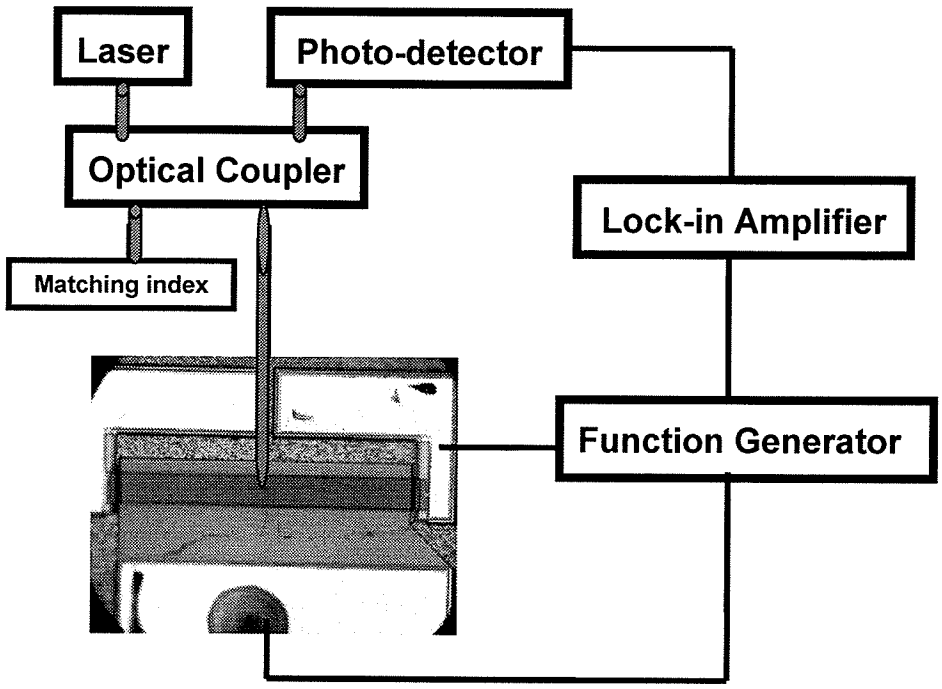

(a)

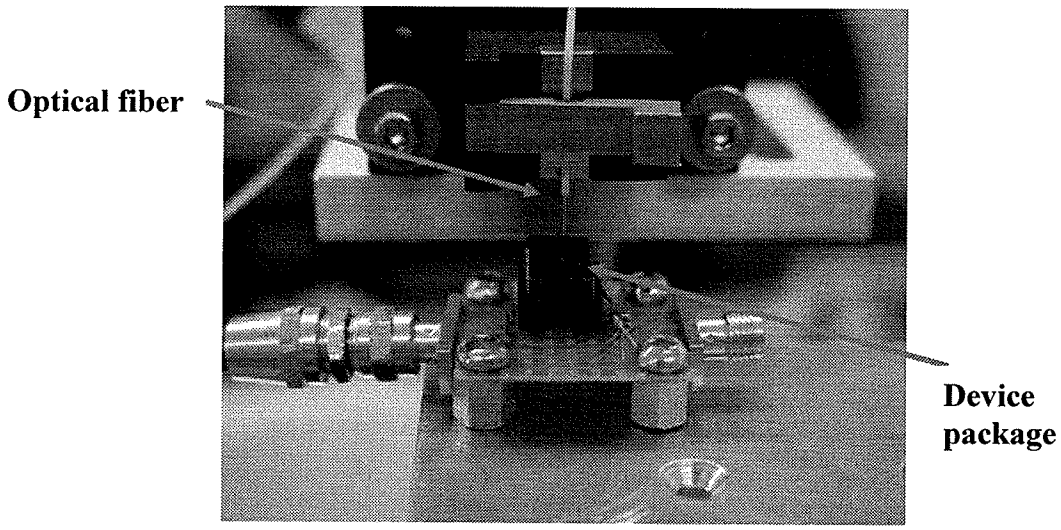

(b)

Figure 4.9 Schematic diagram of measurement by optical fiber interferometer is shown in (a) and experimental setup in (b)

Chapter 5 Experimental Results and Analysis

The experimental characterization of dynamic vibration behavior of micromachined resonators was performed using both electrical and optical methods as described previously. The resonant frequency of resonators and its dependence upon DC bias voltage are first important properties to be determined. The experimental data for them will provide direct feedback for the design principle and the manufacturing processes. Nonlinear vibration behavior is a very interesting phenomenon, it is necessary to understand its origins and its behavior under various operating conditions. In addition, the experimental data will demonstrate advantages and disadvantages of the electrical measurements and optical measurements; data analysis will give out the electromechanical parameters and equivalent electrical components.

5.1 Measurement of 150 kHz Resonator

5.1.1 Capacitive Coupled Measurement

The clamped-clamped resonator with the frequency of 150 kHz was first measured in a vacuum chamber under pressure less than 10^{-3} Torr using capacitive coupled technique. Figure 5.1 shows measured data by sweeping frequency from 100 kHz to 200 kHz. The exciting AC voltage of 20 mV and the DC bias voltage of 10 V were applied. It can be first seen that output signal from lock-in amplifier displays an absorption-type peak around the frequency of 144.500 kHz accompanied by a phase change from 10 degree to 50 degree. Reason for this is not clear. Data also clearly show that another sharp peak appears at the frequency of 147.516 kHz, and the peak is accompanied by a small phase

change from 45 degree to 25 degree. Figure 5.2 shows the data obtained within a narrow sweeping frequency range. In addition, the data indicates the significant existence of large background signals, leading to the very poor peak amplitude. The sharp drop occurred just above the peak frequency might be linked to the existence of parallel-resonance right following series resonance [42]. Although the 150 kHz resonator was first examined using network analyzer, no any resonant peak was observed when frequency was swept near the frequency of 150 kHz.

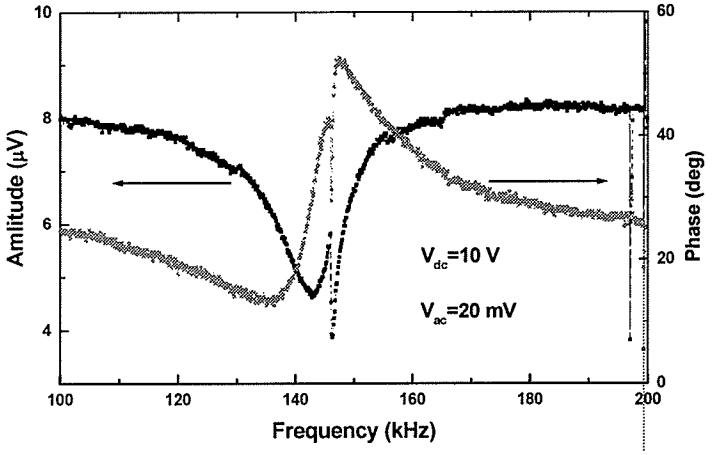

Figure 5.1 Amplitude and phase versus sweeping frequency using capacitive coupled measurement.

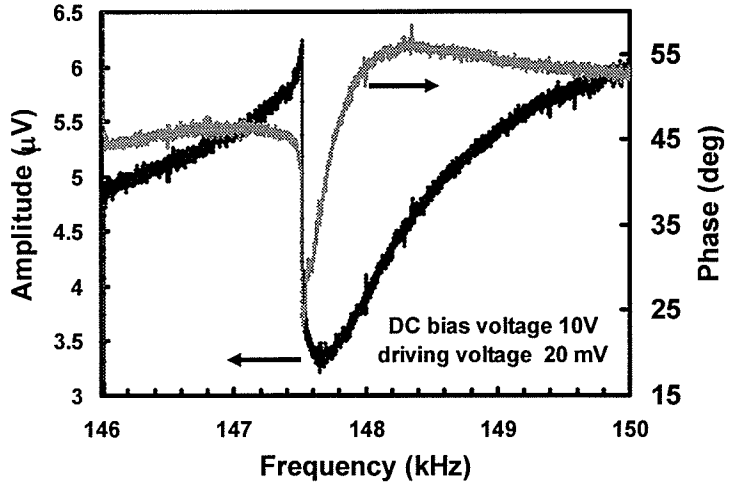

Figure 5.2 Data collected near peak frequency by capacitive coupled measurement.

5.1.2 Measurement by Optical Beam Deflection

5.1.2.1 Resonant Frequency

This 150 kHz resonator was also measured under mechanical pumped vacuum using optical beam deflection technique. Figure 5.3 shows the data measured with the DC bias voltage of 10 V and the AC driving voltage of 20 mV within sweeping frequency range of 100 kHz to 200 kHz. The data collected in a narrow frequency range are shown in figure 5.4. Here, the amplitude peak was found at frequency of 147.080 kHz. By comparing with the data obtained above using capacitive coupled method, two measured resonant frequencies are very close; also, it is obvious that the signal/noise ratio for optical method is much better. In addition, the data in figure 5.4 shows a rapid jump in amplitude at the resonant frequency, this phenomenon is nonlinear behavior and will be discussed in detail later.

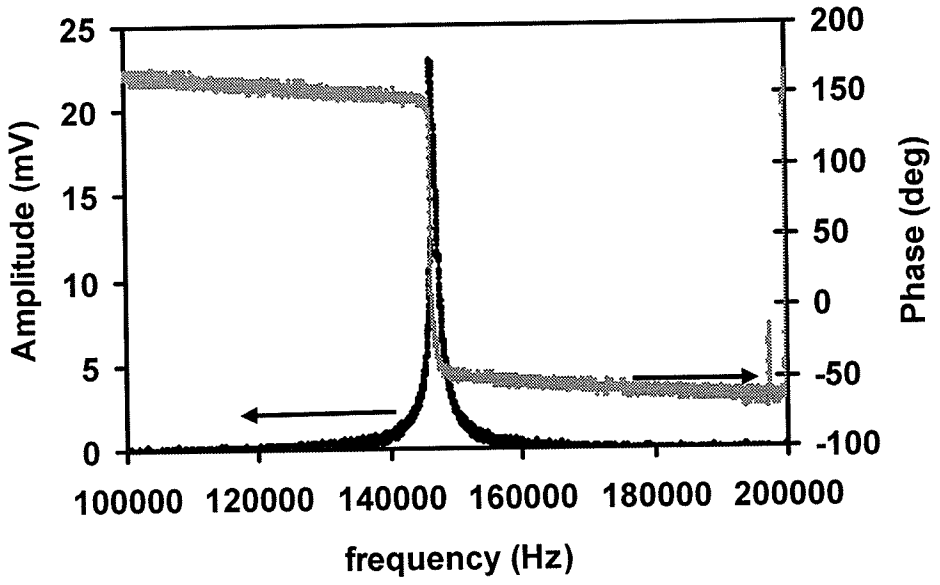

Figure 5.3 Amplitude and phase versus frequency measured by optical beam deflection.

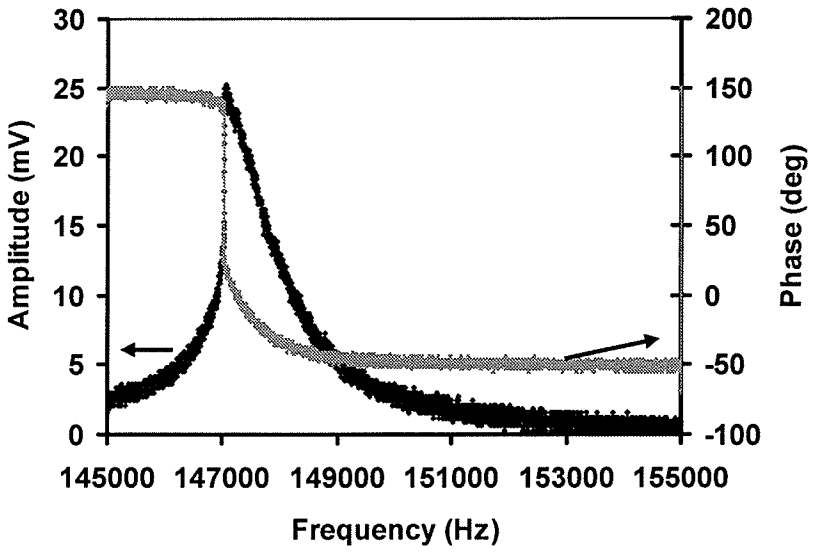

Figure 5.4 Measurement data by frequency sweeping using optical beam deflection

Theoretically, the principal natural resonant frequency can be calculated using the following equation derived from the equation (2.11) in chapter 2:

$$f_0 = 1.03\sqrt{\frac{E}{\rho}}\frac{h}{L^2} \qquad 5.1$$

For the 150 kHz resonator E = 165 GPa, ρ = 2330 kg/m^3, L =300 μm, h = 1.6 μm, f_0 is calculated as 151.9 kHz. Other researchers took the value of E as 150 GPa [8], if this value is used here, the calculated f_0 is 144.9 kHz. Actually, it is reasonable we assume the following uncertainties for the parameters of the resonator beam: 5% of E, 3% of h and d_0, 1% of L and W. By doing so $f_0 = (150 \pm 10)$ kHz was calculated. Here the peak resonant frequencies given in figure 5.2 and figure 5.4 for two methods, being 147.516 kHz in capacitive couple measurement and 147.076 kHz in beam deflection measurement, respectively, fall within the above calculated regime despite the applied DC bias voltage of 10 V induced a decrease of the resonant frequencies. Experimentally the resonant

frequency under zero DC bias voltage can be obtained by extrapolating the data of resonant frequencies dependence on DC bias voltages. These will be discussed later.

Figure 5.5 gives the data measured with a DC bias voltage of 1 V and an AC driving signal of 20 mV using optical method. As a comparison, figure 5.6 shows the data measured with a DC bias voltage of 2 V and an AC driving signal of 20 mV using capacitive coupled method. The data by optical method clearly show a well-defined resonance peak occurred at the frequency of 151.310 kHz, accompanied by a phase change of 180 degree. This is the typical characteristic of mechanical resonance. But, the data by capacitive coupled method show a very small peak in amplitude accompanied by a very ambiguous phase shift. This clearly demonstrates the existence of large parasitic signals in the capacitive coupled detection, the motional current almost completely buried in the background signals.

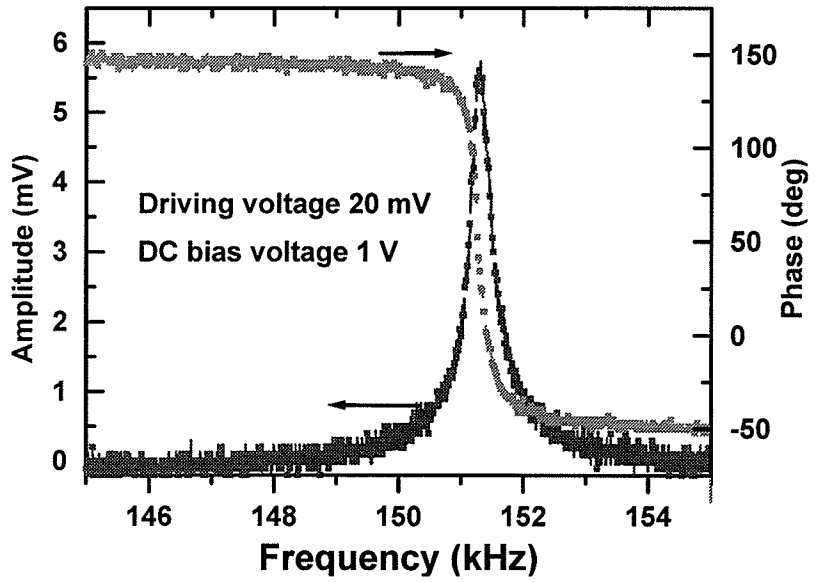

Figure 5.5 Measurement data under DC Bias voltage of 1 V and AC driving voltage of 20 mV using optical beam deflection method.

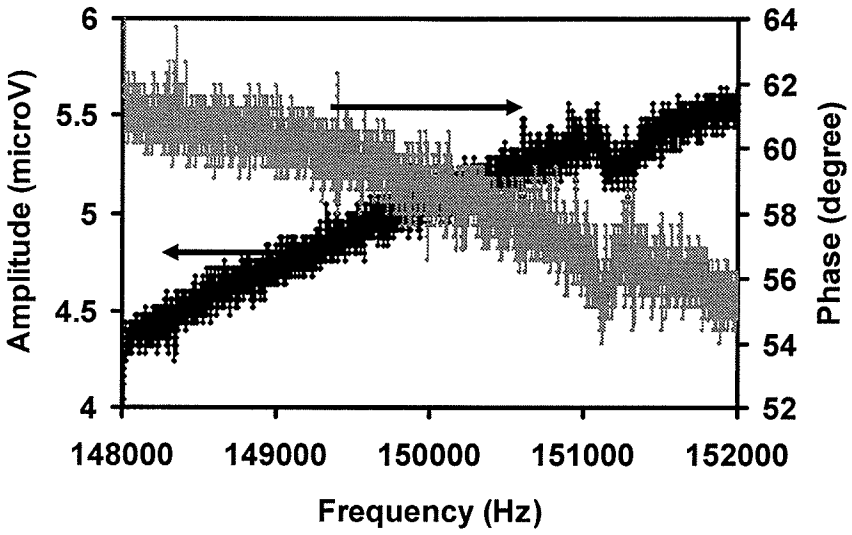

Figure 5.6 Measurement data under the DC Bias voltage of 2 V and AC driving voltage of 20 mV using capacitive coupled method.

5.1.2.2 Quality Factor Q

An important mechanical property, Quality factor Q, can be deduced from the frequency response of the amplitude. Q is defined as the ratio between the total energy stored in the vibration and the energy loss per cycle:

$Q = 2\pi$ (total energy stored in vibration)/(dissipated energy per period)

The quality factor Q is a measure for the energy losses in the resonator (or for the mechanical damping). A high Q implies low energy losses, which is always expected. When a resonator is excited by a harmonic force with constant amplitude, Q is commonly determined from the response characteristics of the resonator using -3db definition: $Q = f_r /(\Delta f_{-3dB})$, where f_r is the frequency with maximum frequency response and Δf_{-3dB} is the half power bandwidth of the frequency response. Hence, a sharp resonant peak will result in a high Q factor, which is preferred by the frequency selectivity of the resonator. Here, from the experimental data in figure 5.5 the value of Q is estimated as 700.

High Q is desired because of the low energy requirement for maintaining the vibration, low sensitivity to mechanical disturbances and minimal effect of the electronic circuitry on the oscillation frequency. Usually, the energy losses in the resonator are attributed to three contributions: losses into the surrounding medium, losses into the mechanical support of the resonator and intrinsic energy dissipation inside the material of the resonator. Thus, it is important to carefully distinguish the dominant source of energy losses in order to effectively improve the quality factor.

5.1.2.3 Motional and Feedthrough Currents

The following gives the estimation of feedthrough current and motional current based on theoretical formula. The motional current can be calculated using following equation deduced from equation (2.48)

$$i_m = (QU_{dc}^2 U_{ac} \omega_0 C_0^2)/(k_1 d^2) \qquad 5.2$$

When U_{dc} is 1 V and U_{ac} is 20 mV, d = 2 μm, ω_0 =2π x 150 kHz, K_1 is calculated as 23 N/m using equation (2.13), C_0 is calculated using the dimension of the resonator is 40 fF. The motional current i_m has a value of 0.26 nA using quality factor estimated by optical method. For U_{dc} =10 V and i_m = 26 nA, if Q is assumed as the same value.

On the other hand, the feedthrough current from C_0 can be calculated using the following equation

$$i_0 = C_0 \omega_0 U_{ac} \qquad 5.3$$

i_0 = 0.75 nA. i_0 is not affected by DC bias voltage based on equation (5.3).

When the DC bias voltage is 2 V, i_m is about 0.67 nA using Q of 437 estimated from the optical data under DC bias voltage of 2 V, which is very close to i_0. Thus, it is very

hard to resolve the motional current from the feed through current and other parasitic currents. This rough estimation agrees well with what the experimental data revealed in figure 5.6.

The experimental data acquired using optical beam deflection method can be used to estimate vibration amplitude experienced by the resonant beam, the amplitude in voltage can be converted into the amplitude in nanometer by taking an approximate conversion coefficient of 0.4 mV/nm [43], then, peak-peak value of vibrating amplitude of about 15 nm is yielded for the data in figure 5. under the DC bias voltage of 1 V and the AC driving voltage of 20 mV. Theoretical resonance amplitude can be calculated based on the following equation:

$$u_{res} = \frac{F_e}{k_1} Q = \frac{C_0}{d_0} \frac{Q}{k_1} U_{dc} U_{ac} \qquad 5.4$$

u_{res} is about 14 nm using Q of 700. This value agrees well with that obtained from the experimental data. For the experimental data taken under the DC bias voltage of 2 V and the AC driving voltage of 20 mV the estimated vibration amplitude is about 23 nm while the calculated value from formula (5.4) is about 18 nm using Q of 437 extracted from the experimental data by optical beam deflection method. They are still in a good agreement. That the calculated value is a little bit smaller than the measured one might be speculated to be caused by the occurrence of nonlinearity when DC bias voltage reached 2 V. Q factor is now hard to be accurately evaluated from the experimental data.

5.1.2.4 Dependence of Resonance Frequency on DC Bias Voltage

In order to investigate dependence of resonant frequency and quality factor on DC bias voltage, measurements were done by varying DC bias voltage from 1 V to 10 V. The

experimental data of dependence of the peak frequency on the DC bias voltage for both capacitive coupled technique and optical beam deflection method were summarized in Table 5.1. The values of peak frequencies were directly read from the measurement data.

Table 5.1 Experimental data of peak frequency versus DC bias voltage when V_{ac}=20 V

DC bias voltage (V)	2	4	6	8	10
Peak frequency (kHz) (Capacitive coupled method)	151.086	150.461	149.721	148.713	147.517
Peak frequency (kHz) (Optical deflection method)	151.078	150.463	149.526	148.411	147.076
f/f_0 (Theoretical data) f_0 =(150 ± 10) kHz	0.9991 (0.0002)	0.9966 (0.0010)	0.9922 (0.0022)	0.9861 (0.0038)	0.9783 (0.0060)
f/f_0 (Experimental optical data) f_0 =(151.2 ± 0.1) kHz	0.9989 (0.0000)	0.9955 (0.0002)	0.9899 (0.0004)	0.9819 (0.0007)	0.9716 (0.0010)

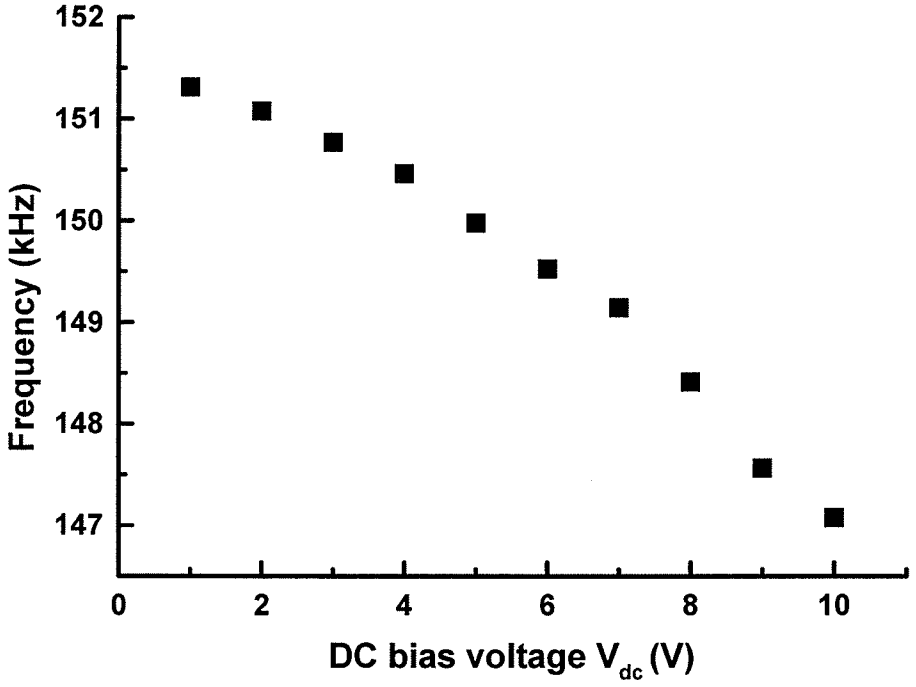

Figure 5.7 Peak frequency versus DC bias voltage using optical beam deflection method

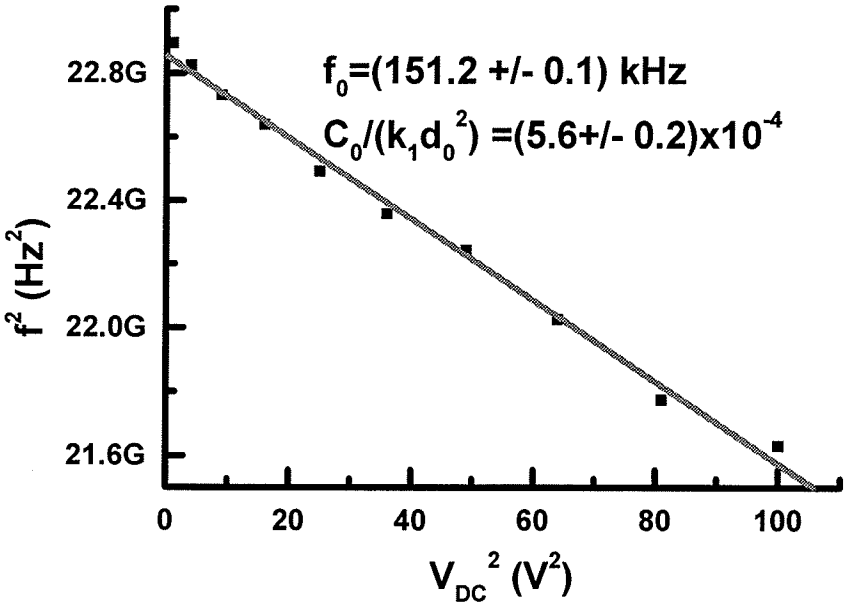

Figure 5.8 Data were fitted for dependence of DC bias voltage on peak frequency

Figure 5.7 plotted the data of peak frequency versus DC bias voltage acquired by optical beam deflection method. It is clearly seen that the peak frequency decreases with increase in DC bias voltage. This agrees well with the theoretical expectation based on the equation (2.45), which is rewritten in the following form

$$f_r = f_0\sqrt{1-\frac{C_0 U_{DC}^2}{k_1 d^2}} \qquad 5.5$$

The experimental data were fitted based on the above equation, and the fitted data can be utilized to examine how well theoretical calculation and experimental data agree. As shown in figure 5.8, the fitted value of $C_0/k_1d_0^2$ is $(5.6\pm 0.2) \times 10^{-4}$ and f_0 is (151.2 ± 0.1) kHz using the experimental data. Theoretical calculation of $C_0/k_1d_0^2$ is $(4.3\pm 1.2) \times 10^{-4}$. They agree pretty well even if the peak resonant frequencies, rather than real resonant frequencies due to the nonlinear behavior, were applied.

Figure 5.9 plotted the normalized resonant frequency against the DC bias voltage for both theoretically calculated data and experimental data by optical beam deflection. They are in very good agreement at low DC bias voltages. The deviation at higher DC voltages (over 3 V) might be caused by 'spring softening' nonlinear behavior, which usually makes the resonant peak bend towards lower frequency. Equation (5.3) is only valid for linear behavior of beam vibration.

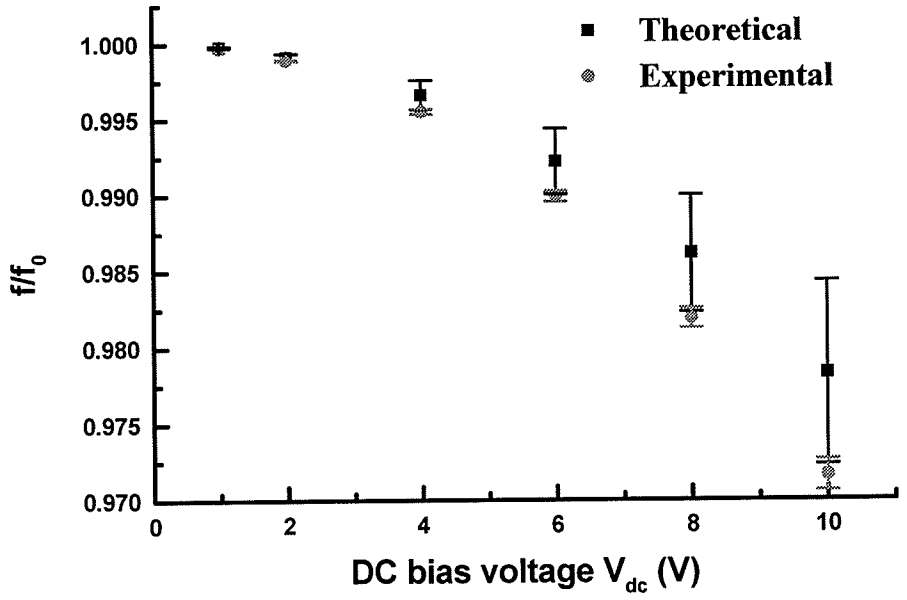

Figure 5.9 Normalized resonant frequency versus DC bias voltage for theoretical and experimental data.

Table 5.2 summarizes the estimated major mechanical properties and electromechanical parameters for the 150 kHz micromachined resonator. The important parameters such as resonant frequency and spring constant coefficient were obtained both theoretically and experimentally. Based on the experimental data, the equivalent electrical components of this electromechanical system were deduced in terms of the description in the section 2.11 of the chapter 2. The equation (2.54) can be rewritten in the following forms:

$$L_m = \frac{k - k_e}{\omega_0^2 \eta^2} \qquad R_m = \frac{k - k_e}{\omega_0 Q \eta^2} \qquad C_m = \frac{\eta^2}{(k - k_e)}$$

where $\eta \approx U_{DC} \frac{C_0}{d_0}$, and $k_e = U_{dc}^2 \frac{C_0}{d_0^2}$.

The values of k, ω_0 and Q are taken from the experimental data with the DC bias voltage of 1 V. k_e is 0.01 N/m for U_{dc} of 1 V. Experimentally the uncertainty of k was estimated to be of 12% per cent, and the uncertainty of ω_0 of 0.04% is negligible. The uncertainties of k and η of 8% were only considered to estimate the uncertainties of R_m, C_m and L_m. The equivalent electrical circuit can be constructed using these equivalent electrical parameters for further analysis in terms of circuit theory and simulation tools.

Table 5.2 Theoretical and experimental data for the 150 kHz resonator

Mechanical parameters		**Electromechanical parameters**	
Length of beam, L_r (μm)	300	Static capacitance, C_0 (fF)	40 ± 2
Width of beam, W_r (μm)	30	Quality factor, Q (V_{dc}=1V)	700
Thickness of beam, h_r (μm)	1.6	EM coupling, η (V_{dc}=1V) x10^{-8}	2 ± 0.2
Beam-substrate spacing, d_0 (μm)	2.0	Equivalent resistance, R_m (MΩ)	70 ± 20
Young's Modulus, E (GPa)	157 ± 8	Equivalent inductance, L_m (kH)	50 ± 10
Density of polysilicon, ρ (kg/m^3)	2330	Equivalent capacitance, C_m (aF)	22 ± 2
Beam mass, m (kg x10^{-12})	32.9	Pulling Voltage, V_{pull} (V)	23 ± 3
Spring constant, K_1 (N/m)	23 ± 4	Measured K_1 (N/m)	18 ± 1
Resonant frequency, f_r (kHz)	150 ± 10	Measured f_r (kHz)	151.2 ± 0.1

5.1.2.5 Nonlinear Behavior

In Figure 5.10 nonlinear vibration is evidenced by the rapid jump in amplitude when the resonant frequency is approached, reflecting the nonlinearity of spring restoring force. The curve at peak frequency bent towards lower frequency, which is caused by the so-called 'spring softening' induced by the DC bias voltage. Experimental data show that the nonlinear behavior occurred when the DC bias voltage reached over approximate 2 V. The rapid jump of amplitude indicates that vibration quickly changes from an unstable state to another stable state when sweeping frequency passes through the resonance regime. Because the real resonance frequency is hard to be defined due to the occurrence of nonlinearity, the peak frequencies are used to be approximate resonant frequencies. In addition, the peak amplitude increases with the DC bias voltage. But the value of vibration amplitude is not proportional to the DC bias voltage as equation (2.43) expected because nonlinearity limited the resonant peak value.

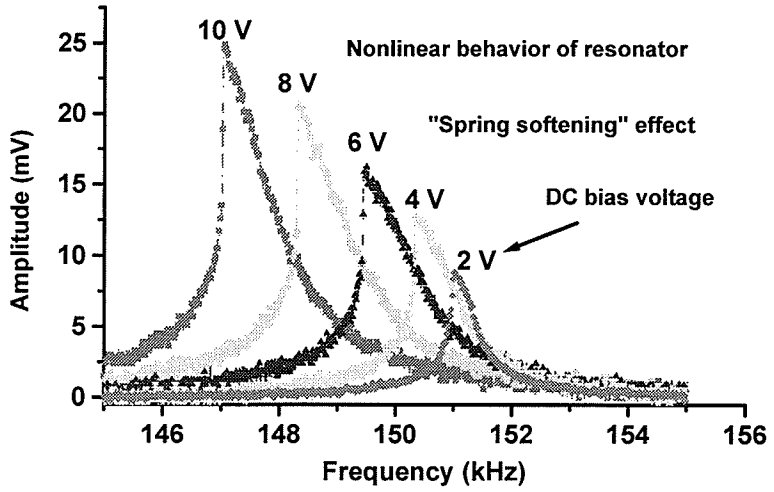

Figure 5.10 Lock-in outputs versus sweep frequency under various DC bias voltages

Most existing models proposed for the explanation of nonlinearity are based on specific experimental observations [44-49]. For instance, the observed 'spring hardening' behavior is attributed to the mechanical restoring force with a positive cubic form, which tends to shift natural frequency to higher value; whereas, the 'spring softening' behavior is associated with electrostatic force, which tends to shift natural frequency to lower value. In actual devices, however, mechanical and electrical nonlinearity usually simultaneously contribute to the nonlinear behavior. In addition, the microbeam is a distributed mass system rather than a single-degree-of-freedom system as assumed in many models. The electric force is dependent on the variable gap between the resonant beam and the electrode; the natural frequencies of a straight beam and a DC biased beam are different. Thus, it is often hard to analytically predict what type of nonlinearity will occur. Experimentally, some devices exhibited softening behavior, whereas others exhibited hardening behavior [44]. In many experiments the 'spring hardening' behavior was observed by increasing AC driving voltage [48-52]. The experimental data in reference [49] are in good agreement with their simulation results, the simulation data was derived using the method of harmonic balance by assuming the mid-plane stretching being an only contribution to the nonlinearity without the electrostatic force; on the other hand, the simulation results show a softening-type behavior by solely considering the electrostatic force and neglecting the mid-plane stretching. Our experimental data, as far as we know, first experimentally demonstrated the softening-type behavior as shown in the figure 5.10. That quantitatively how well our experimental data can be fitted into their model is suggested for future work.

A comprehensive description of the distributed-parameter system for a microbeam was introduced by accounting for mid-plane stretching, an applied axial load, and the microbeam response to both DC and AC components [53]. The study shows that either the increase or the decrease in the nonlinear resonance frequency depends on the sign of the effective nonlinearity coefficient which is associated with the mid-plane stretching, the DC bias voltage and the AC driving voltage, and the damping and the axial force. The increasing in the axial force tends to improve the linear characteristics and decrease the frequency shift. In contrast, the increasing in the mid-plane stretching will increase the nonlinear resonance frequency. On the other hand, the DC bias voltage affects the effective nonlinearity coefficient of the system, if the sign of the effective nonlinearity coefficient changes from positive to negative, the vibration system changes its behavior from a 'spring hardening' type to a "spring softening' type, this is attributed to the electrical nonlinearity, which drastically increases in magnitude and overcomes the influence of the geometrical nonlinearity. Most likely this is the case occurred for our 150 kHz resonator, the applied DC bias voltage dominates the nonlinearity of the microbeam rather than the mechanical stretching does. But, further quantitative calculation based on the design parameters and the measured properties is necessary for correct evaluation of the practical device.

5.1.2.6 Nonlinear Criterion

Theoretically critical condition for linear and nonlinear operation of the forced vibration can be computed, the maximum vibration amplitude for the linear motion is given by the following formula [45]

$$u_c = \frac{h}{\sqrt{0.53Q(1-\nu^2)}} \qquad 5.6$$

Where h is the thickness of the microbeam, Q is the quality factor, ν is the Poisson's ration (for polysilicon ν is about 0.2). When the vibration reaches nonlinear regime, the amplitude has triple values for certain frequency, showing unstable state. Thus, resonant amplitude u_{res} must be smaller than the critical amplitude in order for linear operation. Critical amplitude calculated based on the equation (5.6) is estimated as 83 nm using the estimated Q factor of 700.

Combining the equation 5.4 and 5.6 yields the driving voltage condition for linear operation:

$$U_{dc}U_{ac} < \frac{1.4}{Q^{3/2}} \frac{k_1 h d_0^2}{\varepsilon A} \qquad 5.7$$

Equation (5.7) shows the limitation for the linear operation by the structure parameters of device and its quality factor; and for a microstructure, driving signal and DC bias voltage should be carefully chosen to ensure linear operation.

The theoretical calculation based on equation (5.7) predicts the critical value of DC bias voltage for the occurrence of nonlinearity much larger than the experimental data for the AC driving voltage of 20 mV. The theoretical computation gives a critical value of DC bias voltage of about (6 ± 1) V using estimated Q value of 700 under the DC bias voltage of 1 V, it is as 3 times large as the experimental value of 2 V. But, this result is not unreasonable, given the large uncertainties in many of the parameters. Figure 5.11 plots a critical curve for the linear operation based on the equation (5.7).

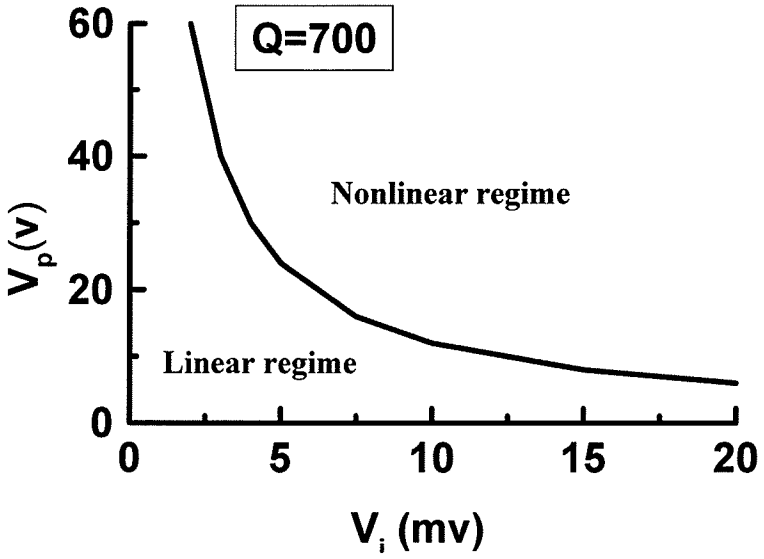

Figure 5.11 The criterion curve for the linear operation of the microbe

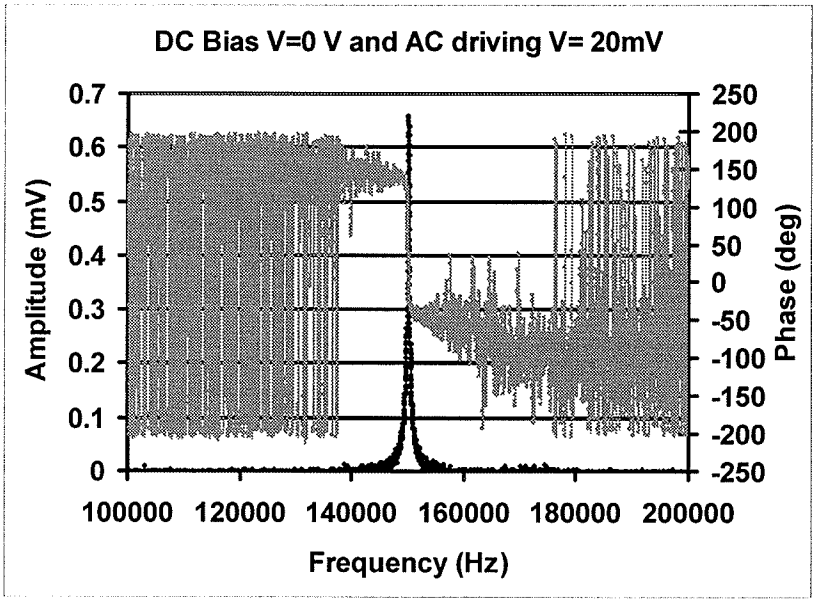

Figure 5.12 Lock-in output versus frequency by optical beam deflection.

Figure 5.12 shows the experimental data collected under zero DC bias voltage and AC driving voltage of 20 mV in the turbo pumped vacuum. The data presents a very

pronounced peak around 150 kHz, its resonant vibration amplitude was estimated about 1.5 nm. The measurement clearly demonstrates that the optical method offers much higher resolution than the electrical measurement. Therefore, the optical testing techniques for the characterization of the MEMS device are a good choice.

5.1.3 Experimental Data by Optical Fiber Interferometer

5.1.3.1 Resonant Frequency

The 150 kHz resonator was also examined using optical fiber interferometer as described in the figure 4.9 of the chapter 4. Figure 5.13 illustrated the spatial relationship between the tapered fiber and the resonator beam. It can be seen that it is hard to position the core fiber right above the resonator with a narrow width.

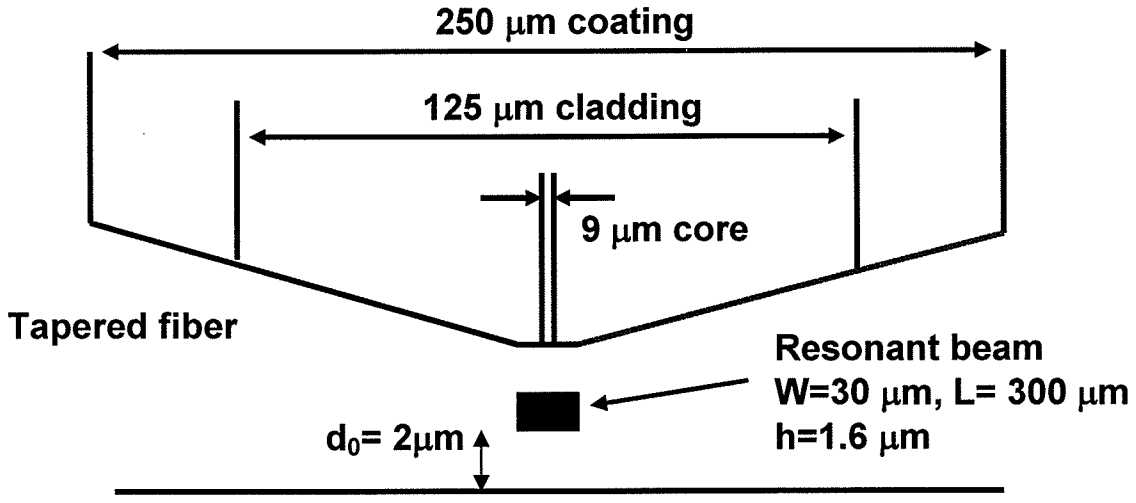

Figure 5.13 Schematic diagram of the tapered fiber and its position relative to the mechanical resonator beam.

Figure 5.14 shows the measurement data obtained with an AC driving signal of 20 mV and a DC bias voltage of 1 V under turbo pump vacuum. Peak resonant frequency is 151.380 kHz around which phase shifts about 180 degree. Q factor of 540 was found by -3dB definition. The data obtained here show the same behaviors as those measured using optical beam deflection discussed previously.

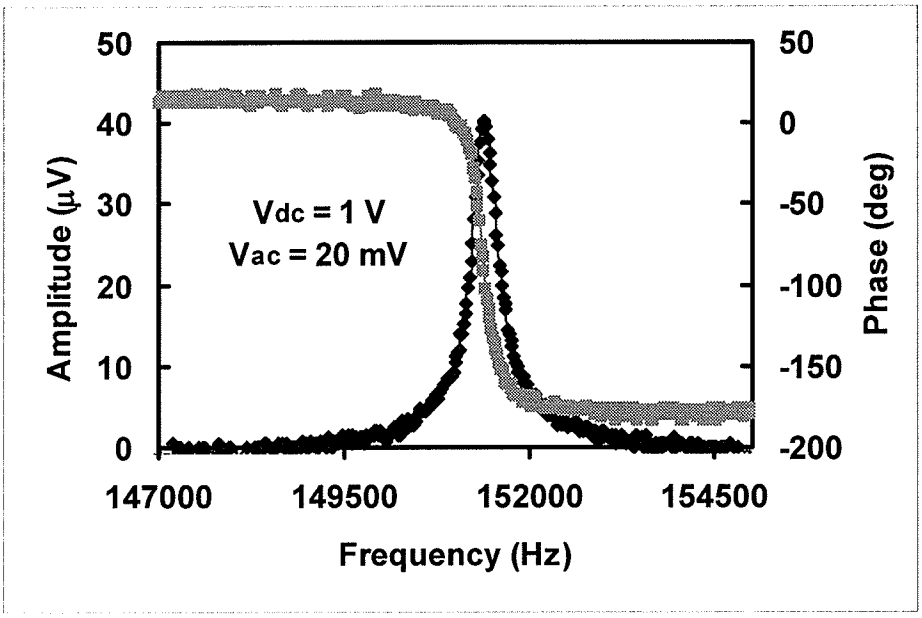

Figure 5.14 The resonator vibration measured using optical fiber interferometer

5.1.3.2 Effect of DC bias voltage

The effect of DC bias voltage on the vibration of the resonator was also investigated using optical fiber interferometer. The experimental data are shown in the figure 5.15, from which the peak frequencies under different DC bias voltages were obtained and listed in the Table 5.3.

Table 5.3 Peak frequencies measured when V_{ac} = 20 mV

V_{dc} (V)	0	0.2	0.5	1	2	3	4
f (KHz)	151.400	151.440	151.420	151.380	151.300	151.180	151.060
V_{dc} (V)	5	6	7	8	9	10 (up)*	10 (down)**
f (KHz)	150.880	150.720	150.480	150.360	150.140	149.860	149.700

(Up)* frequency sweep up; (down)** frequency sweep down

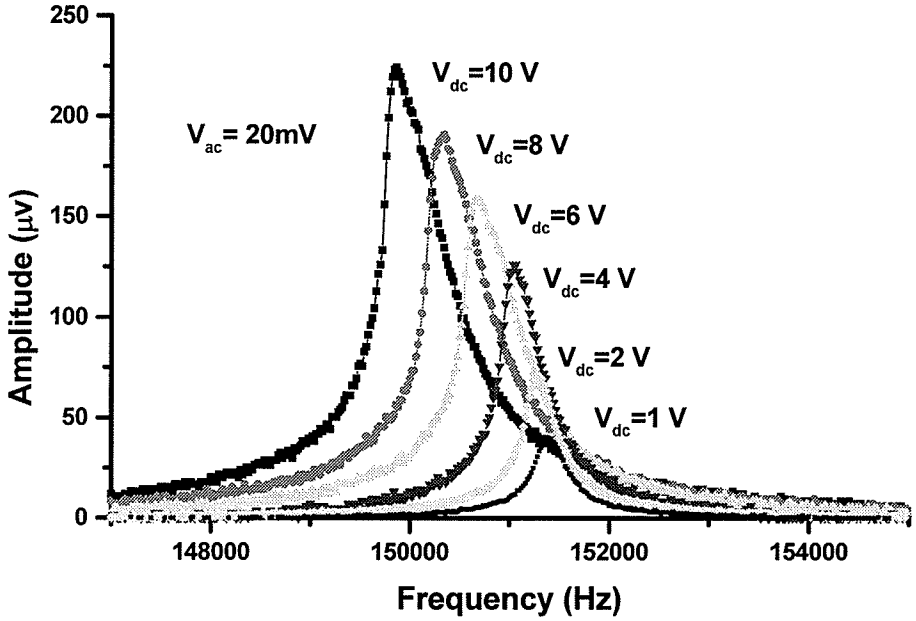

Figure 5.15 Effect of DC bias voltage measured by optical fiber interferometer

As same behavior as in the measurement by optical beam deflection method, the resonant frequency decreases with increase in the DC bias voltage, and the nonlinear vibration behavior of the resonator occurs at high DC bias voltages. The difference is that here the changes in resonant frequency under high DC bias voltages are less than those measured by optical beam deflection. The reason for this is unclear. It is speculated that

the mechanical properties of the beam probably changed after high AC driving voltage was applied during the measurement using optical beam deflection. Based on the same data analysis as that used for the beam deflection method, the resonant frequency of 151.4 kHz and spring constant k_l of 47.7 N/m were deduced by fitting the experimental data. It is obvious that k_l obtained using fiber optical interferometer is roughly two times larger than that using optical beam deflection method. It seems that the resonant beam became stiffer, but, resonant frequency did not increase much corresponding to the increase of the spring constant. Quantitatively the value of k_l seems not reasonable when compared with the theoretical expectation and the measurement result by optical beam deflection method.

5.1.3.3 Effect of AC exciting voltage

In figure 5.16 the effect of AC driving voltage on the vibration was investigated by fixing DC bias voltage at 2 V. The peak frequencies under different AC driving voltages were listed in the Table 5.4. It is evidenced that the vibration behavior is very close to be linear under the AC voltage of 20 mV and DC bias voltage of 2 V and tends to display nonlinearity under high AC driving voltages, especially under the AC voltage of 100mV. The nonlinearity belongs to the type of 'spring-softening' as discussed previously. This is contrary to the other experimental results [50-52] where the nonlinearity of 'spring hardening' was observed when the AC driving voltage increased. These experimental results reveal the complexity of the mechanisms affecting practical devices; they are difficult to predict unless the controlling of all relevant parameters is available.

Table 5.4 Peak frequencies measured when V_{dc} = 2 V

V_{ac} (mV)	20	40	60	80	100
f (kHz)	151.300	151.180	151.140	151.060	150.980

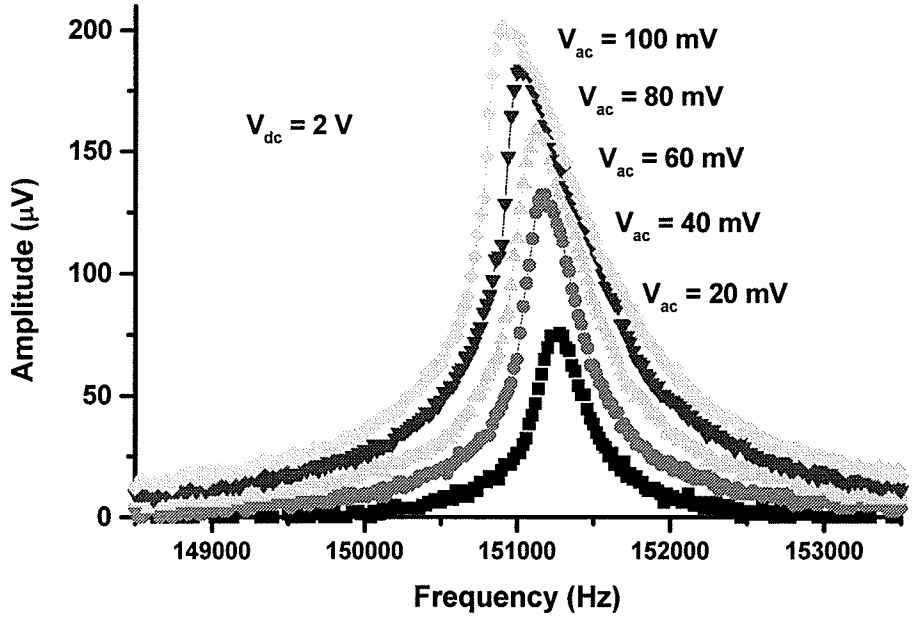

Figure 5.16 Effect of AC driving voltage on the vibration by optical fiber interferometer

5.1.3.4 Hysteresis in the Mechanical Response

The nonlinear frequency response of the vibrating amplitude predicts the possibility of hysteresis as stated in chapter 2. Experimentally, this hysteresis was investigated by sweeping frequency up and down, respectively. The data shown in figure 5.17 indicate that the mechanical system really displays the hysterisis behavior. The peak amplitude in frequency sweeping-down is a little bit higher than that in frequency sweeping-up, and the peak frequency of 149.700 kHz in the frequency sweeping-down is lower than that of

149.860 kHz in the frequency sweeping-up. Difference of the two frequencies is significant for real time applications.

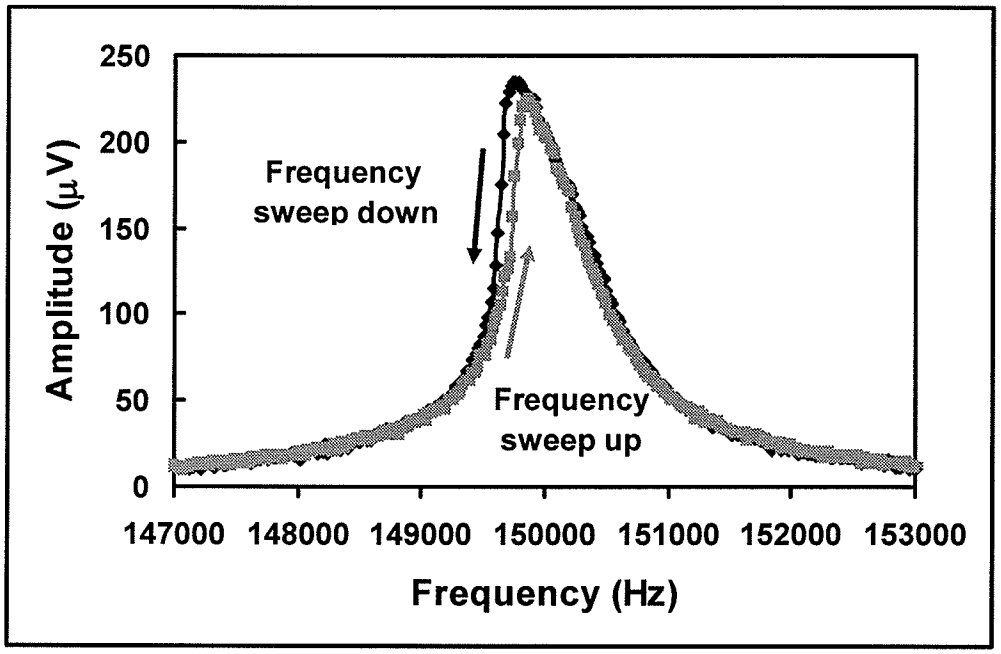

Figure 5.17 Hysteresis behavior measured under a DC Bias voltage of 10 V and an AC voltage of 20 mV by sweeping frequency up and down, respectively.

5.1.3.5 Effect of Viscous Damping

Another factor affecting the resonator is the viscous damping of the surrounding gas. The effect of pressure on the vibration of the resonator was roughly investigated in our experiment, and experimental data are shown in figure 5.18. It is obviously seen that the increasing of pressure in the vacuum chamber significantly reduced the vibration amplitude and quality factor Q. The quality factor and the peak frequency of vibration under different pressure environments are tabulated in Table 5.5. When the vacuum chamber was under the pressure of atmosphere, the signals of amplitude and phase of the

vibration were almost completely buried in noise background. This indicates that the measurement of the resonator has to be carried out under certain vacuum environment.

Table 5.5 Effect of pressure on the vibration of the resonator (V_{dc} = 2V, V_{ac} = 20mV)

	$P<10^{-3}$ torr	9 hours after stopping pump	60 hours after stopping pump	After releasing some air in
Q	378	90.8	12.1	3.7
f_{peak} (kHz)	151.2	150.7	150.5	149.2

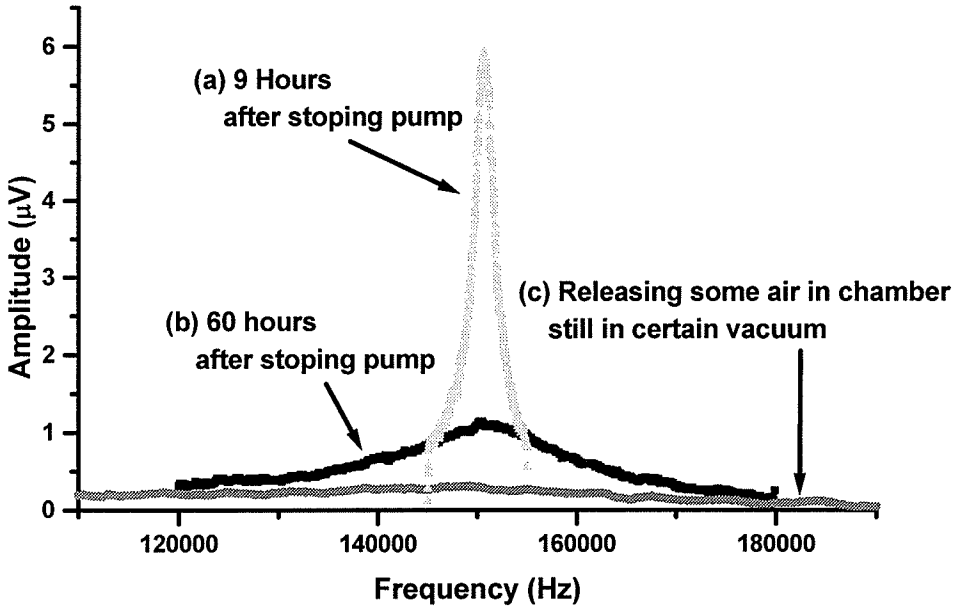

Figure 5.18 Effect of vacuum pressure on the vibration of the resonator under DC bias voltage of 2 V and an AC driving voltage of 20 mV.

The interaction between the resonator and the surround gas molecules was investigated in terms of the pressure and relative geometrical dimension of the resonator where three situations were discussed [1]: One is for pressure much below 1 atm under which the

mean free path of gas molecules is sufficiently long so that they do not interact with each other significantly. The momentum exchange of the gas molecules with the resonator structure is proportional to the difference in velocity between them, leading to the damping proportional to gas pressure. Second is for the micromachined resonators with widths greater than 0.4 μm, gases can be treated as a viscous fluid where molecules interact with each other and Stoke's Law can be employed to compute Q by taking into account the damping force. Third is for the resonant beam with the spacing to the substrate less than approximately one-third of the width of beam, the squeeze damping effects take effect, where the flow velocities are subsonic. The relationship between Q and pressure can be evaluated theoretically under the above three conditions.

The viscous damping will severely affect the performance of the micromachined resonator, especially, when the size of resonators becomes smaller and smaller, such as for the so-called Nano-mechanical devices (NEM). Thus, complete study on the effect of pressure on the resonators is very necessary for the practical applications of the micromachined resonator, especially for the vacuum package.

5.1.3.6 Conversion of Lock-in Output to Nanometer

In order to estimate the vibration amplitude of the resonator, output of lock in amplifier in voltage needs to be converted to actual vibration amplitude. Based on the interfering intensity equation (3.38), intensity changes with distance between the end face of fiber and the surface of the vibrating resonator in a sinusoidal form, assuming the light reflected back into the fiber keeps constant when the spacing d changes, the interfering intensity I/I_0 changes with the distance d as illustrated in figure 5.19.

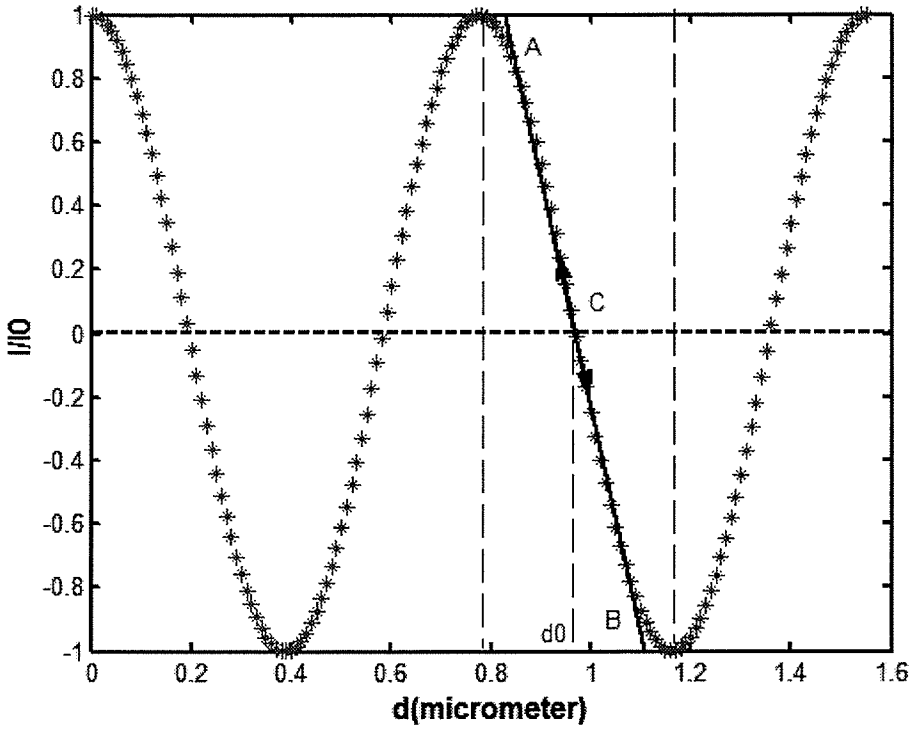

Figure 5.19 Interfering intensity versus spacing d between the fiber end and the Resonator.

For a small signal, the signal modulation is best to be positioned on the point of C where the slope is maximum so as to get best sensitivity of measurement. To locate the position C, the spacing d is adjusted to the position where the maximum signal is obtained. Also, wavelength of light can be tuned so that the maximum signal can be obtained. In order to determine the maximum slope, the intensity of signal should be measured against the change of known spacing d. Because the C point is hard to set, one method can be approximately used to estimate the slope as indicated in figure 5.19, where points A and B can be approximated as two peak points. The peak-peak amplitude of the signal is divided by the one fourth of the wavelength, giving the maximum slope of voltage signal against the vibration amplitude in nanometer, i.e., conversion coefficient. In our

experiment, wavelength of laser was tuned to the 1571(0.3) nm for the set-up of maximum slope; the maximum peak-peak signal of about 206 mV was measured for the vibration of the sample stage with low frequency. The conversion coefficient of 0.525mV/nm was roughly derived. For the measurement data obtained under the DC bias voltage of 2 V and AC driving voltage of 20 mV, the lock-in output is 70 μV in RMS, the peak-peak value V is 198μV. It is also needed to account for the limited frequency response of the photodetector and lock-in amplifier. As far as lock-in amplifier is concerned, there exists the frequency cut-off by the bandwidth formed by input impedance and input capacitance of lock-in amplifier in our experiment. The lock-in input was the port of 1MΩ//30pF, if the capacitance contributed by coaxial cable is included, total of 100 PF was estimate; thus, -3 dB frequency bandwidth calculated for the 1MΩ//100pF is 1.59 kHz. For the input impedance of 10 kΩ//100pF, 159 kHz bandwidth was yielded. This tells us that the signal measured using the input port of 1MΩ//100pF for lock-in amplifier was actually decayed very much. The measurement was carried out under the input of 1MΩ//100pF and 10kΩ//100pF, respectively. The lock-in output gave the value of about 70 μV for both under the V_{dc} of 2 V and V_{ac} of 20 mV. By taking account of the difference of two input impedances (1 MΩ and 10 kΩ), the signal measured for the input of 10kΩ//100pF should be multiplied by 100 so as to get the value corresponding to that for the input of 1 MΩ//100pF because the signal was actually decayed due to the frequency cut-off during the measurement. By doing so, the vibration amplitude of 33.8 nm was obtained, which falls in a reasonable range.

5.2 Measurement of 11MHz Resonator

5.2.1 Measurement by Network Analyzer

The sample of 18C device with 5 beams (beam L=30.6 μm, W=9 μm) was measured using network analyzer. The power of RF signal from network analyzer is 0 dbm (0.2225V) and DC bias voltage of 25 V applied to the resonator. Measurements were performed under the mechanical pumped vacuum chamber. No attempt was made to match the resonator to the testing circuit. Figure 5.20 shows the results of the measurements, where the upper part is transmission parameter S21. The data indicate that the power transmitted through the resonator peaks at around 10.9 MHz with peak value of -45.6 db. Corresponding to the amplitude peak, phase shift of about 8 degree is observed in the lower part of the figure. The width of peak is large and its peak height is very low, only about 0.5 db higher than the noise floor. Thus, it is hard to estimate Q value for this resonator. Both very small peak value and phase change at the resonance indicate that other parasitic signals rather than the desired signal induced by the resonant vibration of the resonator co-exist in the measuring circuit. These parasitic signals usually include the feedthrough capacitive signal of the resonator, bond pads capacitive signal and the cable capacitive signal. They are frequency-dependent, leading to the upward ramp. The experimental data show that the peak of S21 was becoming too small to be seen when the DC bias voltage decreased down to around 15 V, indicating that the motion current was buried in the parasitic signals. The peak value versus frequency listed in the table 5.6 qualitatively demonstrates the dependence of the resonance frequency on the DC bias voltage. Viscous damping can reduce the Q value, following the measurement under mechanical-pumped vacuum (usually less than 10^{-2} Torr), the

vacuum chamber was pumped using turbo-molecular pump, but, no significant difference of the measurement results under two vacuum pressures was observed, indicating that vacuum higher than mechanical-pumped system seems not improve the resonant vibration much (at least in our experiment). The damping caused by air becomes negligible when the pressure is below that of the mechanical pump. The peak frequency obtained in the measurement is very close to the data provided by Gennum Corporation.

Table 5.6 Dependence of peak frequency on DC bias voltage for P = -10dbm

V_{dc} (V)	15	18	20	23	25	30
f (peak)	11.080	11.058	11.000	10.968	10.905	10.852

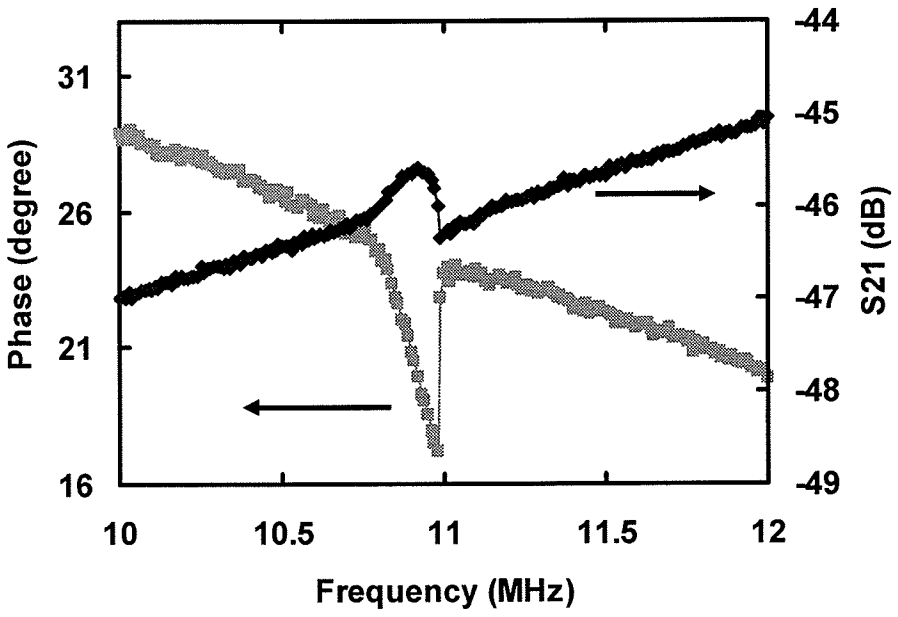

Figure 5.20 Transmission parameter S21 and phase measured by network analyzer with DC bias voltage of 25 V and RF power of 0 dBm in the vacuum for the sample 18C.

Another sample device of FL1 with 5 fingers (beam L=30.6 μ m, W=9 μ m) was measured via VNA with -10dbm and DC bias voltage 30 V under mechanical-pumped vacuum. The data is shown in figure 5.21. It is clearly seen that there exist three peaks at three different frequencies in the upper part of diagram and three correspondent phase shifts in the lower part. The results indicate that five identical fingers of the resonator did not response to the exciting signal at the same frequency. Considering the measurement data of 18C device with five fingers, it seems that it was hard to control fabrication process to build completely identical multiple-beams, which is initially expected for.

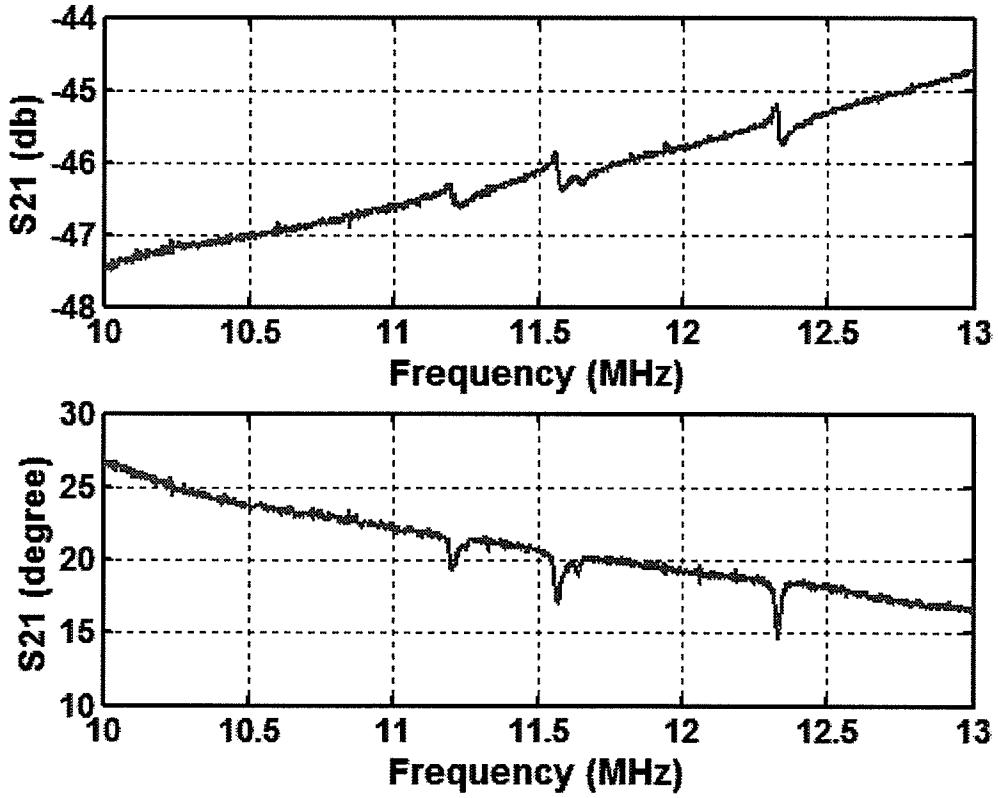

Figure 5.21 Transmission parameter S21 and phase measured by network analyzer for the sample FL1.

All of such samples were failed during the measurement. The sample 18 C was failed when exciting signal with high power was applied; others changed their resistivity from open circuit into around 200 Ω. The direct consequence was that no any resonant peaks could be observed again during the measurement. It is speculated that the devices are electrostatic sensitive and probably inappropriately handling caused the breakdown between electrode and substrate although much attention was already taken during the measurement.

Based on the equation (5.2) and (5.3), the ratio of the motional current i_m and the feedthrough current i_0 can be used to roughly evaluate the effect of parasitic signal. Here it is not intended because of unknown Q factor. The effect of parasitic signals on the measurement was also observed in many experiments performed by other investigators. In reference [34, 54], measurements were done for piezoelectrically/capacitively driven resonator beam force sensors. Their experimental data also showed a pronounced background signals occurring in the gain data, where a small resonant peak accompanied by a small phase shift at the resonance rather than 180 degree phase change as expected by resonance theory. The large background signals (crosstalk) were attributed to the substrate currents which were coupled to the detection fields. In order to eliminate the crosstalks, other two drive-detect schemes were successfully used to suppress the crosstalk [34]. In reference [50], in order to separate the feedthrough current from the motional current for a low Q comb-drive microresonator, an electromechanical amplitude modulation (EAM) measurement system was developed to remove the parasitic signal in frequency domain. In reference [42], mixing technique was used to separate the motional current from extraneous parasitic currents.

5.2.2 Measurement of 11 MHz Resonator by Optical Fiber Interferometer

5.2.2.1 Measurement by Network Analyzer

Before measurement on the resonator (labeled as 19D 9comb with 14 beam fingers, beam L= 31.6 μm, W = 3 μm) was done using optical fiber interferometer, network analyzer was first used to examine the frequency response of the S-parameters. Figure 5.22 gives experimental data for the sample measured under the DC bias voltage of 10 V and AC signal of -10 dbm in the mechanically pumped vacuum using network analyzer, indicating one resonant peak around 11.0 MHz and another two very closed peaks around 11.805 MHz and 12.0 MHz accompanied by very small phase shifts of about a few degree.

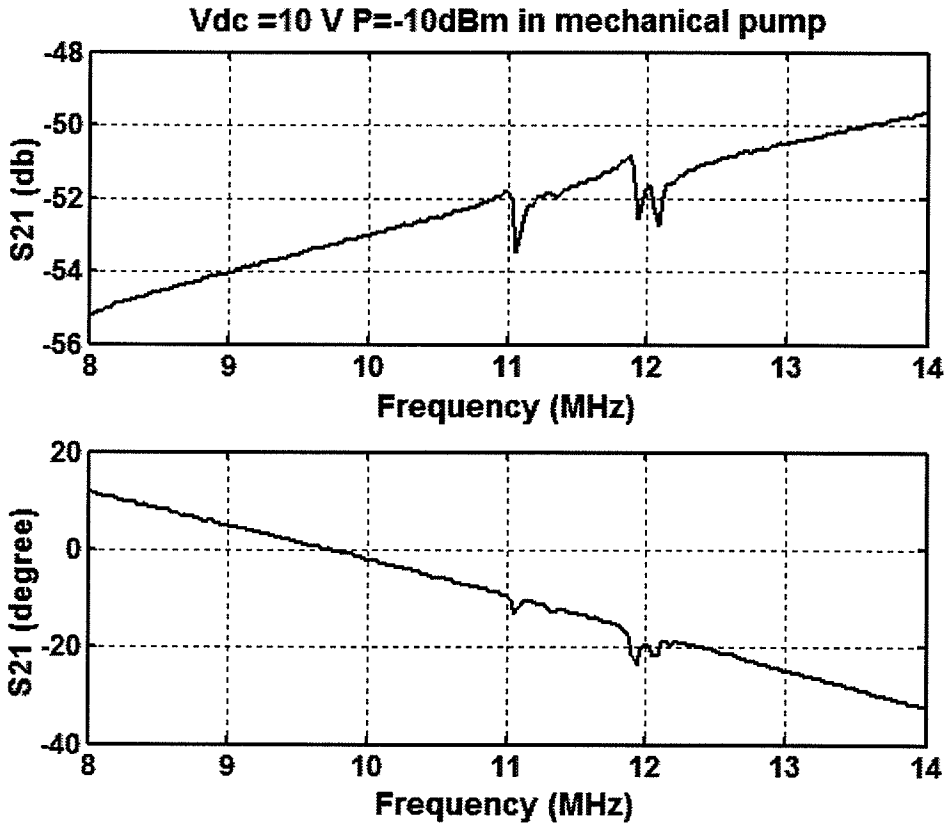

Figure 5.22 Experimental data measured using network analyzer.

The experimental data show the significant effect of parasitic signals on the measurement, which resulted in the degradation of signal/noise ratio. It is clear that the other better method for characterizing this electromechanical system is needed.

5.2.2.2 Measurement by Optical Fiber Interferometer

Figure 5.23 shows the experimental data measured under the DC bias voltage of 10 V and AC signal of 70 mV in the turbo pumped vacuum using optical fiber interferometer. A major amplitude peak at a frequency of 11.805 MHz is accompanied by a large phase shift of about 120 degree. The amplitude jump at 11.805 MHz clearly demonstrates nonlinear behavior of vibration with the type of "spring softening" which was introduced mainly by the electrostatic force applied to the resonator beam.

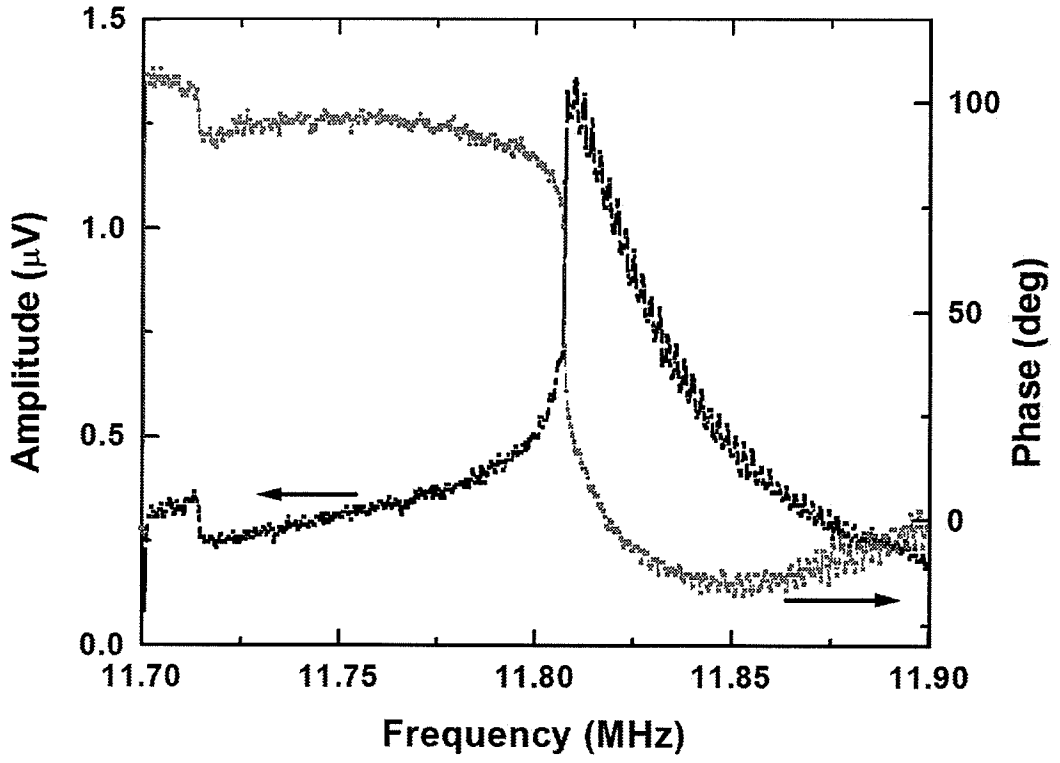

Figure 5.23 Amplitude and phase shift versus sweeping frequency under a DC bias voltage of 10 V and an AC exciting voltage of 70 mV in turbo pumped vacuum chamber.

5.2.2.3 Effect of DC Bias Voltage on Resonance

In figure 5.24 dependence of resonant frequency upon DC bias voltage was studied. It is clearly seen that the resonant frequency decreases with increase in DC bias voltage, peak frequency versus DC bias voltage is plotted in figure 5.25 and tabulated in Table 5.7. As described before for the 150 kHz resonator, the experimental data were fitted as shown in the figure 5.26, the resonant frequency at zero DC bias and spring constant k_1 were derived from the fitting results. Here the data of peak resonant frequencies were directly taken from the measurement, errors were not considered.

Table 5.7 Peak frequency measured when V_{ac} = 70 mV

V_{dc} (V)	2	3	4	5	6	7	8	9	10
f (MHz)	12.078	12.058	12.038	12.006	11.969	11.937	11.894	11.848	11.805

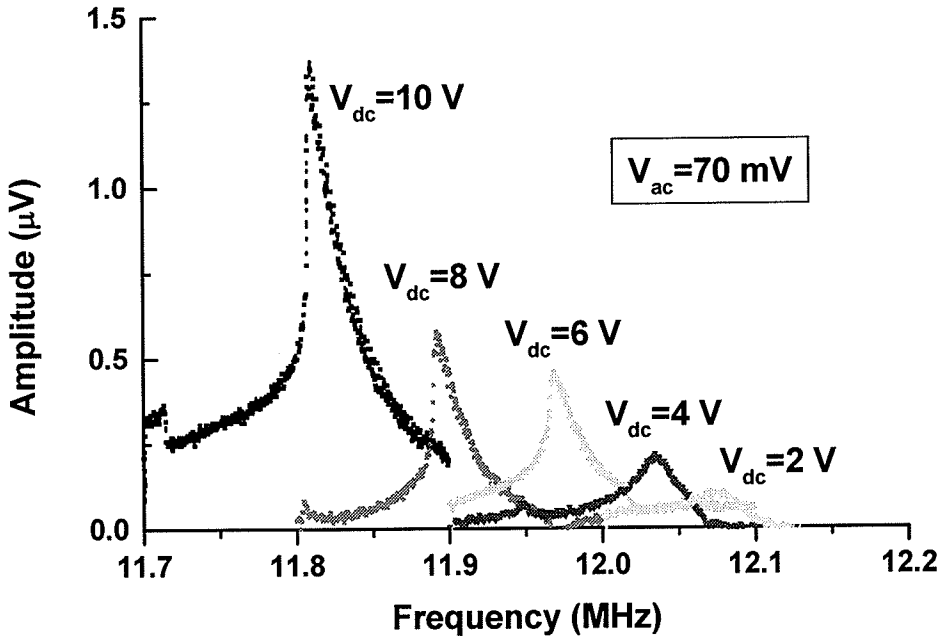

Figure 5.24 Dependence of resonant frequency and resonant amplitude upon DC bias Voltages at the same AC exciting voltage of 70 mV.

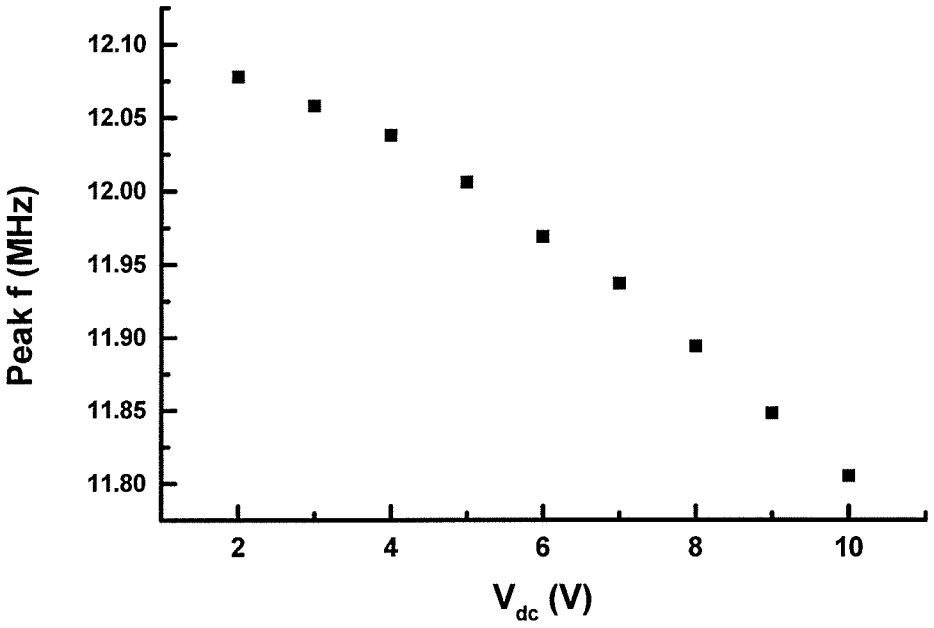

Figure 5.25 Dependence of peak frequency on DC bias voltage

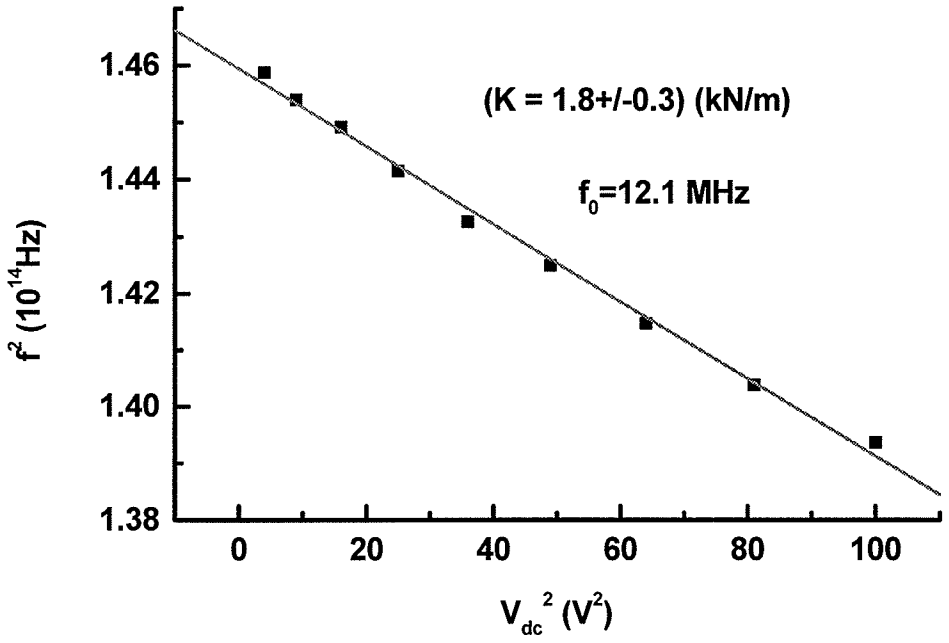

Figure 5.26 Experimental data were fitted and k was derived.

5.2.2.4 Effect of AC driving voltage on Resonance

The effect of AC exciting voltage on the resonant vibration behavior was investigated as shown in figure 5.27 where increase in AC voltage not only induced larger vibration amplitude but also significantly reduced the resonant frequency and enhanced the nonlinearity. This is because the applied AC driving signals were not very small compared to the DC bias voltages. As occurred in the 150 kHz resonator, increase in the AC driving voltage caused the occurrence of the 'spring softening' nonlinearity instead of "spring hardening'. The peak frequencies for different AC driving voltages are listed in Table 5.8.

Table 5.8 Peak frequencies versus AC voltages when V_{dc} = 10 V

V_{ac} (mV)	10	30	50	70	100	150
f (MHz)	11.862	11.840	11.819	11.811	11.797	11.783

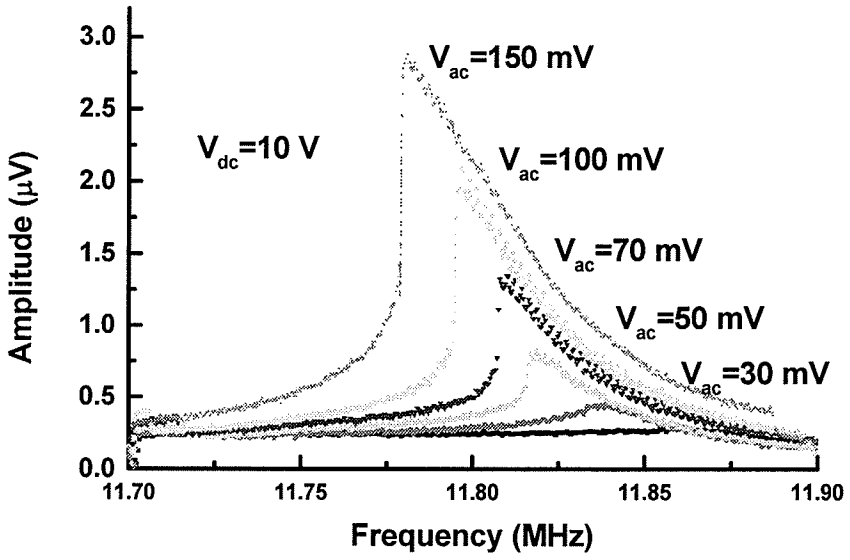

Figure 5.27 Dependence of resonance on AC driving voltages.

5.2.2.5 Mechanical and Electromechanical Parameters

Based on the experimental data, equivalent electrical parameters R_m, C_m and L_m for this resonator can be approximately derived in the same way as done for the 150 kHz resonator. The following formulas were written again to show how the electromechanical parameters were derived.

$$L_m = \frac{k - k_e}{\omega_0^2 \eta^2} \qquad R_m = \frac{k - k_e}{\omega_0 Q \eta^2} \qquad C_m = \frac{\eta^2}{(k - k_e)}$$

where $\eta \approx U_{DC} \frac{C_0}{d_0}$, and $k_e = U_{dc}^2 \frac{C_0}{d_0^2}$.

Q factor of 630 was taken from the experimental data with the DC bias voltage of 4 V and AC driving voltage of 70 mV. The values of k and ω_0 were obtained by fitting experimental data. η and k_e were calculated for U_{dc} of 4 V. k_e is 6.4 N/m. Most of the mechanical and electromechanical parameters for the resonator are listed in Table 5.9. The information about the dimension, young's modulus and density of the resonator beam was provided by Gennum Corp. The length of beam is not measurable by optical microscopy since the clamped area is not visible due to 40 nm topography/anchor. The length of 31.6 μm was used to calculate the resonant frequency, the expected value is 13.9 MHz for E of 165 GPa . Even if we use smaller Young's modulus E of 150 GPa, the resonant frequency is calculated to be 13.3 MHz. Here, we assume the following uncertainties for the parameters of the 11 MHz resonator beam: 5% of E, 3% of h and d_0, 5% of L and 1% of W. By doing so $f_0 = (14 \pm 2)$ MHz was calculated. Here, the measured resonant frequency is 12.1 MHz, which falls in the region of the expected resonant frequency. The spring constant k_1 of (1.8 ± 0.3) kN/m was obtained by fitting the experimental data. When young's modulus E of 157.5 GPa is used, the calculated k_1 is

(2.0 ± 0.6) kN/m, They agree very well within the uncertainty. The pull-in voltage V_{pl} of (25 ± 5) V was calculated based on the equation (2.46) by using experimental k of 1.8 kN/m. This value seems lower than that expected for the practical device. Probably the effective overlap area of the capacitor formed by the beam and the electrode should be considered because it may become significant when the beam becomes much smaller. Here equivalent electrical resistance R_m and equivalent inductance L_m are much smaller than that for the 150 kHz resonator beam, this is attributed to the very small beam-electrode spacing d, which greatly enhanced the electromechanical coupling. This is expected by the design of beam resonator.

Table 5.9 Theoretical and experimental data for the 11 MHz resonator

Mechanical parameters		**Electromechanical parameters**	
Length of beam, L_r (μm)	31.6 ± 1.6	Static capacitance, C_0 (fF)	8.4 ± 0.8
Width of beam, W_r (μm)	3.0 ± 0.03	Quality factor, Q (V_{dc}=4V)	630
Thickness of beam h_r (μm)	1.6 ± 0.05	EM coupling, η (V_{dc}=4V) x10^{-7}	3.4 ± 0.4
Beam-substrate spacing, d_0 (nm)	100 ± 3	Equivalent resistance, R_m (kΩ)	300 ± 100
Young's Modulus, E (GPa)	157 ± 8	Equivalent inductance, L_m (H)	3 ± 1
Density of polysilicon, ρ (kg/m^3)	2330	Equivalent capacitance, C_m (aF)	70 ± 30
Beam mass, m (kg x10^{-13})	3.33	Pulling Voltage, V_{pull} (V)	25 ± 5
Spring constant, K_1 (kN/m)	2.0 ± 0.6	Measured K_1 (kN/m)	1.8 ± 0.3
Resonant frequency, f_r (MHz)	14 ± 2	Measured f_r (MHz)	12.1 ± 0.0

Chapter 6 Conclusions and Further Work

6.1 Conclusions

With the rapid development of various micromachined devices using the MEMS technology, such as the micromechanical resonators, it is becoming more and more important to develop the testing tools for characterization of static and dynamic behavior of the MEMS devices in order to effectively evaluate their performances and to provide feedback to their design and fabrication processes. Besides conventional electrical measurements of the micromechanical devices using capacitive, piezoelectric and piezoresistive detection with network analyzer, spectrum analyzer and lock-in techniques, optical detection techniques, using laser beam deflection, heterodyne interferometer and homodyne interferometer, provide much better means by their high sensitivity of sub-nanometer resolution and much less susceptibility to parasitic signals. Through dynamic measurements of out-of-plane vibration, the mechanical and electromechanical properties can be obtained. These have been demonstrated through the measurements of the microresonators in this thesis work. Both electrical and optical measurements were carried out on the micromechanical resonators with the expected resonant frequency of near 150 kHz and 11 MHz, respectively.

For 150 kHz resonator, measurements were performed using capacitive coupled detection with lock-in technique as well as optical beam deflection and optical fiber interferometer methods. The experimental data show that this system behaved very much like a simple harmonic oscillator at low actuation levels and its resonance frequency very close to the expected theoretical calculation. Dependence of resonance frequency on DC bias voltage was investigated and the experimental data show a good agreement with

theoretical expectation. In addition, non-linearity of vibration of the micromechanical beam was observed and identified as a "spring softening" effect mainly induced by the large electrostatic force when higher actuation levels were applied. The experimental data demonstrate both optical methods display superior testing capability to the electrical measurements.

For the 11 MHz resonator, electrical and optical measurements were done using network analyzer by capacitive coupling method and optical fiber interferometer, respectively. Electrical measurement data show three resonant peaks, indicating the complicated electrical responses of the multi-beams structure of resonator. Its resonant frequency obtained experimentally is in a reasonable agreement with theoretical calculation. Dependence of resonance frequency on DC bias voltage agrees with theoretical prediction. A "spring softening" non-linearity of the beam vibration was also observed, which is similar to that occurred for the 150 kHz resonator.

The important features were evidenced by the experimental data are that the electrical measurements display very small resonant peaks accompanied by very small phase shifts and that the optical measurements show significantly large resonant peaks accompanied by large phase shifts about 180 degree which is a typical characteristic of mechanical resonant problem. The electrical measurements clearly indicate that the large parasitic signals exist in the capacitive coupled detection, which can greatly degrade the measurement. By contrast, the optical measurements are much less susceptible to the parasitic signals, especially to the feedthrough signal caused by the static capacitance of the resonator. Our experimental data undoubtedly demonstrate the advantages of the optical detection over the electrical detection.

Based on the experimental data, mechanical spring constant k and quality factor Q were derived; and the equivalent electrical parameters (resistance R_m, capacitance C_m and inductance L_m) for the electromechanical system were approximately derived in terms of equivalent electrical circuit theory. These parameters, on the one hand, can be applied to the evaluation and simulation of the mechanical and electrical properties of the device; on the other hand, are beneficial to the construction and simulation of practical electrical circuits, such as, filters and oscillators.

6.2 Construction of a Microresonator Oscillator

Micromechanical resonators have potential applications in the fields of sensors and electrical circuits of wireless communication. One possible application is to construct oscillators using these micromachined mechanical resonators so as to replace current quartz crystal oscillators in order for realizing system on a chip.

As described in the chapter 2, the microresonator can be modeled by the equivalent electrical circuit composed of purely passive circuit elements L_m, C_m and R_m, these electrical components consist of a series LRC circuit for describing the current-voltage characteristics of the resonating mechanical elements. These parameters can be found in the way as demonstrated by the 150 KHz and 11 MHz resonators. Besides the L_m, C_m, and R_m, parasitic elements in a practical electrical circuit should be appropriately modeled and included. The parasitic feedthrough capacitor C_0 is a major physical element affecting the performance of the electrical circuit. Other parasitic signals also should be carefully treated including interconnections, couplings from input and output ports to the ground and couplings between input and output port through the substrate.

A basic principle for construing an oscillator requires that a micromechanical resonator and an electronic amplifier are implemented in a positive feedback loop circuit. The resonator serves as a time element and the amplifier as a gain element. Two conditions need to be satisfied for the operation of the oscillator, one is that the loop gain must be designed to be larger than unity, second is the loop phase change should be 360^0 degree at the designed oscillating frequency.

A number of different oscillator topologies have been investigated and reported [55-60]. Among them two main types of oscillator topologies were employed, they are the transimpedance amplifier and the pierce oscillators. The general block diagram of the oscillator is shown in figure 6.1. The conditions for oscillation of loop circuit are represented by the following mathematical forms:

$$G(j\omega) = \frac{G_m Z_1 Z_2}{Z_1 + Z_2 + Z_r} \tag{6.1}$$

$$|G(j\omega)| \geq 1 \tag{6.2}$$

$$\angle G(j\omega) = 0^0 (360^0) \tag{6.3}$$

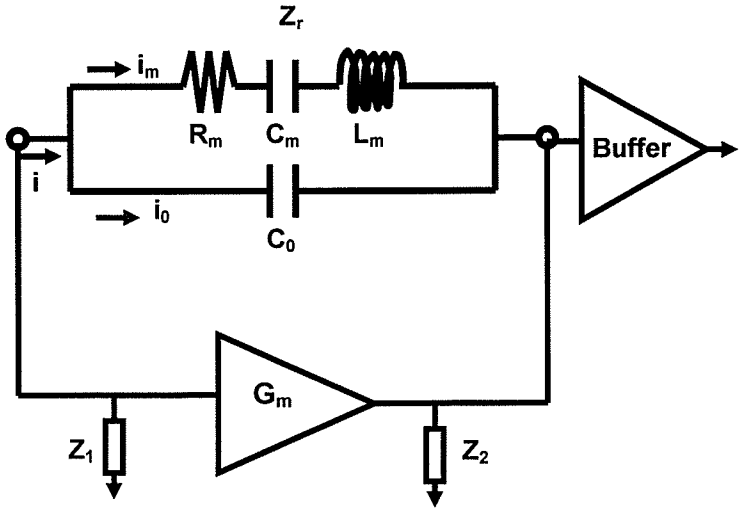

Figure 6.1 Schematic diagram of the microresonator oscillator

As shown in figure 6.1, G_m is the gain of an amplifier, Z_r represents impedance of the resonator, Z_1 and Z_2 are the impedance of capacitive or resistive elements. The sustaining circuit using capacitive Z_1 and Z_2 is defined as the pierce oscillator and for resistive Z_1 and Z_2 the transresistance amplifier oscillator is named. The oscillator outputs its periodical signal through a buffer amplifier which does not affect the performance of positive feed back loop circuit.

Based on above oscillator schemes, an oscillator was constructed and tested using the measured 11 MHz resonator. Its success still remains to be explored.

References

[1] G. T. A. Kovacs, "Micromachined Transducers Sourcebook", Boston: McGraw Hill, 1998.

[2] Jack, W. Judy, "Micromechanical Systems", Smart Mater. Struct. 10 (2001) 1115-1134.

[3] Ashwin A. Seshia, Trey A. Roessig, Roger T. Howe, et al., "A Vacuum Packaged Surface Micromachined Accelerometer", Journal of Microelectromechanical Systems, Vol. 11, No. 6, December 2002.

[4] M. Aikele, et al., "Resonant accelerometer with self-test", Sensors and Actuators A 92 (2001) 161-167.

[5] N. Yazdi, F. Ayazi and K. Najafi, "Micromachined Inertial Sensors," Proceedings of the IEEE, Aug., pp. 1640-1659, 1998.

[6] Victor M. Lubecke and Jung-Chih Chiao, "MEMS Technologies for Enabling High Frequency Communications Circuits", The IEEE 4th International Conference on Telecommunications in Modern Satallite, Cable and Brodcasting Services, Nis. Yugoslavia, Oct. 13, 1999.

[7] Clark t.-C.Nguyen, "Micromechanical Circuits for Wireless Communications". Proceedings, 2000 European Solid-State Device Research Conference, Cork, Ireland, Septmber 11-13, 2000, pp. 2-12.

[8] Frank D. Bannon, John R. Clark and Clark T.-C. Nguyen, "High-Q HF Microelectromechanical Filters", IEEE Journal of Solid-State Circuits, Vol. 35, No. 4, April 200.

[9] Liwei Lin, Roger T. Howe and Albert P. Pisano, 'Microelectromechanical Filters for Signal Process", Journal of Microelectromechanical Systems, Vol. 7, No. 3, Sept. 1998.

[10] Ark-Chew Wong and Clark T,-C. Nguen, "Micromechanical Mixer-Filters ("Mixlers")", Journal of Microelectromechanical Systems, Vol. 13, No. 1, Feb. 2002.

[11] Reza Navid, John R. Clark, Mustafa Demirci and Clark T.-C Nguyen, "Third-order Intermodulation Distortion in Capacitively-Driven CC-Beam Micromechanical Resonators", Technical Digest Int. IEEE Conf. Micromechanical Syatem Conference intertaken, Switzerland, PP. 228-231, 2001.

[12] T. Albrecht, P. Grutter, D. Horne and D. Rugar, "Frequency modulation detection using high-Q cantilevers for enhanced force microscope sensitivity," Journal of Applied Physics, vol. 69, no. 2, pp. 668-673, 1991.

[13] M. Esashi, "Resonant Sensors by Silicon Micromachining," in Proc. IEEE International Frequency Control Symposium, 1996, pp. 609-614.

[14] T. Boltshauser, M. Schonholzer, O. Brand and H. Baltes, "Resonant humidity sensors using industrial CMOS-technology combined with postprocessing," Journal of Micromechanics and Microengineering, vol.2, no.3, Sept., pp. 205-207, 1992.

[15] P. Enoksson, G. Stemme and E. Stemme, "A silicon resonant sensor structure for Coriolis mass-flow measurements," IEEE/ASME Journal of Microelectromechanical Systems, vol.6, no.2, pp. 119-125, 1997.

[16] C. Hagleitner, D. Lange, N. Kerness, A. Hierlemann, O. Brand, and H. Baltes, "A gas detection system on a single CMOS chip comprising capacitive, calorimetric, and mass-sensitive microsensors," in Technical Digest IEEE International Solid-State Circuits Conference, San Francisco, CA, USA, Feb. 2002, pp. 430-431.

[17] E. -L. Florin, M. Reif, H. Lehmann, M. Ludwig, C. Dornmair, V. T.Moy, H. E. Gaub, "Sensing specific molecular interactions with the atomic force microscope," Biosensors & Bioelectronics, vol. 10, no. 9-10, Dec., pp. 895-901, 1994.

[18] B. Ilic, D. Czaplewski, M. Zalalutdinov, H. Craighead, H. Neuzil, C. Campagnolo, C. Batt, "Single cell detection with micromechanical oscillators," Journal of Vacuum Science & Technology B (Microelectronics and Nanometer Structures), vol.19, no. 6, Nov. pp. 2825-2828, 2001.

[19] Z. Kadar, A. Bossche, J. R. Mollinger and P. M. Sarro, "Magnetic-field measurements using an integrated resonant magnetic-field sensor," Sensors and Actuators A (Physical), vol. A70, no. 3, Oct., pp.225-32, 1998.

[20] Alain Bosseboeuf and Sylvain Petitgrand. "Characterization of the static and dynamic bahaviour of M(O)EMS by optical techniques: status and trends." J. Micromech. Microeng. 13 (2003) S23-S33,

[21] Christian Rembe, et al. "Optical measurement method to study dynamic behavior in MEMS", from web site, http://www-basc.eecs.berkeley.edu.

[22] Samara L. Firebaugh, et al. "Optical Deflection Measurement for Characterization of Microelectriomechanicl Systems (MEMS)" IEEE Transactions on Instrumentation and Measurement, Vol. 53, No. 4. August, 2004.

[23] S. Timoshenko, "Vibration problems in engineering". John Wiley & Sons, 1974.

[24] Harrie A C Tilmans, "Equivalent circuit representation of electromechanical transducers, II: distributed-parameter systems", J. Micromech. Microeng. **7** (1997) 285 309;

[25] Tilmans H A C, "Equivalent circuit representation of electromechanical transducers, I: lumped-parameter systems". J. Micromech. Microeng. **6** (1996) 157–76.

[26] Lecture notes by Olav Solgaard. http://www.stanford.edu/group/SML/ee321.

[27] Sayanu Pamidighantam, et al., "Pull-in voltage analysis of electrostatically actuated beam structures with fixed–fixed and fixed–free end conditions", J. Micromech. Microeng. **12** (2002) 458–464.

[28] Yongchul Ahn, et al., "Capacitive microbeam resonator design", J. Micromech. Microeng. **11** (2001) 70-80.

[29] A. A. Seshia, PHD Theses, University of California at Berkeley, 2002.

[30] Ikeda, K., Kuwayama, H., Kobayashi, T., Watanabe, T., Nishikawa, T., Yoshida, T., Harada, K., 1990, 'Silicon pressure sensor integrates resonant strain gauge on diaphragm', Sensors and Actuators A: Physical **21–23**: 146–150.

[31] Constant A.J. Putman, et al. "A detailed analysis of the optical beam deflection technique for use in atomic force microscopy." J. Appl. Phys. 72 (1) 1, 1992, pp 6.

[32] Richard Xuesong Qi. Master Thesis, University of Manitoba, 2003.

[33] Doug. Thomson, lecture notes. University of Manitoba.

[34] Franz Larmer, et al.,"Experimental characterization of dynamic micromechanical transducers", J micromech. Microeng. 6 (1996) 177-186.

[35] P. J. Mulhern, et al., "A scanning force microscopy with a fiber optic interferometer displacement sensor', Rev. Sci. Instrum. 62 (5), May 1991, pp 1280.

[36] D. Ruger, et al. "Improved fiber–optical interferometer for atomic force microscopy." Appl. Phys. Lett. 55 (25)1989, pp 2588.

[37] D. Rugar, et al. "Force microscope using a fiber-optic displacement sensor." Rev. Sci. Instrum. 59 (11), 1988, pp 2337.

[38] S. Breen, et al. "Fiber optic displacement sensor with sub-angstrom resolution", Applied optics Vol. 29, No. 1 1990, pp. 16.

[39] C. W. Lee1, X. M. Zhang1, S. C. Tjin1 and A. Q. Liu, "Nano-scale Displacement Measurement of MEMS Devices using Fiber Optic Interferometry", Journal of The Institution of Engineers, Singapore Vol. 44, Issue 5 2004.

[40] Madou M. Fundamentals of Microfabrication (Boca Raton, FL: Chemical Rubber Company) 1997.

[41] Cronos Multi-User MEMS Process (MUMPS) webpage, www. memsrus. Com/ cronos / svcsmumps.html.

[42] J.R. Clark, W.-T. Hsu and C. T.-C. Nguyen, "Measurement Techniques for Capacively Transduced VHF-to-UHF Micromechanical Resonator". Digest of Technical Papers, the 11th International conference on Solid-State Sensors ad Actuators, Munich, Germany, June 10-14, 2001, pp. 1118-1121.

[43] Moses Teong Sen TAN, Master thesis, University of Manitoba.

[44] Ayela, F. and Fournier, T., 'An experimental study of anharmonic micromachined silicon resonators', Measurement, Science and Technology **9**, 1998, 1821–1830.

[45] Gui, C., Legtenberg, R., Tilmans, H. A., Fluitman, J. H., and Elwenspoek, M., "Nonlinearity and hysteresis of resonant strain gauges", Journal of Microelectromechanical Systems **7**, 1998, 122–127.

[46] Tilmans, H. A. and Legtenberg, R., 'Electrostatically driven vacuum-encapsulated polysilicon resonators. Part II. Theory and performance', Sensors and Actuators A45, 1994, 67–84.

[47] Turner, G. C. and Andrews, M. K., 'Frequency stabilization of electrostatic oscillators', in Digest of the 8th International Conference on Solid-State Sensors and

Actuators, Vol. 2, Stockholm, Sweden, S. Middelhoek and K. Cammann (eds.), Elsevier, Amsterdam, 1995, Vol. 2, pp. 624–626.

[48] Zook, J. D., Burns, D. W., Guckel, H., Sniegowski, J. J., Engelstad, R. L., and Feng, Z., 'Characteristics of polysilicon resonant microbeams', Sensors and Actuators **A35**, 1992, 290–294.

[49] Veijola, T., Mattila, T., Jaakkola, O., Kiihamäki, J., Lamminmäki, T., Oja, A., Ruokonen, K., Sepä, H., Seppälä, P., and Tittonen, I., 'Large-displacement modeling and simulation of micromechanical electrostatically driven resonators using the harmonic balance method', in the IEEE MTT-S International Microwave Symposium Digest, Boston, MA, T. Perkins (ed.), IEEE, New York, 2000, Vol. 1, pp. 99–102.

[50] J. Cao and C. T.-C. Nguyen, "Drive Amplitude Dependence of Micromechanical Resonator Series Motional Resistance". Digest of Technical Papers, 10th International conference on Solid-State Sensors ad Actuators, Sendai, Japan, June 7-10, 1999, pp. 1826-1829.

[51] Clark T.-C. Nguyen and Roger T. Howe. "CMOS Micromechanical Resonator Oscillator". Technical Digest, IEEE International Electron Devices Meeting. Washington, D. C., December 5-8, 1993, pp. 199-202.

[52] Dustin W. Carr, et al., "Measurement of mechanical resonance and loss in nanometer scale silicon wires", Appl. Phys. Lett. Vol 75, No 7, 16 August 1999.

[53] M. I. Younis and A. H. Nayfeh Nonlinear Dynamics 31: 91–117, 2003.

[54] Valerio Annovazzi-Lodi, et al., "Comparison of capacitive and feedback interferometric measurements on MEMS", Journal of microelectromechanical systems, Vol. 10, No. 3, September 2001.

[55] Randall W. Rhea, oscillator Design and Computer Simulation, McGraw-Hill, 1997

[56] C. T-C. Nguyen and R. T. Howe, "An integrated CMOS micromechanical resonator high-Q oscillator," IEEE Journal of Solid-State Circuits, vol.34, no.4, Apr., pp. 440-55, 1999.

[57] T. A. Roessig, R. T. Howe, A. P. Pisano and J. H. Smith, "Surface-Micromachined 1MHz Oscillator With Low-Noise Pierce Configuration," in Technical Digest Solid State Sensors and Actuators Workshop, Hilton Head 1998, pp. 328-332.

[58] S. Lee, M. U. Demirci and C. T-C. Nguyen, "A 10-MHz Micromechanical Resonator Pierce Reference Oscillator for Communications," in Proc. Eleventh International Conference in Solid State Sensors and Actuators, 2001, pp. 1094-1097.

[59] T. Mattila, O. Jaakkola, J. Kiihamaki, J. Karttunen, T. Lamminmaki, P. Rantakari, A. Oja, H. Seppa, H. Kattelus and I. Tittonen, "14 MHz micromechanical oscillator," in Proc. 11th International Conference on Solid-State Sensors and Actuators, Transducers '01, Berlin, Germany, 2001, pp. 1102-1105.

[60] A. A. Seshia, W. Low, S. A. Bhave, R. T. Howe and S. Montague, "Micromechanical Pierce Oscillator for Resonant Sensing Applications," in Proc. Fifth International Conference on Modeling and Simulation of Microsystems, San Juan, Puerto Rico, 2002, pp. 162-165.